Numerical studies of electron transfer in systems with dissipation

von der Fakultät für Naturwissenschaften
der Technischen Universität Chemnitz
genehmigte Dissertation zur Erlangung des akademischen Grades
doctor rerum naturalium
(Dr. rer. nat.)

vorgelegt von Dipl.-Chem. Ivan Stelyianov Kondov

geboren am 18. März 1973 in Dobrich (Bulgarien)

eingereicht am 17. Oktober 2002

Gutachter: Prof. Dr. M. Schreiber, IU Bremen
Prof. Dr. K. H. Hoffmann, TU Chemnitz
Dr. habil. V. May, Humboldt Universität zu Berlin

Tag der Verteidigung: 31. Januar 2003

http://archiv.tu-chemnitz.de/pub/2003

Bibliographische Beschreibung

Kondov, Ivan Stelyianov
Numerical studies of electron transfer in systems with dissipation
Dissertation (in englischer Sprache), Technische Universität Chemnitz,
Fakultät für Naturwissenschaften, Chemnitz, 2002
105 Seiten, 31 Abbildungen, 5 Tabellen

Referat

Diese Dissertation befasst sich mit Modellrechnungen zur Dynamik vom photoinduzierten Elektrontransfer und Exzitontransfer in Systemen mit vielen Freiheitsgraden. Außerdem trägt diese Arbeit zu einigen theoretischen und numerischen Aspekten der Redfield-Theorie bei. Betrachtet werden der ultraschnelle Elektrontransfer im Farbstoff Betain-30, die Elektroninjektion von einem Chromophormolekül Perylen ins Leitungsband vom Halbleiter TiO_2, sowie die Exziton-Ausbreitung in einem modellhaften ringförmigen System mit 18 Lokalisierungszentren.

Zuerst wurde der Einfluss der elektronischen Kopplung auf die Dissipationsterme der Redfield-Gleichung untersucht. Es wurde gezeigt, dass bei bestimmten Potenzialkonfigurationen die Vernachlässigung der elektronischen Kopplung (die s.g. *diabatic damping approximation*, DDA) dazu führt, dass das System nicht in das thermische Gleichgewicht mit dem Wärmebad relaxiert. Jedoch verliert die DDA ihre Gültigkeit nicht für kleine elektronische Kopplung in einer ganzen Reihe von Fällen, z.B. in der *Marcus inverted region*. Die Transfermechanismen, welche jenseits dieser Näherung auftreten, werden mit Hilfe der Störungstheorie erster Ordnung in der elektronischen Kopplung detailliert untersucht. Solche Betrachtung in diabatischer Darstellung beseitigt viele der Nachteile sowohl der DDA als auch der exakten Formulierung in adiabatischer Darstellung. Weiterhin wurden direkte Verfahren zur genauen numerischen Lösung zeitlokaler Mastergleichungen (bzw. der Redfield-Gleichung) implementiert und getestet. Die Effizienz dieser Methoden wurde am Beispiel von einem eindimensionalen Elektrontransfer-Modell bestimmt. Desweiteren wurde noch ein neues stochastisches Verfahren zur Propagation von Dichtematrizen entwickelt und in den Simulationen verwendet.

Der ultraschnelle photoinduzierte Elektrontransfer in Betain-30 wurde sowohl mit einer einzelnen Reaktionsmode als auch mit zwei Reaktionsmoden modelliert. Anhand der reduzierten Dichtematrix ließ sich die Gesamtpolarisation berechnen und somit war es möglich, ein Pump-Probe-Experiment zu simulieren. Die Rechenergebnisse wurden dann mit experimentellen Daten verglichen.

Die Anpassungsfähigkeit der Dichtematrix-Theorie an physikalisch sehr unterschiedliche Modelle hat auch ermöglicht, Exzitontransfer in biologischen Systemen und Elektrontransfer an Oberflächen zu untersuchen. Das Studium des letztgenannten Systems stellt eine neue Anwendung der Dichtematrix-Methode dar.

Schlagwörter

Elektrontransfer, Exzitontransfer, dissipative Quantendynamik, reduzierte Dichtematrix, Redfield-Theorie, stochastische Wellenfunktion, Dissipation, Pump-Probe-Spektroskopie, Betain-30

Contents

List of abbreviations **7**

1 Preamble **9**

2 Redfield theory and models for electron transfer **12**

2.1 Introduction 12
2.2 Reduced density matrix formalism 13
2.3 Electron transfer in a two-center system 17
2.4 Electron transfer model with multiple reaction coordinates 20
2.5 Perturbation expansion of the relaxation operator 21
2.6 Population dynamics in a two-center system 23
2.7 Transfer mechanisms within the first-order expansion of the relaxation operator 28
 2.7.1 Configurations with barrier in the normal region 29
 2.7.2 Barrierless configurations and configurations in the inverted region . 31
2.8 Summary 31

3 Numerical methods **33**

3.1 Introduction 33
3.2 Scaling properties of the Redfield quantum master equation 34
3.3 Direct reduced-density-matrix propagators 35
 3.3.1 Runge-Kutta method 36
 3.3.2 Short iterative Arnoldi propagator 36
 3.3.3 Symplectic integrator 37
 3.3.4 Newton polynomial scheme 37
 3.3.5 Chebyshev polynomial scheme 38
3.4 Performance of the direct propagators 39
3.5 Stochastic wave function methods 43
 3.5.1 Unraveling of Lindblad quantum master equations 44
 3.5.2 A new unraveling scheme for generalized quantum master equations 45
3.6 Summary 51

4 Intramolecular electron transfer in betaine-30 **54**

4.1 Experimental and theoretical background 54

4.2 Population dynamics and electron transfer rates 56
4.3 Pump-probe spectroscopy 59
4.3.1 Description of the method 60
4.3.2 Results 61
4.4 Summary 65

5 Photoinduced electron injection 67
5.1 Introduction 67
5.2 Model 68
5.3 Results 69

6 Exciton transfer in biological systems 72
6.1 Introduction 72
6.2 Model 73
6.3 Results 78

7 Conclusion 79

A Calculation of Λ_{nm} 82

B Stochastic wave function algorithm 84
B.1 The standard quantum jump method 84
B.2 The new quantum jump method 85

Bibliography 87

Erklärung gemäß Promotionsordnung §6 (2) 4, 5 97

Thesen zur Dissertation 98

Lebenslauf 101

Veröffentlichungen und Vorträge 103

Danksagung 105

List of abbreviations

CP	Chebyshev polynomial scheme
D^+A^-	charge-transfer donor-acceptor state
DA	neutral donor-acceptor state
DDA	diabatic damping approximation
DR0	zeroth-order perturbation expansion in v
DR1	first-order perturbation expansion in v
DR	diabatic representation
ER	eigenstate representation
ET	electron transfer
NP	Newtonian polynomial scheme
PES	potential energy surface
QME	quantum master equation
RDM	reduced density matrix
RK	Runge-Kutta propagation method
RK-NAG	Runge-Kutta from the *Numerical Algorithms Group*
RK-NR	Runge-Kutta from the *Numerical Recipes*
RWA	rotating wave approximation
SA	secular approximation
SIA	short iterative Arnoldi propagation method
SI	symplectic integrator
SSE	stochastic Schrödinger equation

Chapter 1

Preamble

Quantum dynamics of complex molecules or molecules in a dissipative environment has attracted a lot of attention during the last years. In particular, the effort of numerous scientists in the last two decades has been focused on the theoretical description of electron transfer (ET) which has been regarded as a key process in many chemical reactions in gaseous and condensed phase. ET can be generally defined as a transition between two microscopic states whereby an electron changes its spatial location moving from a donor site to an acceptor site. Since the middle of the twentieth century the theoretical research on ET has greatly advanced as the first quantitative description for ET, the theory of Marcus, appeared [72]. Based on the classical transition state theory the electron was considered as a classical particle moving in an effective potential along the reaction coordinate and possibly passing over a barrier. The main result of this classical approach is the rate law with maximum at the configuration where the reorganization energy equals the change of the free energy of the reaction. A second issue concerns the so called *inverted region* whose existence was experimentally confirmed for intramolecular ET in organic radical anions [17] and in betaine dyes [51]. The predicted rate dependence was in excellent agreement with the experimentally determined rates of many systems [17] except for some systems in the inverted region like the betaine dyes [51, 117] for which the rates are strongly underestimated by Marcus theory. As the electronic coupling between the donor and the acceptor groups in the betaine dyes is very strong the quantum effects like tunneling and resonances predominate in the overall mechanism and hence increase the measured rates. On the other hand the dynamic solvent effects were not taken into account in Marcus theory. The solvent can change not only the energy of the electronic states but also, playing the role of a dissipative environment, can take part in the reaction dynamics. Further attempts to account for the quantum effects as well as for the dynamic solvent effects resulted in other rate theories [113, 48]. Recently, path integral methods [119, 70], semi-classical approaches [36] and semi-group methods [20, 59, 54] were applied to ET problems. Nearly all quantum approaches use the reduced density matrix (RDM) formalism in order to proceed with only those degrees of freedom of the total system which are relevant for the ET dynamics. In contrast to the rate theories the RDM approach allows for a physically correct formulation of the quantum dynamics on very short time scales. Several RDM studies based on or derived from the Redfield theory succeeded to treat ET in the normal [76,47,25,23] and in the inverted region [122,27,103,23]. The Redfield theory was originally established in the research area of nuclear magnetic resonance [98]. Compared to path integral methods the Redfield theory is advantageous to approach systems with ever increasing complexity. The path integral methods are still limited for simple and sometimes trivial systems since they, implemented numerically, are computationally very demanding. Progress in this respect was done by Makri *et al.* [71] who applied their numerical path integral technique to ET in bacterial photosynthesis using a simple three-state model. More recently a very promising quantum-classical iterative hybrid method was developed [109, 118] which allows for a numerically accurate treatment of highly complex systems (e.g. polyatomic molecules in solution) at reasonable computational costs. The iterative hybrid method was successfully tested on the spin-boson model for ET [116]. The remarkably rapid progress of ET theories was, among others, reviewed by Barbara *et al.* [5] and more recently by Bixon and Jortner [8].

This thesis presents novel numerical simulations of carrier transfer in three different systems with use of Redfield theory as well as certain advance in some purely theoretical and numerical aspects of the Redfield approach.

Chapter 2 gives a brief introduction to the RDM theory. A microscopic model for ET shall be introduced and the limits of several approximations for the Redfield master equation for this ET model shall be examined. It will be shown that for certain potential configurations and electronic coupling strengths the Redfield theory must be applied in a strict way without further approximations. In the next Chapter 3 a large selection of established methods for the numerical solution of QME is tested and their numerical efficiency is verified on the example of the ET model with one reaction coordinate. A new stochastic wave function method is proposed and its applicability for solving the Redfield QME is proven.

The next three chapters include applications of the introduced theory, models and numerical methods to experimentally relevant systems. Chapter 4 reports on photoinduced ET in betaine-30 in solution. The classical Marcus theory and the quantum mechanical golden rule fail to predict the rate because of the large value of the donor-acceptor electronic coupling. In order to be successful one has to elaborate the model so that dynamic solvent effects as well as multi-mode internal vibrational energy redistribution during the ET transition with the participation of a low-frequency mode can be considered. All these peculiarities of betaine dyes make their quantum dynamical treatment a very demanding task. In the introduction of Chapter 4 the state of the art in this research area will be overviewed. Then a donor-acceptor model comprising two reaction modes will be constructed. First, the ET rates are computed and compared with the rates calculated with the single-reaction-mode model as well as with the rates predicted by other theories and measured in experiment. Next, using again the RDM approach in the framework of Redfield theory and a two-mode model for ET, transient emission-absorption spectra with high frequency and time resolution are simulated. The simulated spectra are compared with recent experimental data, discussed and conclusions about the ET mechanism are done.

The treatment of photoinduced ET from a chromophore molecule attached to the surface of a semiconductor represents an additional challenge for the theory as the conduction band of the semiconductor has to play the role of an acceptor. Such an acceptor can be modeled with a quasi-continuum of diabatic states. The system of choice, a covalently attached perylene chromophore to the surface of porous TiO_2, was recently studied in pump-probe experiments [13]. Chapter 5 gives an extension to the existing theory [95] and numerical simulations [96] by taking the vibrational dissipation into account.

In addition to open spin systems and ET systems Redfield theory allows for treatment of other physically different problems such as exciton transfer. Chapter 6 deals with exciton dynamics in biological chlorophyll aggregates. The system Hamiltonian describes a single exciton propagating in a model ring structure. The simulation takes into account static disorder in the local energies of the ring sites as well as the dynamic disorder induced by the thermal bath. The experimentally measured quantity is here the anisotropy of fluorescence which is numerically simulated. Furthermore, non-Markovian effects in the short-time exciton transfer dynamics are considered. The influence of non-Markovian effects is estimated by comparing with the results obtained by Redfield theory. Finally, all results from the whole work are summarized and conclusions are given in Chapter 7.

Chapter 2

Redfield theory and models for electron transfer

2.1 Introduction

Besides classical and semi-classical descriptions of dissipative molecular systems several quantum theories exist which fully account for the quantum effects in dissipative dynamics. Among the latter are the reduced density matrix (RDM) formalism [9, 74, 20, 59, 54] and the path integral methods [119, 70]. The basic concept in all these theories is the separation of the total system into relevant system and thermal reservoir (bath) as sketched in Fig. 2.1. All considerations and calculations in this thesis shall be done in the framework of Redfield theory [98], in which one has to solve a quantum master equation (QME) for the RDM. It is obtained from the Liouville-von Neumann equation[1]

$$\frac{\partial \sigma}{\partial t} = -i\,[H, \sigma] \tag{2.1}$$

which describes the time evolution of the density matrix σ of the total system by performing a second-order perturbation treatment in the system-bath coupling as well as restricting the calculation to the Markovian limit. In this approach the quantum dynamics of an "open" system, e.g. the irreversible loss of coherence with time and the exchange of energy with the thermal bath, can be described. The unidirectional energy flow into the environment (the bath) is called dissipation. Within this theory it is possible e.g. to simulate the dissipative short-time population dynamics usually detected by modern ultrafast spectroscopy experiments.

To be rigorous in applying Redfield theory, the operators describing the time evolution have to be expressed in eigenstate representation (ER) of the relevant system as has been done in the original paper [98]. For electron transfer this was performed in part of the literature (see for example [25, 90, 45, 46]), while in another part [77, 75, 62, 27, 121, 122] diabatic (local) representations (DRs) have been used.

While in ER the dissipative term is evaluated exactly, in DR the influence of the coupling between the local subsystems on dissipation is neglected. As a consequence

---

[1] Atomic units will be used for the equations, i.e. $\hbar = 1$.

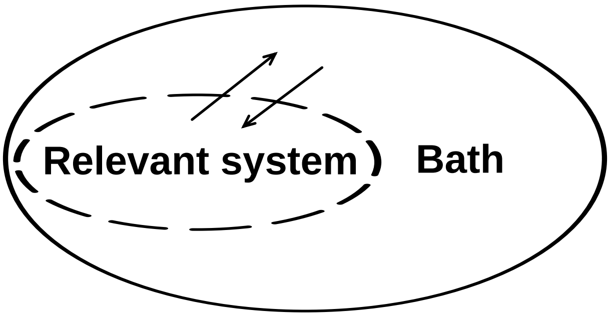

Figure 2.1: System-bath separation.

the relaxation terms do not lead to the proper thermal equilibrium of the coupled system [20,105]. Only the thermal equilibrium of each separate subsystem is reached which can be quite different from the thermal equilibrium of the coupled system. In the following it will be shown that even for a very small intercenter coupling a completely wrong asymptotic value can be obtained.

Although possibly leading to the wrong thermal equilibrium the local DR has advantages. For large problems it may be difficult to calculate the eigenstates of the system. These are not necessary in the DR. There one only needs the eigenstates of the subsystems. The quantum master equation can be implemented more efficiently in DR in many cases [77, 123, 104, 55]. Moreover, almost all physical and chemical properties of transfer systems are expressed in the DR. For example, to determine the transfer rate one often calculates the population of the diabatic states and obtains the rate from their time evolution.

Using the semi-group methodology and a simple model of two fermion sites, DR and ER have been compared already [20]. The curve-crossing model, used in the present work, requires a more complicated treatment. Here DR and ER will not only be compared but it will be shown how the relaxation term can be written more precisely in DR for small intercenter coupling.

2.2 Reduced density matrix formalism

The total system under consideration is divided into a relevant system (S) and a heat bath (B) (Fig. 2.1). Therefore the total Hamiltonian consists of three terms – the relevant system part H_S, the bath part H_B, and the system-bath interaction H_SB:

$$H = H_\mathrm{S} + H_\mathrm{B} + H_\mathrm{SB}. \tag{2.2}$$

As already introduced, the full description of the whole system can be reduced using a RDM (in the following ρ) which depends only on the degrees of freedom of the relevant system. In the trivial case of vanishing H_SB such a reduction is straightforward because the total density matrix simply factorizes. The treatment of cases with finite values of H_SB requires more special formal approaches, such as the path integral method or perturbation theory in H_{SB}. The former method provides an exact description for arbitrary values of H_{SB}. In contrast, perturbation theory makes sense only for sufficiently small H_{SB}. Moreover, it is not easy to answer *a priori* the question of how small H_{SB} has to be. This can be answered only when one has derived closed equations of motion for the RDM. The first-order expansion in H_{SB} of the Liouville-von Neumann equation for the full system (2.1) leads to the so called mean field correction to the system dynamics [74]. The only physical meaning of this correction is a shift of the energy scale of H_{S} which gives no relaxation behavior of the dynamics. Therefore one has to expand Eq. (2.1) to second order in H_{SB} making use of a special projector formalism (Nakajima-Zwanzig formalism) which i) allows for factorization of the total density matrix and ii) ensures exact summation of the perturbation series to arbitrary order. This formalism is performed in the interaction picture and its application to derive a closed QME for the RDM is thoroughly described in Ref. [74]. On the way of derivation the following additional assumptions are made.

1. The bath stays in thermal equilibrium for any time scale of the dynamics of the relevant system and its macroscopic state is given by a canonical distribution

   $$\rho_{\mathrm{B}} \approx \frac{e^{-\beta H_{\mathrm{B}}}}{\mathrm{tr} e^{-\beta H_{\mathrm{B}}}} \tag{2.3}$$

   where $\beta = 1/(k_{\mathrm{B}}T)$ is the inverse temperature.

2. The initial full density matrix factorizes as $\sigma(t_0) \approx \rho(t_0)\rho_{\mathrm{B}}$. According to Eq. (2.3) the density matrix of the bath ρ_{B} does not depend on the RDM $\rho(t_0)$. Thus, the factorization of $\sigma(t_0)$ means that initial correlations between the relevant system and the bath are not taken into account.

3. The system-bath interaction is modeled by bilinear terms containing relevant system operators K_m acting only in the state space of the relevant system and bath operators Φ_m acting in the state space of the bath

   $$H_{\mathrm{SB}} = \sum_m K_m \Phi_m . \tag{2.4}$$

   In contrast to the first two items, this assumption does not present a restriction of the second-order perturbation theory. It is sufficiently general and is done for convenience. Redfield theory was originally derived without this assumption. It has also to be noted that in some cases the index m in Eq. (2.4) counts up to 1 (only one term is considered), in other cases to more than 1, depending on the microscopic model.

The resulting time-nonlocal QME with omitted first-order mean-field term reads [74]

$$\begin{aligned}\frac{\partial \rho}{\partial t} = -i\left[H_{\mathrm{S}}, \rho\right] - \sum_{m,n} \int\limits_0^{t-t_0} d\tau \Big\{ & C_{mn}(\tau)\left[K_m, e^{-iH_{\mathrm{S}}\tau} K_n \rho(t-\tau) e^{iH_{\mathrm{S}}\tau}\right] \\ & - C^*_{mn}(\tau)\left[K_m, e^{-iH_{\mathrm{S}}\tau} \rho(t-\tau) K_n e^{iH_{\mathrm{S}}\tau}\right]\Big\} .\end{aligned} \tag{2.5}$$

The first term on the right-hand side of this integro-differential equation describes the coherent dynamics of the relevant system. The other nonlocal terms give rise to dissipation. Characteristic for Eq. (2.5) is that the RDM at time t depends explicitly on its own history $\rho(t-\tau)$. This memory introduces a strong nonlinearity into the QME and makes the direct integration of Eq. (2.5) infeasible. The quantity $C_{mn}(\tau)$ is the bath correlation function which establishes a connection between the fluctuations of the operators Φ_m and Φ_n around their equilibrium values $\langle\Phi_m\rangle$, respectively $\langle\Phi_n\rangle$, at different times

$$C_{mn}(\tau) = \langle\Phi_m(t)\Phi_n(0)\rangle - \langle\Phi_m\rangle\langle\Phi_n\rangle. \tag{2.6}$$

The bath correlation function is characterized by a correlation time τ_c, giving the time scale on which $C_{mn}(\tau)$ decays to zero. If τ_c is short compared to any other characteristic time scale of the system then $C_{mn}(\tau)$ can be approximated by $c_{mn}\delta(\tau)$. Using such an assumption Eq. (2.5) is reduced to its Markovian limit. Since the operators Φ_m and K_m can be chosen to be Hermitian [33,32] the matrix c_{mn} can then be diagonalized by means of a unitary transformation $c = U^\dagger\kappa U$ and Eq. (2.5) can be cast into a special symmetric form, which is called Lindblad form

$$\frac{\partial\rho(t)}{\partial t} = -i\left[H_\mathrm{S},\rho(t)\right] + \sum_n\left[L_n\rho(t)L_n^\dagger - \frac{1}{2}\rho(t)L_n^\dagger L_n - \frac{1}{2}L_n^\dagger L_n\rho(t)\right], \tag{2.7}$$

where $L_n = \sqrt{\kappa_n}\sum_m U_{nm}K_m$. The Lindblad QME (2.7) has been extensively used in the quantum optics community (see e.g. [19,29,35,30,89]) because by construction/generation it keeps the RDM Hermitian, normalized, and positive semidefinite. The last property ensures that all eigenvalues of the RDM (the populations) stay non-negative which is important for the physical interpretation of the populations as probabilities. As it will be shown later the Lindblad form of QME is obtainable on other levels of approximation as well. This means that κ_n, which can be viewed as generalized diffusion coefficients (or rates), may hold quite different physical information depending on how Eq. (2.7) is obtained.

It is very difficult, and sometimes even impossible, to model a real system with a δ-correlated bath. Thus, one is naturally motivated to search for another approach to bring the memory kernel in Eq. (2.5) into a time-local form, i.e. to ignore the memory effects. Let us suppose that the integrand in Eq. (2.5) does not change significantly within the time interval $[0;\tau_m]$, whereby the memory time τ_m is related but not necessarily identical to the bath correlation time τ_c. Under this assumption one can invoke the *Markov approximation* by substituting $\rho(t-\tau)$ with $\rho(t)$. This implies that the continuous time axis t (the axis of the solution $\rho(t)$) has a coarse mesh size $\Delta t > \tau_m$ and hence the upper integral limit can be extended to infinity. Technically the Markov approximation is applied within the interaction picture in which the fast oscillating off-diagonal elements in the RDM vanish [74]. As result, one has to plug $\rho(t-\tau) \rightarrow e^{iH_\mathrm{S}\tau}\rho(t)e^{-iH_\mathrm{S}\tau}$ into Eq. (2.5). Making use of the compact notation

$$\Lambda_m = \sum_n\int\limits_0^\infty d\tau C_{mn}(\tau)K_n^\mathrm{I}(-\tau), \tag{2.8}$$

where $K_n^{\mathrm{I}}(-\tau) = e^{-iH_{\mathrm{S}}\tau} K_n e^{iH_{\mathrm{S}}\tau}$ is the operator K_n in the interaction representation, the final form of the desired Markovian QME reads [91, 74]

$$\frac{\partial \rho}{\partial t} = -i\,[H_{\mathrm{S}}, \rho] + \sum_m \Big\{ \Big[\Lambda_m \rho, K_m\ \Big] + \Big[K_m, \rho \Lambda_m^\dagger\Big] \Big\}. \tag{2.9}$$

This is the Redfield equation expressed in terms of the operators Λ_m and K_m acting in the Hilbert space. For historical reasons one should mention that the original Redfield equation [98, 9] is written in terms of the Redfield tensor $\mathcal{R}$ instead. The latter is acting on the RDM like the Liouville superoperator $\mathcal{L}$

$$\frac{\partial \rho}{\partial t} = -i[H_{\mathrm{S}}, \rho] + \mathcal{R}\rho = \mathcal{L}\rho. \tag{2.10}$$

A unique relation between $\mathcal{R}$, K_m and Λ_m can be obtained after some algebra in arbitrary representation. The action of the Redfield tensor can be expressed in state representation as

$$\langle i|\mathcal{R}\rho|j\rangle = \sum_{k,l} R_{ij,kl}\,\rho_{kl}\ . \tag{2.11}$$

If the indices m and n are suppressed for simplicity the matrix elements of the Redfield tensor read

$$R_{ij,kl} = K_{lj}\Lambda_{ik} + \Lambda_{lj}^\dagger K_{ik} - \delta_{lj}\sum_r K_{ir}\Lambda_{rk} - \delta_{ik}\sum_r \Lambda_{lr}^\dagger K_{rj}\ . \tag{2.12}$$

In the original paper [98] it is proposed that some terms of $\mathcal{R}$ can be regarded as perturbations and can be ignored if $R_{ijkl} \ll |\omega_{ij} - \omega_{kl}|$. Here ω_{ij} are the transition energies for $|i\rangle \rightarrow |j\rangle$. All remaining terms, the so called *secular terms*, enter two decoupled equations of motion. The first one involves the off-diagonal elements of ρ (the coherences) and has an analytical solution

$$\rho_{ij}(t) = \rho_{ij}(0)e^{-i\omega_{ij}t}e^{R_{ij,ij}t}\ . \tag{2.13}$$

The second one is the Pauli master equation for the diagonal elements of ρ (the populations) [74, 23]

$$\frac{\partial \rho_{ii}}{\partial t} = \sum_{j\neq i} R_{ii,jj}\rho_{jj}(t) + R_{ii,ii}\rho_{ii}(t)\ . \tag{2.14}$$

According to Redfield [98] this approximation, known as *secular approximation* (SA) has to be applied with caution for systems with resonances and should not be applied for systems with degeneracy. A special case in which the SA is known to fail is if a strong resonant field is applied [98]. Further in Sec. 2.6 the SA will be numerically compared with other levels of approximation when applied to a simple ET model.

Summing up, let us first answer the question about the range of validity for the second-order perturbation theory (also known as *the second Born approximation*). Looking at the right-hand side of Eq. (2.5) one can extract the magnitude of the contribution of the first-order and of the second-order term, respectively $\langle H_{\mathrm{S}}\rangle$ and $\tau_m\langle H_{\mathrm{SB}}\rangle^2$ [74]. The perturbation expansion is justified only if the latter quantity is smaller that the former one.

The Markovian approach with the use of the Redfield equation succeeds especially in treating excitation/relaxation of nuclear spins in molecules in strong magnetic fields (e.g. in NMR spectroscopy) [98,9,18]. In these systems the environment has much shorter correlation times than the times for which the spin states evolve. However, there exist many physically relevant situations in which the environment correlation time is comparable or even longer that the evolution time scale of the relevant system and the Markovian description fails. In particular, for very low temperatures the bath fluctuations become relatively rare events. This leads to a very slow decay of the bath correlation function $C_{mn}(t)$ while the system relaxation has still very short characteristic times (e.g. ET between centers in frozen media). In addition to the necessary quantal description the memory effects have to be taken into account in this case.

2.3 Electron transfer in a two-center system

As far as the aim of this work is to approach systems with ET the next step has to be modeling the relevant system and the bath in an appropriate way. In most ET systems one can distinguish at least two terminal states. In the first one the particle (the electron) is localized at a center (group of atoms) which is called *donor* and the state is conventionally denoted as DA state. If the particle is localized at the center known as *acceptor* the state of the system is denoted as D^+A^- state. For all cases of intramolecular ET this basic concept seems to be sufficient. For instance, in betaine-30 the first electronically excited state S_1 can be identified as DA state and the ground state S_0 as D^+A^- state. Nevertheless, there are models for ET (applied e.g. to porphyrin-quinone complexes, DNA and other biological systems) in which the electron can occupy intermediate (bridge) centers, i.e. there exist other local states involved in the ET process. Being virtually unoccupied, such states can, however, strongly influence the dynamics of the transition from DA to D^+A^- and *vice versa*. This interesting phenomenon is known as *superexchange* which will not be investigated here. The model for the Hamiltonian of the relevant system H_S, which will be described below, has already been widely used, e.g. most recently in Refs. [77,62,25,27,47,122,23,52], and will be applied with no further modifications.

In every chemical reaction, the transitions between DA and D^+A^- cause certain reorganization of the nuclei in the molecular system along a reaction path in the potential energy surface (PES). An effective description of the reaction path can be done either by selecting representative normal vibrational modes of the molecule or by modeling the PES along a so-called effective reaction coordinate. Since for most ET reactions the modes under reorganization are diabatically coupled to the electronic states of DA and D^+A^- two crossing diabatic PESs provide a suitable representation. As first approximation the PESs can be considered harmonic as sketched in Fig. 2.2. The stable points (for harmonic PESs the minima) of the PESs correspond to the relaxed geometries of DA and of D^+A^-. In this Chapter it is not yet necessary to specify which state, DA or D^+A^-, has lower energy. All parameters that completely determine a two-center system with one reaction coordinate are the oscillator frequencies ω_1 and ω_2, the reorganization energy λ, and the change of the free energy ΔG, as depicted in Fig. 2.2. Note that in the following the

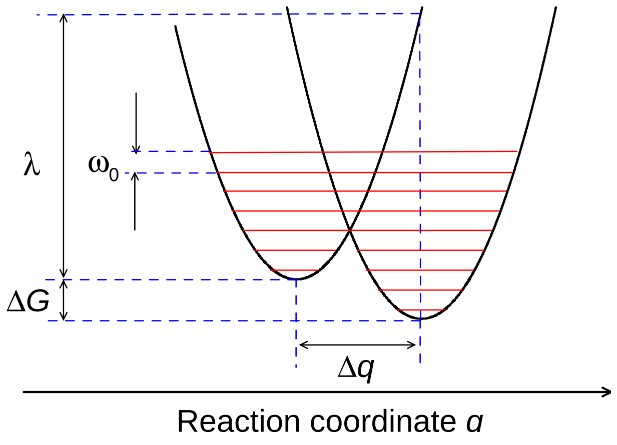

Figure 2.2: Sketch of the model with one effective mode.

frequencies for both diabatic states are assumed to be equal and designated by ω_0. The definition of the reorganization energy reads

$$\lambda = \frac{1}{2}\mathcal{M}\omega_0^2(\Delta q)^2 = \frac{1}{2}\omega_0\Delta^2 \tag{2.15}$$

where Δq is the coordinate shift and Δ the dimensionless coordinate shift of the upper state relative to the ground state and $\mathcal{M}$ is the reduced mass. Alternatively, an equivalent parameterization is done in terms of the electronic-vibrational coupling κ which is defined as the gradient of the potential of the upper state along the dimensionless coordinate at the minimum position of the ground state. Thus, it reads $\kappa = \omega_0\Delta$. Important to note is which different configurations can be considered in the framework of this model. The case $\lambda > |\Delta G|$ is called normal region in which the model particle has to overcome a (classical) barrier. This particular configuration of the model PESs is depicted in Fig 2.2. The configuration with $\lambda = |\Delta G|$, e.g. the ground-state PES intersects the upper PES at its minimum, represents the regime of maximal back-transfer rate in the classical Marcus theory [72, 73]. $\lambda < |\Delta G|$ defines the strongly exothermic *Marcus inverted region*. In this case the minimum of the upper PES is located between the crossing and the minimum of the ground-state PES with respect to the reaction coordinate. Finally, configurations with $\lambda = 0$ (no crossing of the diabatic PES) physically represent vibronically decoupled electronic states.

The harmonic potentials are coupled by an electronic coupling v_{12} assumed here to be coordinate-independent for simplicity. Thus, the Hamiltonian of the uncoupled system is then given by

$$H_0 = \sum_{i=1,2}\left[U_i + \left(a_i^\dagger a_i + \frac{1}{2}\right)\omega_i\right] \tag{2.16}$$

and the coupling by

$$V = \sum_{i,j}\sum_{M,N}(1-\delta_{ij})v_{ij}f(i,M;j,N)|iM\rangle\langle jN| \,. \tag{2.17}$$

The first index in each state vector $|iM\rangle$ denotes the diabatic PES while the second labels the vibrational level. a_i and $a_i^\dagger$ are the boson operators acting in state i, and $f(i,M;j,N)$ is the Franck-Condon factor which measures the overlap between the vibronic states $|iM\rangle$ and $|jN\rangle$. All Franck-Condon factors can be calculated with the use of the eigenfunctions $\varphi_{i,M}(q)$ of the harmonic oscillator

$$f(i,M;j,N) = \langle iM|jN\rangle = \langle iM|\Big\{\int dq|q\rangle\langle q|\Big\}|jN\rangle = \int dq\varphi_{i,M}(q)\varphi_{j,N}(q)\ . \qquad (2.18)$$

This was all necessary to model the relevant system and sufficient for the definition of H_S

$$H_\mathrm{S} = H_0 + V\ . \qquad (2.19)$$

In order to use the Redfield QME (2.9) one needs to know K and Λ. Bilinear system-bath coupling (2.4), that was already assumed, allows a variety of ways to define K_m and Φ_m. A very natural approach is expanding the PES of the total system around the global minimum into a series, restricting oneself to second order terms (all first order terms vanish automatically). Then the total PES splits into pure harmonic components which give rise to H_S described above and H_B (harmonic bath), and a presumably small coupling term proportional to $\sum_k qZ_k$ where q is the coordinate operator of the relevant system and Z_k are the bath coordinate operators. Taking only one term from Eq. (2.4) and comparing it with $\sum_\xi qZ_\xi$ one can set $K=q$ and $\Phi \propto \sum_\xi Z_\xi$. Thus, K reads

$$K = q = \sum_i \sum_{MN} (2\omega_i \mathcal{M})^{-1/2} \left(a_i^\dagger + a_i\right) |iM\rangle\langle iN| \qquad (2.20)$$

where $\mathcal{M}$ is the reduced mass of the relevant system and

$$Z_\xi = g_\xi \left(b_\xi^\dagger + b_\xi\right)\ . \qquad (2.21)$$

The rest of the total Hamiltonian is the bath of harmonic oscillators

$$H_\mathrm{B} = \sum_\xi \omega_\xi \left(b_\xi^\dagger b_\xi + 1/2\right)\ . \qquad (2.22)$$

Here one may decide to simplify the system-bath coupling model introducing the *rotating wave approximation* (RWA) [115, 119, 74]. It means that all terms in H_SB proportional to $a_i b_\xi$ and $a_i^\dagger b_\xi^\dagger$ will be neglected. They give rise to elementary transitions in which an excitation (deexcitation) occurs simultaneously both in the relevant system and in the bath. Such events are very unlikely and the RWA can be reasonably applied for weak system-bath coupling. Nonetheless, this brings no special advantages from a computational point of view except for a few special cases like the damped harmonic oscillator [53, 120] or the present ET model with additional approximations [122, 124, 23] (see Sec. 2.5). In both cases the Redfield QME (2.9) turns into a Lindblad QME (2.7).

In order to obtain relevant physical information about the ET dynamics one has to calculate the expectation values of certain observables. Most commonly used are the populations (occupation probabilities) of the diabatic states which are calculated by means of a partial trace over the vibrational levels

$$P_i = \sum_M \rho_{iMiM} . \tag{2.23}$$

For the case of propagating the RDM in the basis of diabatic states $|iM\rangle$ (i.e. in the DR) this is convenient. Using other representations one has to transform the RDM back to the DR in order to apply Eq. (2.23) which requires two matrix-matrix multiplications. In such cases it is advantageous to use the projection operator of the ith diabatic state $O_i = |i\rangle\langle i|$ instead, whose matrix is initially transformed to ER, to calculate the populations

$$P_i = \mathrm{tr}\left(\rho O_i\right) \ . \tag{2.24}$$

This is numerically less expensive because only one matrix-matrix multiplication has to be done. The populations demand little effort for calculation and provide a clear insight into the overall dynamics as well as into the mechanisms of the ET reaction. In addition, the RDM enables the simulation of experimentally detectable transient spectra, of course with more computational costs and considerable sophistication of the models. Then the relevant quantity is the total polarization that measures the response of the system to the action of external fields. The expectation value of the total polarization is necessary for these simulations and will be used in Chapter 4.

2.4 Electron transfer model with multiple reaction coordinates

As already introduced, the Redfield formalism allows arbitrary models for the relevant system. It is possible that one can subsequently take strongly coupled degrees of freedom from the bath and put them into the relevant system part. This will effectively reduce the system-bath coupling and hence make the application of the Redfield theory itself more reasonable. Multi-mode modeling of ET reactions (including systems in the inverted region) has been done in Ref. [121,122,23] with similar argumentation. On the other hand, there is experimental evidence for the participation of multiple modes in the ET transition in some systems (discussed in detail in Chapter 4). Correspondingly, the relevant part of the total ET system can be modeled with a treatably small set of R reaction coordinates $\{q_l\}$. For this purpose one may select a set of representative harmonic normal modes from the molecule and from its environment (e.g. solvent or crystal lattice). Since all normal modes are completely decoupled one can use the single-mode operators (2.16), (2.17), and (2.20) to calculate the matrix elements of the necessary operators in the full diabatic basis $|iM_1 \ldots M_R\rangle$. The matrix element of the Hamiltonian reads

$$\langle iM_1 \ldots M_R | H_\mathrm{S} | jN_1 \ldots N_R \rangle = \delta_{ij} U_i^{(0)} + \sum_{l=1}^{R} H_{iM_l,jN_l} \prod_{p \neq l} \delta_{M_p N_p} \tag{2.25}$$

where

$$H_{iM_l,jN_l} = \delta_{ij}\delta_{M_lN_l}\omega_{i,l}(M_l + \frac{1}{2}) + (1-\delta_{ij})v_{ij}f(i, M_l; j, N_l) \tag{2.26}$$

is the matrix element of the partial Hamiltonian for mode l in a single-mode basis. The $\omega_{i,l}$ denote the eigenfrequencies of the oscillators, v_{ij} the electronic coupling, and $U_i^{(0)}$ the minimum energy of the i-th diabatic state. The Franck-Condon factors $f(i, M_l; j, N_l)$ are calculated with the use of Eq. (2.18).

For R reaction coordinates the expression for H_{SB} includes R terms linear in each coordinate q_l. The matrix element of the latter reads

$$\langle iM_1 \dots M_R|q_l|jN_1 \dots N_R\rangle = \alpha_{i,l}\delta_{ij}\left(\delta_{M_l+1,N_l}\sqrt{M_l+1} + \delta_{M_l-1,N_l}\sqrt{M_l}\right)\prod_{p\neq l}\delta_{M_pN_p} \tag{2.27}$$

The prefactor $\alpha_{i,l} = \sqrt{\omega_{i,l}/2\lambda_l}\Delta q_l$ establishes the connection between $\omega_{i,l}$, the coordinate shift Δq_l and the reorganization energy λ_l.

The multi-mode model can be easily reduced to the previously defined effective single-mode model by means of an orthogonal transformation of H_{S} [87, 115]. After this procedure all R normal modes are transformed to a finite bath with $R-1$ modes bilinearly coupled to the effective mode and the coupling energy appears at the expense of the reduced reorganization energies of the modes. Thus, the reduction from a multi-mode to a single-mode model extends the bath and enlarges the system-bath coupling. The addition of modes to the relevant system can reduce the system-bath coupling and result in a larger total reorganization energy.

2.5 Perturbation expansion of the relaxation operator

Assuming a quantum bath consisting of harmonic oscillators the time correlation function of the bath operator is given as [90]

$$C(\tau) = \langle\Phi(\tau)\Phi(0)\rangle = \int_0^\infty d\omega J(\omega)n(\omega)(e^{i\omega\tau} + e^{\beta\omega}e^{-i\omega\tau}) \; . \tag{2.28}$$

Here $J(\omega)$ denotes the spectral density of the bath [90], $n(\omega) = (e^{\beta\omega} - 1)^{-1}$ the Bose-Einstein distribution, and $\beta = 1/(k_{\mathrm{B}}T)$ the inverse temperature. If Φ is Hermitian the Fourier transform $C(\omega)$ of the correlation function (2.28) has the property [90]

$$C(\omega) = e^{-\beta\omega}C(-\omega) \tag{2.29}$$

which is a necessary but not sufficient condition for the relevant system to evolve to thermodynamic equilibrium.

The Hamiltonian H_{S} of the system we are interested in can be separated according to Eq. (2.19). Two canonical bases can be constructed for such a Hamiltonian. The DR is based on the eigenfunctions of H_0. It is often called a local basis because the basis functions of the diabatic PESs are located at the specific subsystems. Latin indices such as $|m\rangle$ are used below to designate the DR basis states. The other basis diagonalizes the system Hamiltonian H_S. So it consists of eigenstates of H_S and is called adiabatic basis which has been mostly used in nuclear magnetic resonance [98, 18] as well as in ET studies [47]. These ER basis states will be denoted by Greek indices such as $|\mu\rangle$. As discussed in the introduction, Redfield theory is defined in ER but for transfer problems DRs have some conceptual and numerical advantages.

Here one first calculates the dissipation in the DR for small intercenter coupling V. In this basis the matrix elements of Λ are given by

$$\langle n|\Lambda|m\rangle = \int\limits_0^\infty d\omega J(\omega) n(\omega) \int\limits_0^\infty d\tau (e^{i\omega\tau} + e^{\beta\omega} e^{-i\omega\tau}) \langle n|K^\mathrm{I}(-\tau)|m\rangle \ . \tag{2.30}$$

To evaluate the matrix element of K we have to use perturbation theory in V because the diabatic states $|n\rangle$ are not eigenstates of H_S but of H_0. Some details of the determination of $\langle n|\Lambda|m\rangle$ are given in Appendix A. Using the real part of the Fourier transform of the correlation function (2.28)

$$C(\omega) = 2\pi[1 + n(\omega)][J(\omega) - J(-\omega)] \ , \tag{2.31}$$

and denoting the transition frequency between diabatic states $|m\rangle$ and $|n\rangle$ by ω_{mn} the final result can be written as

$$\begin{aligned} \langle n|\Lambda|m\rangle = \frac{1}{2} C(\omega_{mn}) \langle n|K|m\rangle &- \frac{1}{2} \sum_j \langle n|K|j\rangle \frac{\langle j|V|m\rangle}{\omega_{jm}} \left[C(\omega_{mn}) - C(\omega_{jn})\right] \\ &- \frac{1}{2} \sum_i \langle i|K|m\rangle \frac{\langle n|V|i\rangle}{\omega_{ni}} \left[C(\omega_{mn}) - C(\omega_{mi})\right] . \end{aligned} \tag{2.32}$$

This first-order result DR1 can be split into a zeroth-order contribution DR0 independent of V and a first-order contribution proportional to V. Taking the DR0 term

$$\langle n|\Lambda|m\rangle \ = \ \frac{1}{2} C(\omega_{mn}) \langle n|K|m\rangle \tag{2.33}$$

only is equivalent to a complete neglect of the influence of the intercenter coupling V on dissipation. This assumption has been used earlier [77, 75, 62, 27, 121, 122] and is sometimes called the *diabatic damping approximation* (DDA) [23, 52]. In this approximation only the states $|n\rangle$ and $|m\rangle$ contribute to the matrix element $\langle n|\Lambda|m\rangle$. In DR1 all states contribute to each of these matrix elements. As a consequence the spectral density of the bath is not only probed at the transitions of the uncoupled subsystems as in DR0 but at many more frequencies.

As long as the bath has constant temperature the system has to relax, after a certain time, to the thermal equilibrium with the bath. This physical requirement is fulfilled if the detailed balance condition [90] for the microscopic rates $R_{\mu\mu,\nu\nu}$ is satisfied

$$R_{\mu\mu,\nu\nu} = \exp{(-\beta\omega_{\mu\nu})} R_{\nu\nu,\mu\mu} \ . \tag{2.34}$$

This principle is valid only if $|\mu\rangle$ and $|\nu\rangle$ are eigenstates of the relevant system. If we use the diabatic states $|m\rangle$ and $|n\rangle$ instead of $|\mu\rangle$ and $|\nu\rangle$ and substitute the DR0 expression for Λ (2.33) into Eq. (2.12) and then plug the resulting rates $R_{mm,nn}$ into Eq. (2.34) we arrive exactly at Eq. (2.29) but the thermodynamic equilibrium will not always be reached as will be shown numerically in Sec. 2.6.

The ER result for the matrix elements of Λ can easily be deduced from the DR result by replacing the diabatic states by adiabatic ones and setting $V = 0$ in Eq. (2.32):

$$\langle\nu|\Lambda|\mu\rangle \quad = \quad \frac{1}{2}C(\omega_{\mu\nu})\langle\nu|K|\mu\rangle \ . \tag{2.35}$$

This result is of course correct for arbitrary intercenter coupling strength.

In the DR0 expansion (2.33) the system can emit or absorb only at transition frequencies ω_{mn}. The spectral density of the bath $J(\omega)$ is effectively reduced to discrete values $J(\omega) = \sum_\xi \gamma_\xi \delta(\omega - \omega_\xi)$. The advantage of this approach is the scaling behavior of the CPU time with the number $\mathcal{N}$ of basis functions which results from the simple structure of the Λ matrix (2.33). It scales like $\mathcal{N}^{2.3}$ as will be shown numerically in Chapter 3. This is far better than the $\mathcal{N}^3$ scaling of the DR1 approximation (2.32). In DR1 the spectral density is probed at many more frequencies. One needs the full frequency dependence of $J(\omega)$ which we take to be of Ohmic form with exponential cutoff

$$J(\omega) = \eta\Theta(\omega)\omega e^{-\omega/\omega_c}. \tag{2.36}$$

Here Θ denotes the step function and ω_c the cutoff frequency. The normalization prefactor η is determined such that the spectral densities in DR and ER coincide at ω_0. Eq. (2.36) together with Eq. (2.31) yields the full correlation function.

If the system Hamiltonian H_S is diagonalized and the resulting ER basis is used to calculate the elements of the operators in Eq. (2.9), there will be no longer any convenient structure in K or Λ, so that the full matrix-matrix multiplications are inevitable. For this reason the CPU time scales as $\mathcal{N}^3$, where $\mathcal{N}$ is the number of eigenstates of H_S. There appears to be a minimal number $\mathcal{N}_0$ below which the diagonalization of H_S fails or the completeness relation for $|\mu\rangle$ is violated. Nevertheless, the benefit of this choice is the exact treatment of the intercenter coupling. It is straightforward to obtain the matrices for ρ and K (see for example Ref. [25]).

2.6 Population dynamics in a two-center system

It is worthwhile to summarize and compare the various approximations introduced in the foregoing section. To do this, we solve Eq. (2.9) using a model with two harmonic diabatic PES with equal curvature along a single reaction coordinate q as depicted in Fig. 2.3. The corresponding model parameters are listed in Table 2.1. A Gaussian wave packet in the upper diabatic state (the excited state) $|1\rangle$ is prepared by a δ-pulse excitation from the lowest vibrational level of the ground state $|\mathrm{g}\rangle$ of the system

$$\rho_{1M1N}(t = 0) = \langle 1M|\mathrm{g}0\rangle\langle \mathrm{g}0|1N\rangle. \tag{2.37}$$

Table 2.1: Parameters used in Chapter 2 for the one-mode model. The configuration labels according to Fig. 2.3 are marked by bold letters.

Parameter	Used value(s)
System frequency, ω_0	0.1 eV ($\approx$ 800 cm^{-1})
Change of the free energy, $\lvert\Delta G\rvert$	$2\omega_0$ (**a, c**), $2.5\omega_0$ (**b, d**)
Reorganization energy, λ	$3\omega_0$ (**a, b**), $14\omega_0$(**c, d**)
Intercenter coupling, v_{12}	$0.1\omega_0$, $0.5\omega_0$, ω_0
Damping rate, $\Gamma = \pi J(\omega_0)/\mathcal{M}\omega_0$	$0.1\omega_0$
Bath cutoff frequency, ω_c	ω_0
Bath temperature, $k_\mathrm{B}T$	$\omega_0/4$ (295 K)

The coordinate shift of $|\mathrm{g}\rangle$ with respect to $|1\rangle$ is chosen such that mainly the fourth and fifth vibrational levels of the excited state $|1\rangle$ are populated. No coupling to the ground state after the preparation of the initial state is assumed. The initial wave packet starts moving on the PESs of $|1\rangle$ and $|2\rangle$, and spreading. The relevant system part begins losing energy to the bath and dephasing. The population of $|1\rangle$ starts decaying. So the motion of the initial wave packet along the coordinate models the ET dynamics between the centers.

First, let us compare the population dynamics with RWA, SA and DDA, and the dynamics calculated without all these approximations. Very similar and more detailed comparison has been done only with RWA in a recent study by Egorova *et al.* [23]. Figure 2.4 shows such a comparison of the population decay of the upper state with strong intercenter coupling V in configuration (a) (see Fig. 2.3). Typical for the DDA is the wrong long-time behavior of the dynamics which is in agreement with the conclusion in Ref. [23]. In contrast, the SA results in deviations for short times. The simultaneous use of DDA and SA keeps the features of both approximations. Showing no qualitative difference from the pure case of DDA the application of DDA with RWA results in a slightly smaller deviation from the correct population dynamics. This strange effect can be regarded as a case of error cancelation.

In the following we compare the population dynamics in the two-center electron transfer system using three different intercenter coupling strengths V and four different configurations of the two harmonic PESs. Beginning our analysis with the weak coupling case $v_{12} = 0.1\omega_0$ it is expected that a perturbation expansion in V yields almost exact results. This is the reasoning why the DR0 term, which is easy to implement, has been used in earlier work [77, 75, 62, 27, 121, 122].

In configuration (a) the eigenenergies of the two diabatic PESs are in resonance. For example, the first vibrational eigenenergy of the first center equals the third vibrational eigenenergy of the second center. It is important to note that in this configuration no vibrational level of the first center is below the crossing point of the two PESs. The calculations using ER and DR0 as well as DR1 give almost identical results, see Fig. 2.5 (a). For long times DR0 deviates a tiny bit. Redfield theory in ER is known to give the correct

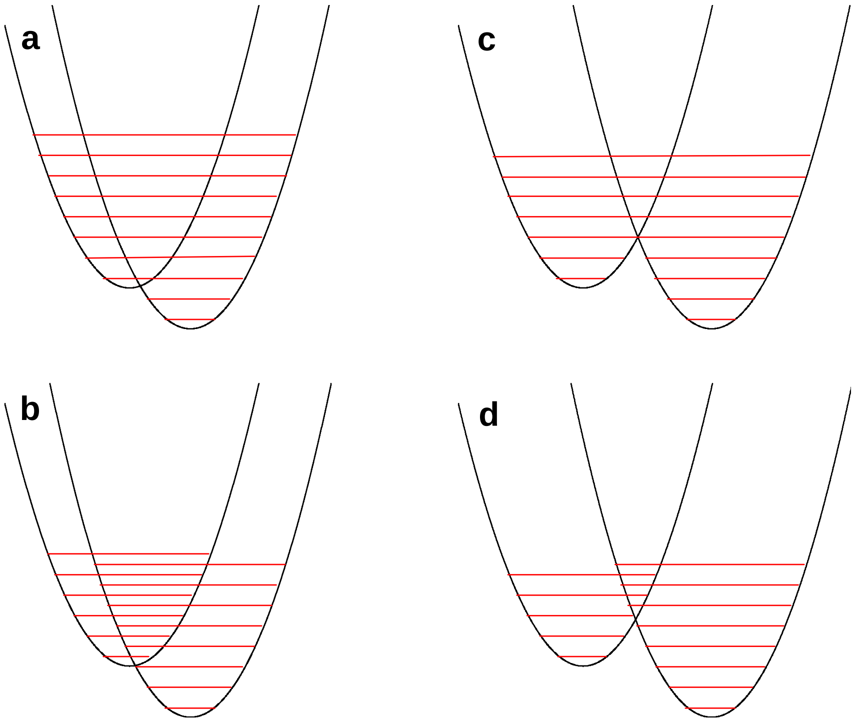

Figure 2.3: The four different configurations of the two diabatic harmonic potentials $|1\rangle$ and $|2\rangle$ as discussed in the text, with the vibronic energy levels in DR.

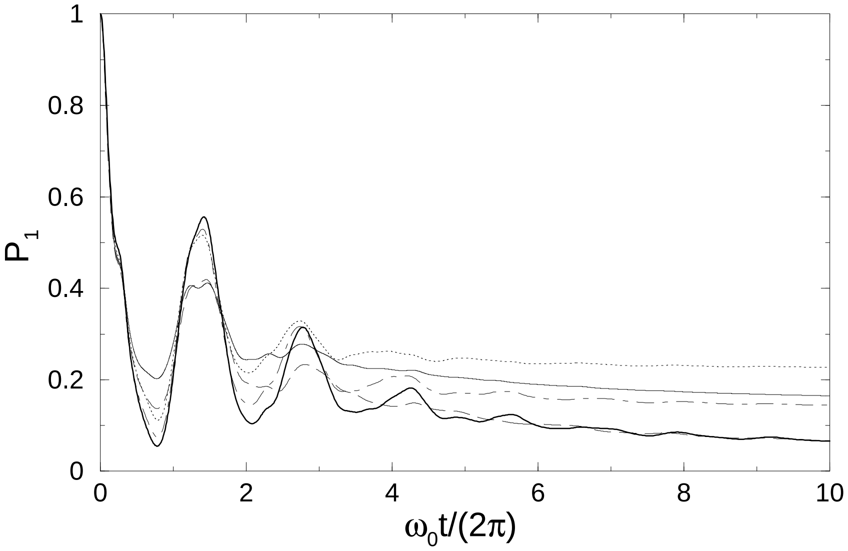

Figure 2.4: Comparison of various approximations in the framework of the Redfield theory. The population of the upper state calculated with no approximations is drawn in thick solid line. Dashed line shows SA, dotted line DDA; thin solid line is drawn for DDA together with SA, and dot-dashed for DDA with RWA.

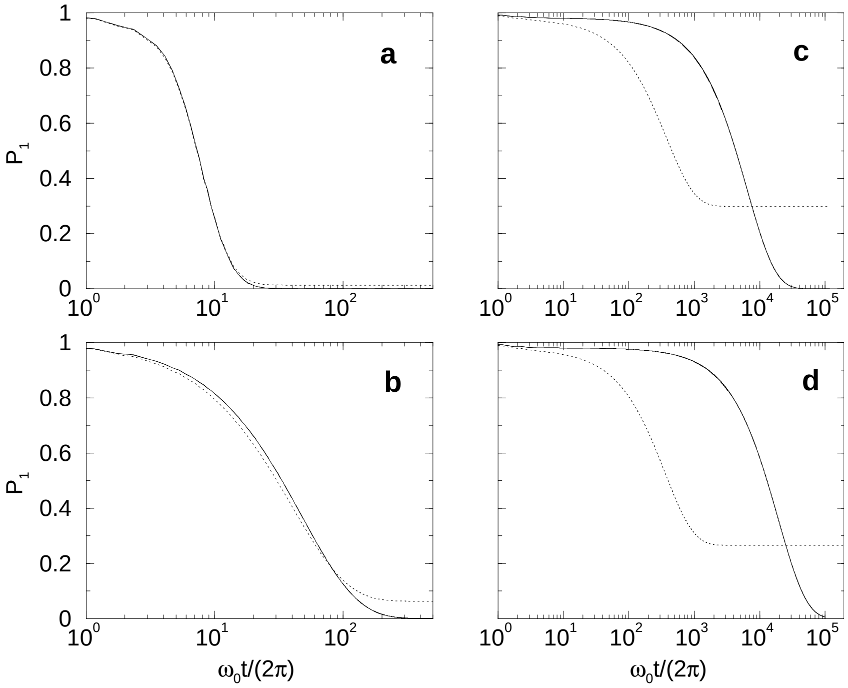

Figure 2.5: Time evolution for small intercenter coupling and for the four different configurations. The results in ER are shown by the solid line while the results in diabatic basis are shown by dotted (zeroth-order) and dashed (first-order) lines. The results for ER and DR1 are indistinguishable for small intercenter coupling. Note the logarithmic time scale.

long-time limit (up to the Lamb shift).

Configuration (b) differs from the first one by shifting the first PES up by $\omega_0/2$. As shown in Fig. 2.5 (b) the ER and DR1 results again agree perfectly. On the other hand, the DR0 results are a little bit off already at early times and the equilibrium value departs from the correct value much more than in the first, on-resonance configuration.

Shifting the PESs further apart than in (a) yields configuration (c). The energy levels are again on resonance but this time two vibrational levels of the first center are below the curve-crossing point, i.e. there is a barrier for low-energy parts of the wave packet. As shown in Fig. 2.5 (c) DR1 and the ER results agree perfectly once more. The DR0 results are terribly off. The long-time population of the first center which should vanish for the present configuration stays finite. If we increase the energy of the first PES by $\omega_0/2$ to obtain configuration (d) DR0 fails again while DR1 gives correct results in comparison to the ER, see Fig. 2.5 (d).

To understand the large difference between DR0 and DR1 let us have a closer look at the final result for the matrix elements of Λ, Eqs. (2.32) and (2.33). The DR0 contribution (2.33) is independent of the intercenter coupling V. The system part of the system-bath interaction K allows only for relaxation within each center. So there is no mechanism in the dissipative part which transfers population from one center to the other. This

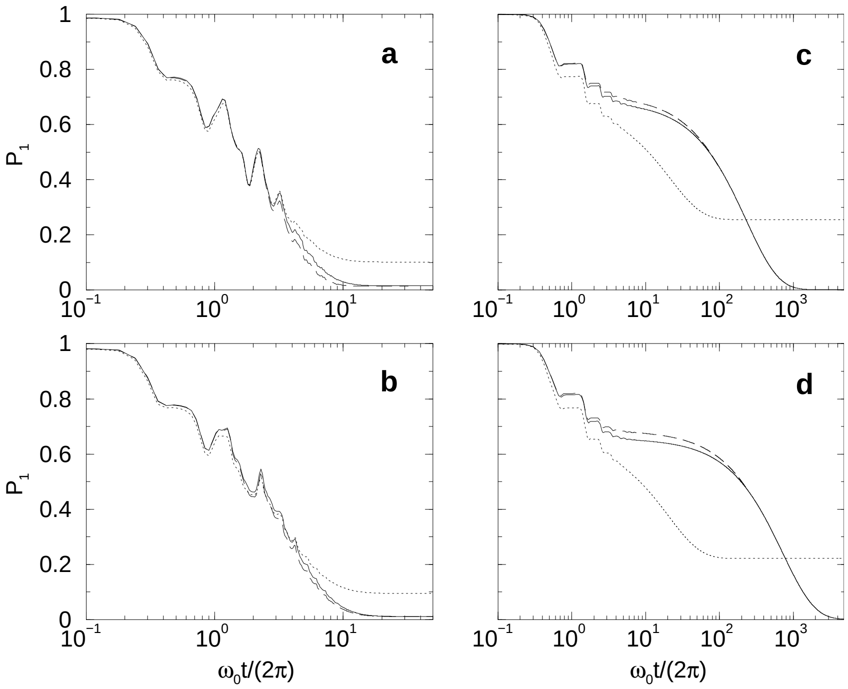

Figure 2.6: Time evolution for medium intercenter coupling.

transfer has to be done by the coherent part of the master equation. But the coherent part cannot transfer components of the wave packet with energy below the crossing point of the PESs. As tunneling is almost completely suppressed, those components of the wave packet cannot leave their center anymore although the corresponding PES might be quite high in energy. This results in the failure of DR0 for the configurations with barrier: Parts of the wave packet get trapped in the two lowest levels of the left center. From Eq. (2.32) one can explain why in the on-resonance case the DR0 results are in better agreement with the correct results than in the off-resonance case. In this configuration some of the DR1 terms are very small and so the DR1 correction is smaller.

Now we discuss the medium coupling strength $v_{12} = 0.5\omega_0$ (see Fig. 2.6). The results for configurations (a) and (b), i.e. without barrier, look quite similar. In both cases the ER and DR1 results agree very well for short and long times. At intermediate times there is a small difference. The DR0 results already deviate at short times and for long times there is too much population in the left (higher) center. For configurations (c) and (d), i.e. with barrier, again the ER and DR1 results coincide for small and long times. DR0 is off already after rather short times and the long-time limit is again wrong.

For strong coupling $v_{12} = \omega_0$ (see Fig. 2.7) the behavior of the results is quite similar to the medium coupling. For configurations (a) and (b) the difference at intermediate times is a little larger, so is the deviation of the long-time DR0 limit. For configurations (c) and (d) with barrier there is also a discrepancy for DR1 already at short times and the correct long-time limit is not reached exactly. But the disagreement is surprisingly small for the strong coupling. Overall DR1 still looks quite reasonable while the DR0 results

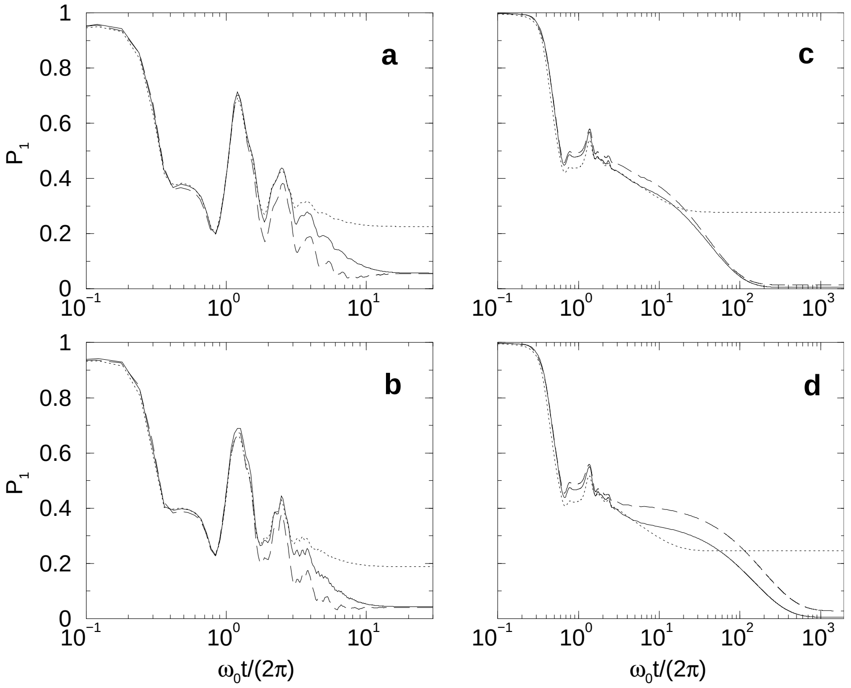

Figure 2.7: Time evolution for strong intercenter coupling.

are completely off.

2.7 Transfer mechanisms within the first-order expansion of the relaxation operator

As already noted most physical quantities, e.g. the population of a diabatic state, are obtained by projecting the RDM onto the diabatic basis. Therefore, one can take advantage of the analytical result for the DR1 contribution in the relaxation operator Λ in order to analyze the limits of validity of DDA.

Inspecting Eq. (2.32) one can see that all diabatic levels contribute to each matrix element of Λ, i.e. all diabatic levels can mediate population transfer between donor and acceptor. This is not the case in the DR0 term (2.33) where only two levels give rise merely to population decay (damping) within one diabatic state. Thus, the only mechanism for population transfer in DDA arises from the coherent term in Eq. (2.9).

The contribution of the DR1 term in the relaxation operator Λ can be viewed as a sequence of two one-quantum processes. The first can be thermal activation from a level $|n\rangle$ due to the bath (Fig. 2.8 a). According to the selection rule $\Delta M = \pm 1$ a neighboring vibronic level $|j\rangle$ from the same diabatic state is virtually occupied. After that the population is transfered coherently to such a level $|m\rangle$ in the other diabatic state with which the Franck-Condon overlap is sufficiently large. Alternatively, as seen in Eq. (2.32) the backward sequence is possible as well, i.e. coherent transfer from $|n\rangle$ to $|i\rangle$ followed

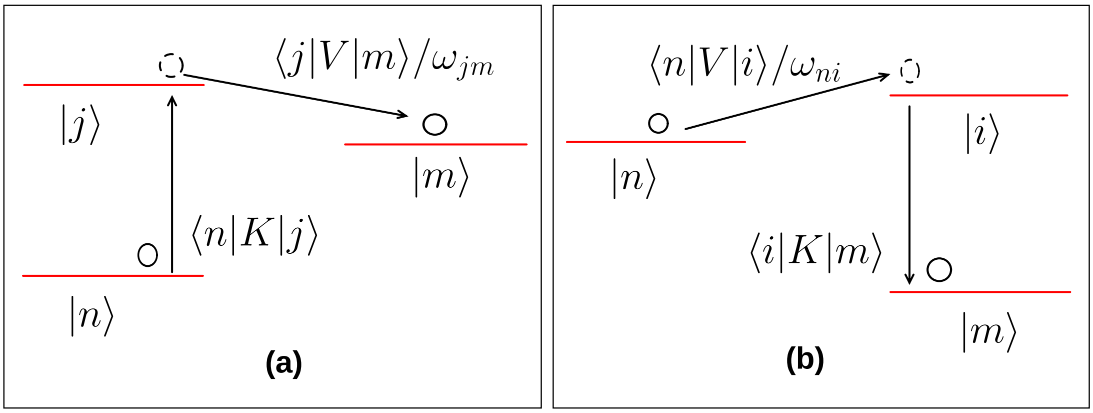

Figure 2.8: Schematic representation of the mechanisms for population transfer within DR1.

by damping down into the next $|m\rangle$ (Fig. 2.8 b). Besides these two possibilities there can be two other routes not shown in Fig. 2.8. These are thermal deexcitation from a higher lying $|n\rangle$ to $|j\rangle$ and then a coherent transfer according to case (a). Respectively, there can occur excitation of $|i\rangle$ to a higher $|m\rangle$ in case (b).

In addition Eq. (2.32) allows for classification of cases for various configuration parameters of the relevant system and for a rigorous determination of the validity limits of DDA. In particular, one has to regard cases in which the coherent transfer mechanisms are hindered, e.g. low levels with inefficient Franck-Condon overlap.

2.7.1 Configurations with barrier in the normal region

This is the case in which $\lambda \gg |\Delta G^0|$. The lowest levels in the upper diabatic state have no Franck-Condon overlap with the levels of the lower diabatic state. Thus, after very fast vibrational relaxation (damping) taking about 10 vibrational periods the lowest level of the upper state is predominantly occupied and in this way the population is trapped before significant coherent transfer has taken place. This short-time phenomenon is less pronounced for larger intercenter coupling whereby coherent mechanisms start to dominate over damping, and hence over trapping at early times of the dynamics (Fig. 2.6 c, d). If the DR1 term is taken into account the trapped population can be transfered to the donor state on a much larger time scale via thermally assisted channels as already discussed above in this section. Regarding the latter two statements, note the plateau-like feature after 10 vibrational periods when coherent mechanisms become slower and DR1 starts to prevail (Fig. 2.6 c, d).

A very interesting situation occurs if the diabatic levels of the donor and of the acceptor states are not in resonance. With DDA such a detuning can influence only the coherent term, and as seen in Fig. 2.5 (c, d) and Fig. 2.6 (c, d), no major difference between the in- and off-resonance cases can be detected. Nevertheless, the dynamics with inclusion of DR1 differs due to the factors $C(\omega_{mn}) - C(\omega_{jn})$ and $C(\omega_{mn}) - C(\omega_{mi})$ in Eq. (2.32)

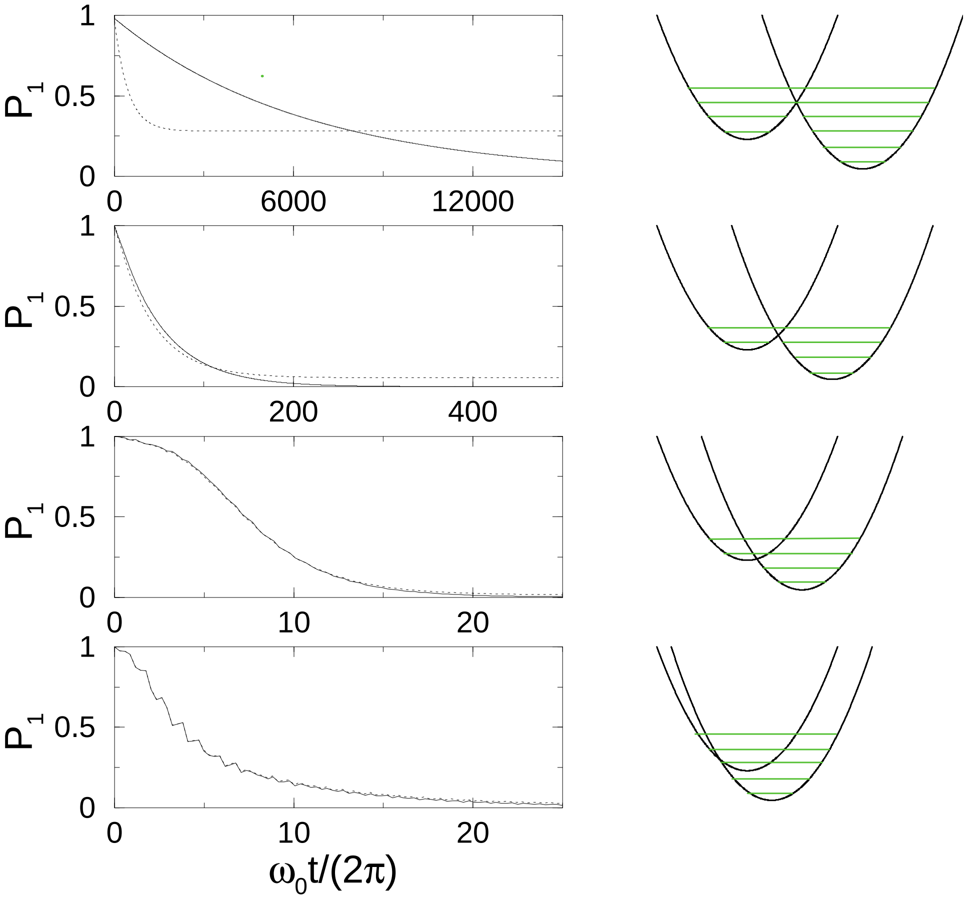

Figure 2.9: Population dynamics of the upper localization center for different values of the reorganization energy and weak intercenter coupling ($v_{12} = 0.1\omega_0$) calculated with DDA (dotted lines) and without DDA (solid lines). The first and the third configurations are identical with cases (c) and (a) respectively from Fig. 2.3 and the last configuration is in the Marcus inverted region ($\lambda = 0.5\omega_0$).

some of which vanish in case of resonance, i.e. $|m\rangle$ and $|j\rangle$ or $|n\rangle$ and $|i\rangle$ respectively, have equal energies, and do not contribute in the transfer process. It can thus be concluded that DDA is better behaved in the case of resonance configurations.

To sum up, the population dynamics in systems with potentials with barrier in the normal region show a good time separation between early coherent and later DR1-dependent transfer mechanisms. Tunneling (regarded as slow coherent motion) can only be efficient for more specific configurations in which non-vanishing overlap between the levels below the curve-crossing is present.

2.7.2 Barrierless configurations and configurations in the inverted region

Exploring a selection of configurations in the normal and in the inverted region (Fig. 2.9) it was possible to verify that the DDA is valid not only in the inverted region but also in the normal region without barrier. In both cases the configurations are characterized by a very strong Franck-Condon overlap between the diabatic levels in the donor and the acceptor states. This enables very fast coherent population transfer. Evidence for the dominating coherent motion are the multiple revivals of population on the donor (Fig. 2.6 a, b). Provided that the damping in the acceptor state is present, the system approaches its equilibrium state before the coherences have completely decayed and before the DR1 term has contributed substantially. This is the reason why in this regime the transfer rate is determined by the damping rate. In addition, the distinction between the cases in- and off-resonance has no relevance to the transfer mechanism either. For sufficiently small value of the intercenter coupling the DR1 and higher order terms give minor contribution and the DDA (2.32) is valid. However, for large intercenter coupling the perturbation theory and particularly DDA fail and one cannot separate and examine contributions in Λ in this manner.

2.8 Summary

In addition to the approximations in Redfield theory, i.e. second-order perturbation expansion in the system-bath coupling and Markov approximation, we have applied perturbation theory in the intercenter coupling. It has been shown for two coupled harmonic surfaces that the zeroth-order approximation DR0, which is equivalent to DDA, can yield wrong population dynamics even for very small intercenter coupling. These artifacts disappear using the first-order theory DR1.

For configurations without barrier it is possible to use DR0 for weak to medium intercenter coupling. This of course depends on the accuracy required especially for the long-time limit. In all other cases one should either use the exact ER or DR1. Although the first-order results are not exact for medium and strong intercenter coupling these calculations have at least two advantages. First of all, one does not need to calculate the eigenstates and eigenenergies of the full system Hamiltonian H_S. For small systems like two coupled harmonic surfaces on one reaction coordinate this calculation is of course easy. But if one wants to study larger systems like molecular wires [20, 25] and/or multi-mode models [121, 122, 123] this is no longer a trivial task. The second advantage is related to the fact that in all transfer problems one is mainly interested in properties which are defined in a local basis, e.g. the population in each subsystem at any moment in time. If one uses the ER one has always to transform back to the DR in order to calculate these properties. So for large-scale problems using a DR together with the first-order perturbation in V should be advantageous.

In a sense the present study is an extension of the investigation performed by Davis *et al.* [20]. They compared ER and DR for a two-site problem. Here we looked at a more general multilevel system and also calculated the first-order perturbation. In their model they do not have a reaction coordinate and therefore no barrier. Their findings correspond more to cases (a) and (b) discussed previously. Besides the agreement in the case of small intercenter coupling they also found good agreement in the high-temperature limit. Using our model this statement could not be confirmed for a general configuration, although there might be configurations where it would be true.

In Ref. [127] the authors followed a strategy different from the present work. They also studied two coupled harmonic oscillators modeling two coupled microcavities, but only one cavity was coupled to the thermal bath directly. This should not effect the questions studied here. With a transformation to uncoupled oscillators they effectively reduced the intercenter coupling to zero. The result [127] is then exact for arbitrary V. The disadvantage of this strategy is that it is not easy to extend to larger systems. The advantage of the presently developed first-order expansion in V is its general applicability to problems of any size.

Chapter 3

Numerical methods

3.1 Introduction

An analytical solution of the Redfield QME is possible only for a limited number of trivial problems, e.g. the damped harmonic oscillator or a single spin in an environment. Modeling real systems one has to approach the solution numerically. Already for moderately large systems this task becomes computationally very demanding or even intractable, and therefore requires efforts in reducing the numerical complexity of the RDM propagation. Straightforward diagonalization of the Liouville superoperator can be used in case of a time-independent Hamiltonian. In this way the rates, i.e. the characteristic inverse times of an exponential decay of the occupation probability of the excited states, can be obtained. Such an approach involves a huge number of floating point operations and the overall computational effort will scale as $\mathcal{N}^6$ where $\mathcal{N}$ is the size of the basis of vibronic states. Furthermore the direct diagonalization can be numerically unstable, but nevertheless has been successfully used [47]. Another strategy [38] suggests solving $\mathcal{N}^2$ ordinary differential equations and requires products between the Liouville superoperator and the RDM which scale as $\mathcal{N}^4$. This is still a very expensive method for simulation of multi-level systems.

Assuming a bilinear system-bath coupling the numerical effort can be reduced considerably by rewriting the Redfield equation in such a form (2.9) that only matrix-matrix multiplications are needed [91] rather than applying a superoperator onto the RDM. Hence, a computational time scaling of $\mathcal{N}^3$ and a storage requirement of $\mathcal{N}^2$ is achieved. In what follows, all approaches based on the latter scaling will be referred to as direct propagation methods.

Using stochastic wave function methods a significant reduction of the scaling of the numerical effort with increasing number of basis functions can be achieved. These methods prescribe certain recipes for unraveling of the QME and substitute the RDM by a set of wave functions which evolve partially stochastically in time. The method has the typical scaling of the well developed and optimized wave function propagators, i.e. $\mathcal{N}^2$. Between the direct and the stochastic methods to solve the Redfield equation the accuracy differs especially because direct RDM integrators are numerically “exact” while the stochastic wave function simulation methods have statistical errors. For small and medium size problems direct propagators can be prefered. Simulations based on the Lindblad QME (2.7) with use of both direct and stochastic methods have already been compared [102,11].

When using stochastic methods for wave function propagation one has to solve Schrödinger-type equations with a non-Hermitian Hamiltonian. For that purpose the same algorithms of the direct propagators can be used. In this sense the direct methods are also of importance for solving Redfield equations by means of stochastic wave function methods. Stochastic unraveling methods will be discussed in detail in Sec. 3.5 and used for some applications in Chapter 4.

The present studies are restricted to state representation. Grid representation of the stochastic wave function is especially useful for complicated or unbound potentials. Then one can take advantage of another propagator, the split operator [31]. This approach can be advantageous for the following reasons. First, its performance does not depend on the spectral range of the Hamiltonian or Liouville superoperator. Second, the most demanding fast Fourier transformations (FFTs) scale with the basis size as $\mathcal{N} \ln \mathcal{N}$, i.e. less than $\mathcal{N}^2$ for the methods in state representations. Typical drawback of this approach is that it cannot be applied with Hamiltonians which have mixed terms in coordinate and momentum operators.

More recently the multi-configuration time-dependent Hartree method has been established to treat density matrix operators [94]. This method might be favorable for multi-dimensional problems, especially dynamics of chemical reactions.

3.2 Scaling properties of the Redfield quantum master equation

The representations introduced in Chapter 2 allow us to consider the numerical effort for a single computation of the right hand side of Eq. (2.9), respectively of $\mathcal{L}\rho(t)$ in Eq. (2.10). In the DR its computation can be approached using two different algorithms. It is possible to perform matrix-matrix multiplication only on those elements of K and Λ which have nonzero contributions to the elements of $\mathcal{L}\rho(t)$ (Fig. 3.1, solid line). This is advantageous because of the tridiagonal form of K in diabatic representation and shows the best scaling properties, namely $\mathcal{N}^{2.3}$. In the same representation but with the full matrix-matrix multiplications in Eq. (2.9) (Fig. 3.1, dashed line) the performance is slightly worse than the same operation in adiabatic representation (Fig. 3.1, dotted line) although the scaling behavior is the same, i.e. $\mathcal{N} = 2$. This is due to the non-diagonal Hamiltonian H_S in the former case that requires an additional matrix-matrix multiplication for the computing of the coherent term in Eq. (2.9). Below we will perform the full matrix-matrix multiplication to evaluate $\mathcal{L}\rho(t)$ in both representations. We do this to concentrate on the various propagation schemes, not the unequal representations. Nevertheless, there are performance changes in the different representations because of the disparate basis functions and forms of the operators in these basis functions.

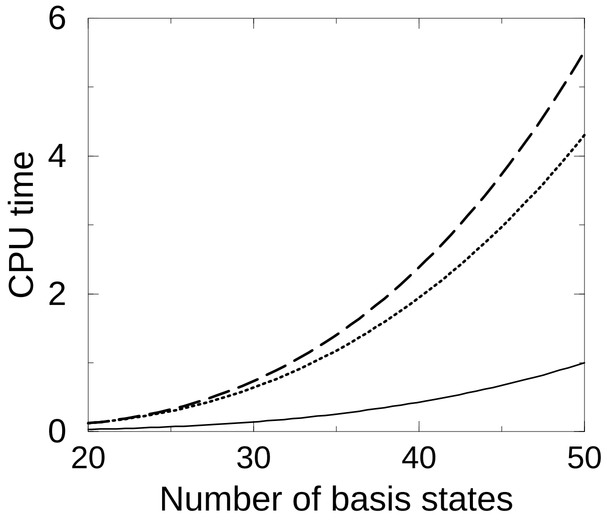

Figure 3.1: Scaling behavior of the product $\mathcal{L}\rho(t)$. Solid line – tridiagonal form of K in diabatic representation, dotted line – adiabatic representation, dashed line – diabatic representation with full matrix-matrix multiplications. The CPU time is scaled so that it is equal to 1 for $\mathcal{N} = 50$ in diabatic representation.

3.3 Direct reduced-density-matrix propagators

In the present section a variety of numerical schemes for solution of the Liouville-von Neumann equation will be tested and compared. The performance of the well-known Runge-Kutta (RK) scheme is studied in two different implementations: as given in the *Numerical Recipes* [93] and by the *Numerical Algorithms Group* [84]. In addition to these general-purpose solvers there are more special algorithms which have been applied previously to the time evolution of wave packets and density matrices. For density matrices these are the short-iterative-Arnoldi (SIA) propagator [91, 90], the short-time Chebyshev polynomial (CP) propagator [38], and the Newtonian polynomial (NP) propagator [7, 4]. The latter propagator is also used as a reference method because of its high accuracy.

Next, a symplectic integrator (SI), which was originally developed for solving classical equations of motion and extended to wave packet [37] and density matrix propagation [49], is tested.

A possible alternative to the Chebyshev scheme is the application of Legendre polynomials [58]. Both types of polynomials are special cases of the more general hypergeometric polynomials (Jacobi polynomials) which gives the hint that the latter can be used for interpolating time propagators as well. Legendre and Jacobi polynomials are not applied in the current work.

3.3.1 Runge-Kutta method

The RK algorithm is a well-known tool for solving ordinary differential equations. Thus, this method can be successfully applied to solve a set of ordinary differential equations for the matrix elements of Eq. (2.9). It is based on a few terms of the Taylor series expansion. In the present work we use the FORTRAN77 implementation as given in the *Numerical Recipes* [93] which is a fifth-order Cash-Karp RK algorithm and will be denoted as RK-NR. As alternative the RK subroutine D02PDF from the *Numerical Algorithms Group* [84] which is based on RKSUITE [10] was tested. It will be referred to as RK-NAG. Both RK-NAG and RK-NR involve terms of fifth order and use a prespecified tolerance τ as an input parameter for the time step control. The tolerance τ and the accuracy of the calculation are not always simply proportional. Usually decreasing τ results in longer CPU times.

In Ref. [104] a time step control mechanism different from those used in RK-NAG and RK-NR was tested. Discretizing the time derivative in Eq. (2.9) and requiring

$$\left| \frac{\rho(t_{i+1}) - \rho(t_i)}{\Delta t} + \mathcal{L}\rho(t_i) \right| < \tau \tag{3.1}$$

one only has to call the propagation subroutine once and to store the previous RDM. In addition one has to calculate the action of the Liouville superoperator $\mathcal{L}$ onto the RDM but the numerical effort for this is small compared to a call of the propagation subroutine. It was shown in Ref. [104] that this time step control is the most efficient for propagation with the coherent terms in Eq. (2.9) only but disadvantageous for problems with dissipation. This is the reason why we do not include this algorithm in the present study.

3.3.2 Short iterative Arnoldi propagator

The SIA propagator [91, 90] is a generalized version of the short iterative Lanczos propagator [66] to non-Hermitian operators. With the short iterative Lanczos algorithm the wave function can be propagated by approximating the time evolution operator in Krylov space, which is generated by consecutive multiplications of the Hamiltonian onto the wave function. In analogy the Krylov space within the SIA method is constructed by recursive applications of the Liouville superoperator onto the RDM $\rho_n = \mathcal{L}^n\rho(t)$. In this way it is tailored to the RDM at every moment in time. The Liouville superoperator, denoted by l in Krylov space, has Hessenberg form

$$\mathcal{L} \approx V l V^{\mathrm{T}} \,, \tag{3.2}$$

where the orthogonal transformation matrix V is constructed iteratively using the so-called Lanczos procedure [91]. The Krylov representation l can be easily diagonalized to L with the help of a transformation matrix S:

$$e^{\mathcal{L}t} \approx V S e^{Lt} S^{-1} V^{\mathrm{T}} \,. \tag{3.3}$$

Since the diagonalization is performed in the Krylov space the numerical effort depends on its dimension which can be chosen small in practice. Having thus derived a diagonal operator e^{Lt} the calculation of $\rho(t)$ is straightforward.

3.3.3 Symplectic integrator

The SIs were originally developed for solving classical equations of motion [101]. The time evolution of a classical Hamiltonian system can be viewed as a canonical transformation and SIs are sequences of canonical transformations. Recently it was shown that the time evolution of wave packets [37] and density matrices [49] can also be performed using SIs. In order to rewrite the Redfield equations in the form of coupled canonical variables that are analogous to classical equations of motion one defines the functions [49]

$$\begin{aligned} Q(t) &= \rho(t) \ , & (3.4) \\ P(t) &= \dot{\rho}(t) \ , & (3.5) \end{aligned}$$

the operator

$$W = -\mathcal{L}^2 \ , \tag{3.6}$$

and the Hamiltonian function

$$G(Q,P) = \frac{1}{2}[P^T P + Q^T W Q] \ . \tag{3.7}$$

Doing so one obtains equations of motion analogous to the classical ones

$$\begin{aligned} \frac{d}{dt}P(t) &= -\frac{\partial G(Q,P)}{\partial Q} = -WQ(t) \ , & (3.8) \\ \frac{d}{dt}Q(t) &= \frac{\partial G(Q,P)}{\partial P} = P(t) \ . & (3.9) \end{aligned}$$

Rewriting this into the SI algorithm of order m yields [49]

$$\begin{aligned} P_i &= P_{i-1} + b_i \Delta t \mathcal{L}^2 Q_{i-1} & (3.10) \\ Q_i &= Q_{i-1} + a_i \Delta t P_i & (3.11) \end{aligned}$$

for $i = 1, \ldots, m$. Different sets of coefficients $\{a_i\}$ and $\{b_i\}$ are given in the literature. Here we choose the McLachlan-Atela fourth-order method [79]. The coefficients for this method are listed in Ref. [37]. A comparison of the McLachlan-Atela fourth-order method with the McLachlan-Atela third-order method [79] and Ruth's third-order method [101] for RDM propagation has been given elsewhere [49].

3.3.4 Newton polynomial scheme

Another way to solve Eq. (2.9) is by a polynomial expansion of the time-evolution operator. Such methods are well established and approved for wave-function propagation [66,4].

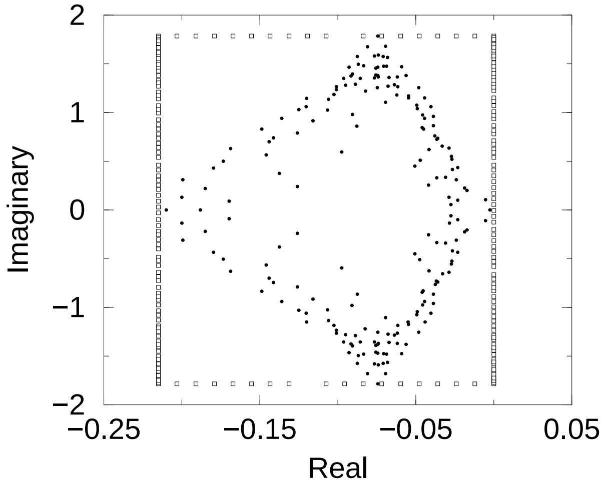

Figure 3.2: Spectrum of the scaled Liouville superoperator $\tilde{L}$ for the model of electron transfer (see the text below Eq. (3.13)). Approximate eigenvalues obtained in the Krylov subspace are plotted as dots. Open squares denote the interpolation points λ_j for the NP scheme.

Recently the Faber [43] and NP [7] algorithms have been applied to propagate density matrices and it has been shown that they behave very similarly [43]. The main idea of the NP method is the representation of the Liouville superoperator by a polynomial interpolation

$$e^{\mathcal{L}t} \approx \mathcal{P}_{N_p-1}(\mathcal{L}) \equiv \sum_{n=0}^{N_p-1} a_n \rho_n = \sum_{n=0}^{N_p-1} a_n \prod_{j=0}^{n-1} (\mathcal{L} - \lambda_j) \tag{3.12}$$

of order N_p where the ρ_n are computed recursively and a_n are the nth divided differences. The interpolation points λ_j can be chosen to form a rectangular area in the complex plane (see Fig. 3.2) which contains all eigenvalues of $\mathcal{L}$. This interpolation scheme is uniform, i.e. the accuracy in energy space is approximately the same in the whole spectral range of $\mathcal{L}$. This is in contrast to schemes such as the SIA propagator which are nonuniform approximations. A consequence of this property is the very high accuracy which can be achieved with uniform propagators. This is why we take a high-order NP expansion as reference solution. Since the quality of the approximation of the time evolution operator is equivalent to a scalar function with the same interpolation points λ_j, one can, before performing the actual calculation, check the accuracy on a scalar function. For the calculation with the NP propagator we set the truncation limit of the expansion to 10^{-15}, i.e. the sum in Eq. (3.12) is truncated when the residuum fulfills $a_n||\rho_n|| < 10^{-15}$ [4].

3.3.5 Chebyshev polynomial scheme

As a last contribution to the present study we will examine the CP propagator. Recently it was studied by Guo *et al.* [38] for density matrices. The Liouville superoperator is approximated by a series of CPs $T_k(x)$. Generally the CPs diverge for non-real arguments. For propagators of the kind e^{-iHt} it has been shown [4] that the CPs may tolerate some imaginary part in the eigenvalues of H. The stability region has the form of an ellipse with a center at the origin and a very small half-axis in imaginary direction [4]. In contrast, the eigenvalues of the Liouville superoperator are spread over the negative real half of the complex plane and symmetrically with respect to the real axis (see Fig. 3.2). The real components for the system that we consider are one order of magnitude smaller than the imaginary components. This is why we make the expansion along the imaginary axis and use an expression similar to that already applied to wave function propagation [66]:

$$e^{\mathcal{L}t} \approx e^{L^+\Delta t} \sum_{n=0}^{N_p-1} (2-\delta_{n0}) J_n(L^-\Delta t) T_n(\tilde{L}) \ . \tag{3.13}$$

Here the expansion coefficients J_n are the Bessel functions of the first kind, and $\tilde{L}$ is the appropriately scaled Liouville superoperator: $\tilde{L} = (\mathcal{L} - L^+)/L^-$, where L^- and L^+ are the half span and the middle point of the spectrum of $\mathcal{L}$. Since the spectrum is symmetric with respect to the real axis, $L^+ = 0$. The time evolution of ρ is given by

$$\rho(t+\Delta t) \approx \sum_{n=0}^{N_p-1} (2-\delta_{n0}) J_n(L^-\Delta t) \tilde{\rho}_n \ . \tag{3.14}$$

The Chebyshev vectors $\tilde{\rho}_n$ are generated by means of a recurrence procedure:

$$\tilde{\rho}_n = 2\tilde{L}\tilde{\rho}_{n-1} + \tilde{\rho}_{n-2}, \quad \tilde{\rho}_0 = \rho(t) \text{ and } \tilde{\rho}_1 = \tilde{L}\tilde{\rho}_0 \ . \tag{3.15}$$

For the CP and NP methods one has to adjust the values of the spectral parameters L^- and L^+. One can obtain some knowledge about the spectrum of $\mathcal{L}$ by an approximate diagonalization, e.g. by Krylov subspace methods. For instance, Fig. 3.2 shows an approximate spectrum of $\mathcal{L}$ appropriately scaled so that all eigenvalues lie within the rectangle formed by the Newtonian interpolation points.

3.4 Performance of the direct propagators

The aim of this section is to compare the different numerical methods described above for propagating the RDM in time. The calculations were performed for both RK methods with different tolerance parameters τ and for the SI as well as the NP, CP, SIA propagators with different time steps. The number of interpolation points N_p in NP and CP propagators is 170 and 64, respectively. The summation terms in Eq. (3.12) and in Eq. (3.13) are truncated if their contribution is less than 10^{-16}. The dimension of the Krylov space for the SIA method was set to 12 because smaller as well as larger values are less efficient for the example studied here. All computations were made on Pentium III 550 MHz personal computers with intensive use of BLAS and LAPACK libraries. The code was compiled using the PGF90 Fortran compiler [88]. For estimation of the computational error of all methods the NP algorithm with 210 interpolation points was chosen as a benchmark.

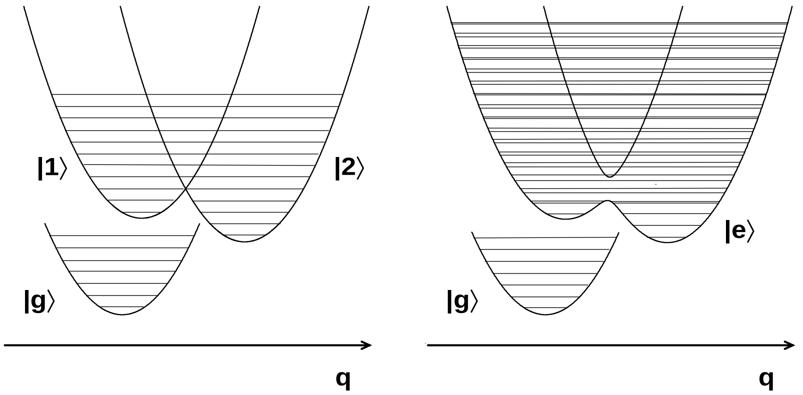

Figure 3.3: PESs for a model electron transfer system. Diabatic PESs are plotted on the left side, and the PES of the adiabatic excited state |e⟩ on the right side.

A one-dimensional model of a system with two charge localization centers ($m = 1, 2$) as presented in Fig. 3.3 is considered. The vibronic coupling of these two centers can be strong while the coupling to the bath degrees of freedom is assumed to be small. Transitions between the centers model the main physics of an electron transfer reaction. A more detailed description of the model was already given in Sec. 2.6. The temperature $T = 298$ K is used. The displacement of the PES of the ground state $|g\rangle$ with respect to $|1\rangle$ corresponds to a reorganization energy $\lambda = 1.1\omega_0$ where ω_0 is the system frequency. All other parameters are the same as for configuration (c) in Table 2.1 and for strong intercenter coupling, i.e. $v_{12} = \omega_0$. A basis size of 16 vibrational levels per center, i.e. a density matrix with $\mathcal{N} \times \mathcal{N} = 32 \times 32 = 1024$ elements, satisfies the completeness relation and presents no difficulties during the diagonalization of H_S. Using Eq. (2.9) the Redfield tensor $\mathcal{R}$ needs not be constructed explicitly. A typical computation till the equilibrium is reached takes a few hours of CPU time on the above described computers (see below for details).

In all cases the RDM was propagated for a total time period of 3×10^5 a.u. which is sufficient for complete relaxation to equilibrium. It was compared to the RDM ρ_ref evaluated by the NP algorithm at the same points in time. The relative error $\varepsilon(t)$ of each method at a certain moment in time t has been estimated using a formula similar to that proposed for wave functions by Leforestier *et al.* [66]:

$$\varepsilon(t) = \left| 1 - \frac{\mathrm{Tr}\left(\rho(t)\rho_\mathrm{ref}(t)\right)}{\mathrm{Tr}\left(\rho^2_\mathrm{ref}(t)\right)} \right| . \tag{3.16}$$

As the error ε we define the maximum value of $\varepsilon(t)$ over the total propagation time. For more details we refer to Ref. [104]. Other error measures (see for example [86,38]) can be used as well but they will have the same qualitative behavior.

As an index for the numerical effort two possibilities were explored. The first one is a direct measurement of the CPU time of the total propagation (Fig. 3.4). It may look quite different on other computer architectures or even on the same architecture but

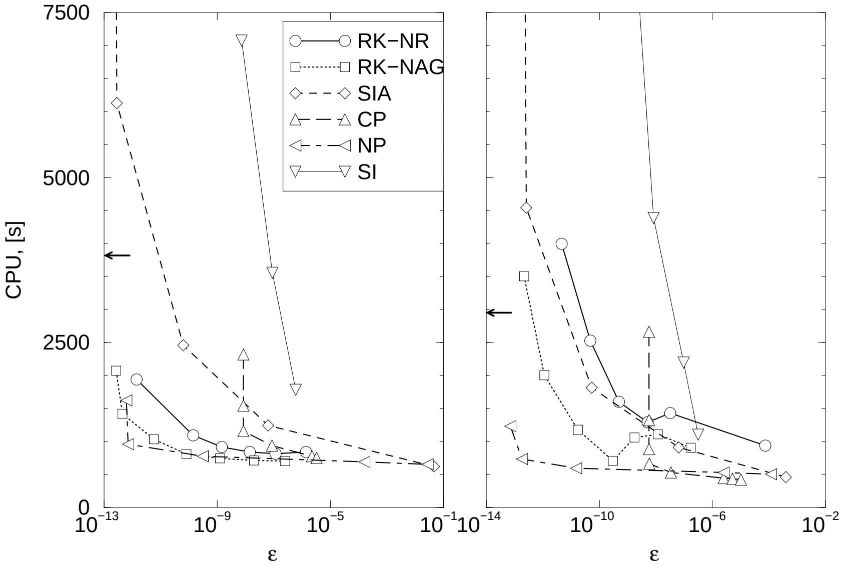

Figure 3.4: Numerical performance of different numerical propagators. Results obtained in the diabatic (adiabatic) representation are shown in the left (right) plot. The arrows represent the numerical performance for the NP propagator with 50 interpolation points and time step 100 a.u.

under changed operation conditions. An evidence of the performance (Fig. 3.4) will be expressed by means of CPU time versus the error ε.

Another approach to describe the numerical effort has been proposed [38] and is called efficiency factor. It is defined as the ratio between the time step Δt and the number of operations $\mathcal{L}\rho(t)$ within this time step. Because of the definition it is a machine independent quantity. The larger the efficiency factor, the better the performance of the algorithm. Because the RK algorithms propagate with variable time step we cannot directly use the definition of the efficiency factor. Instead we define a quantity α as the total number N_c of $\mathcal{L}\rho(t)$-evaluations divided by the total time for the propagation:

$$\alpha = N_c/(N_s\overline{\Delta t}) \ . \tag{3.17}$$

Here N_s denotes the total number of time steps. The inverse of α will have the meaning of an efficiency factor for an averaged time step $\overline{\Delta t}$. We should point out that N_c does not take into account the effort for summation of the different contributions. In particular in the case of the NP method the summation of the different terms in the polynomial expansion (3.12) can be non-negligible. This can be seen in the different relative performance of the propagators shown in Figs. 3.4 and 3.5. We consider both the CPU time and the quantity α as measures of the numerical effort.

Contributions from the algorithm to calculate $\mathcal{L}\rho(t)$ also influence the CPU time. As discussed above, in all computations represented in Figs. 3.4 and 3.5 the full matrix-matrix multiplications in Eq. (2.9) were performed. The performance of the CP, NP, SI and SIA methods is only influenced very little by the choice between diabatic and adiabatic repre-

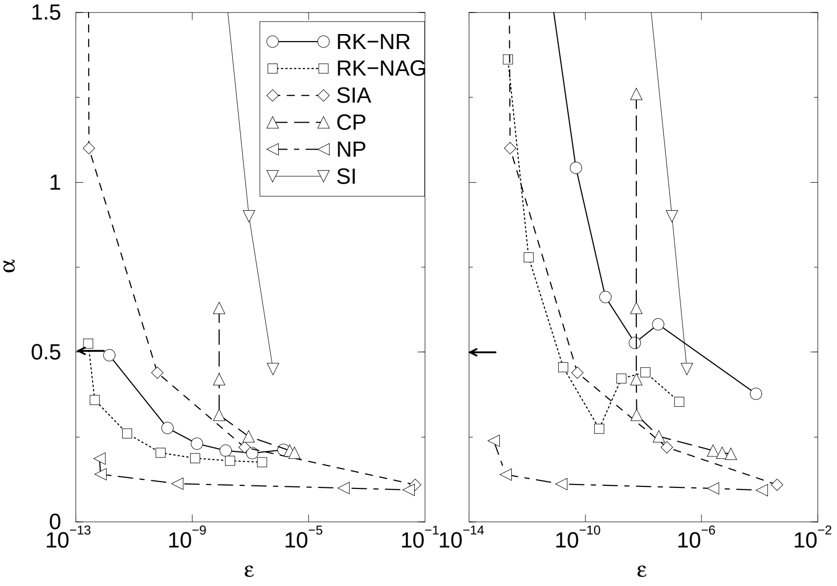

Figure 3.5: Numerical effort of different numerical propagators as defined in Eq. (3.17) in the diabatic (adiabatic) representation shown in the left (right) panel. The arrows represent the numerical performance for the NP propagator with 50 interpolation points and time step 100 a.u.

sentation. Both RK implementations are less efficient in the adiabatic than in the diabatic representation, though the RK-NAG scheme has still the best performance besides the NP algorithm. The RK-NR scheme has an advantage for computation in diabatic rather than in adiabatic representation especially for medium precision requirements. In that range the performance curves of the RK methods exhibit a shoulder for the adiabatic case which seems to result from a numerical artifact.

Because the error of the SIA algorithm is not uniformly distributed in energy space [57] we could expect some difference in its performance in diabatic and adiabatic representation. But because the coupling v_{12} chosen here is not very large, the eigenstates of the coupled system are just slightly disordered (see Fig. 3.3, right plot) and hence the performance of the SIA algorithm is almost not changed.

The uniformity, stability and high accuracy of the CP propagator for wave functions is well known [66,57,86]. The CP approach to density matrix propagation was introduced by Guo and Chen [38]. Using a damped harmonic oscillator as model system and starting from a pure state they established that the relative error can reach the machine precision limits (10^{-15}) for sufficiently small stepsize. However, for the system of coupled harmonic potentials studied here and using an initial RDM with non-zero off-diagonal elements the error saturates at $\varepsilon \approx 10^{-8}$ (see Fig. 3.4). It was not possible to decrease this saturation limit neither by increasing the order of the CP nor by decreasing the time step. This limit seems to depend strongly on the imaginary part of the eigenvalues of $\mathcal{L}$. For large time steps the CP method loses its stability and one needs to estimate the efficiency range of

N_p, Δt and L^-. Turning off the dissipation we could reach much higher accuracy with the CP propagator as expected.

The SI is easy to implement. The expansion coefficients are fixed and can be taken from literature. At the same time the fixed coefficients seem to limit the accuracy. For not too high accuracy the performance of the SI is as good as that of the other propagators in adiabatic representation. In diabatic representation its performance is a little worse. But we were not able to achieve very high accuracy with this method. This might be due to the special version, the fourth order McLachlan-Atela method, which we chose. It is also important to note the relatively bad stability limit ($\varepsilon \approx 10^{-6}$) of the present SI propagator. It is known [37] that the second order Leapfrog symplectic method is stable even for large time steps resulting in very low accuracies. Higher order SI methods, like the fourth order McLachlan-Atela method, are designed to achieve higher accuracy at relatively low costs rather than to explore a broad stability range. Extensive studies of the accuracy and stability of various SI methods have been reported [37, 49].

As already highlighted [43] the NP scheme is very stable for arbitrary spectral properties of $\mathcal{L}$. The only restriction is that the spectrum must be confined within the area formed by the interpolation points. In our investigation the NP propagator performs with a good accuracy for $N_p = 170$ and time steps of 1500 a.u. which is 10 times larger than the step size of the CP scheme. Higher order expansions might be even more efficient but the numerical implementation gets tricky and easily unstable. For time steps of 100 a.u. with $N_p = 50$ the NP algorithm is already numerically exact but computationally very expensive (see the arrows in Fig. 3.4 and Fig. 3.5). For problems with time-dependent Hamiltonians (e.g. non-stationary external fields with relatively small amplitude) the RK and SIA methods will be more efficient with small time step.

At the end we should point out that there exists no ultimate method to determine the performance of a certain numerical approach which could be valid for different platforms. Tuning and optimization features are generally not portable and this may cause even different scaling behavior and hence a different method of preference. That is the reason why the generality of the results is limited to similar computation platforms and even to systems with similar properties of the corresponding Liouville superoperator. But on the other hand this study can give hints on the performance of the different algorithms in general.

3.5 Stochastic wave function methods

Stochastic unraveling (sometimes also called Monte Carlo wave function method) is an efficient numerical tool for solving QMEs. This method allows to simulate very large and complex systems with many degrees of freedom. Instead of propagating the RDM which describes a mixed state of the relevant system one considers an ensemble of pure states, the so called quantum trajectories. Each pure state, described by a wave function, experiences fluctuations in the bath and hence evolves stochastically in time. Formally, the time evolution of every single quantum trajectory is governed by a stochastic Schrödinger equation (SSE). Averaging of a infinitely large ensemble of quantum trajectories yields exactly the deterministic RDM. The stochastic approach might provide physical interpretation of experiments detecting macroscopic fluctuations (e.g. photon counting) in various quantum systems [89] where ensemble descriptions based on RDM fail.

The unraveling schemes originate from the quantum optics community [19, 29, 35, 30, 121, 89] but they have been successfully applied to ET problems [121, 122, 123] as well. These schemes have been restricted to QMEs of Lindblad form (2.7) that ensures that the RDM stays Hermitian, normalized and positive semidefinite at all times and for any system parameters or initial conditions. The increasing interest in descriptions beyond the Lindblad class such as the quantum Brownian motion [112, 111], the Redfield formalism [74], non-Markovian schemes [80, 12], etc. resulted in various efforts to develop new stochastic wave function algorithms. Strunz *et al.* [112, 111] extended the QME for Brownian motion to a non-Markovian QME and then applied a quantum state diffusion algorithm. A similar approach was also proposed by Gaspard and Nagaoka [32]. Very recently Stockburger and Grabert [110] developed a method on how to exactly represent the RDM of a system coupled to a linear heat bath in terms of SSEs. The numerical properties of this approach need to be explored. Breuer *et al.* [12] extended a scheme, which they had used to calculate the multitime correlation functions [11], to the unraveling of QMEs. Their technique is based on doubling the Hilbert space. Instead of a single stochastic wave function $|\psi\rangle$ one has a pair of them, i.e. $(|\psi\rangle, |\phi\rangle)$ [12]. The RDM is reconstructed by means of the ensemble average $\rho = \mathrm{M}\left[|\psi\rangle\langle\phi|\right]$. One problem of this scheme is that the Hermiticity of the RDM is conserved only on an average and not for every single trajectory. Thus, the deviation from Hermiticity is a quantity with statistical error and one has to perform a huge number of realizations in order to achieve a good convergence. Since stability and efficiency are crucial issues for unraveling algorithms we propose in Subsec. 3.5.2 an alternative approach that fulfills these criteria.

3.5.1 Unraveling of Lindblad quantum master equations

The RDM can be replaced by an ensemble average of pure states $|\psi\rangle$, i.e. $\rho = \overline{|\psi\rangle\langle\psi|}$. If $\xi_k(t)$ are possibly complex noise variables characterized by their average [28]

$$\overline{d\xi_k} = 0, \quad \overline{d\xi_k^* d\xi_l} = \delta_{kl} dt \tag{3.18}$$

the relevant SSE reads

$$d|\psi\rangle = D|\psi\rangle dt + \sum_k S_k|\psi\rangle d\xi_k, \tag{3.19}$$

where D and S_k are linear operators which may depend on $|\psi\rangle$ and explicitly on time. Evaluating the differential change of the quantity $\overline{|\psi\rangle\langle\psi|}$ [108] using Eq. (3.19), keeping terms up to first order in dt with the assumption that ensemble averages always factorize, and after comparing the result with Eq. (2.7) one notices that the operators S_k must be of the form $S_k = L_k - \alpha_k$ with arbitrary scalar functions α_k. Having the latter identity one can find that $D = -iH - \frac{1}{2}\sum_k (L_k^\dagger L_k - 2\alpha_k^* L_k + |\alpha_k|^2)$ [22]. Substitution into Eq. (3.19) yields

$$d|\psi\rangle = -iH_{\mathrm{S}}|\psi\rangle dt - \sum_k \left[\frac{1}{2}\left(L_k^\dagger L_k - 2\alpha_k^* L_k + |\alpha_k|^2\right)|\psi\rangle dt + (L_k - \alpha_k)|\psi\rangle d\xi_k\right]. \tag{3.20}$$

According to Ref. [22] the last equation describes a quantum diffusion process if the leading terms in $d\xi_k$ are first order in $\sqrt{dt}$. When $d\xi_k$ get finite number of values, e.g. $\pm\sqrt{dt}$, the process results in continuous trajectories but random within each infinitesimal time interval dt (for $dt \to 0$ the trajectories become smooth but still stay noisy). Diffusion methods will not be considered in the present work. However, if the leading terms in $d\xi_k$ have finite values of order unity, i.e. zeroth order in $\sqrt{dt}$, Eq. (3.20) leads to so called quantum jump methods which produce trajectories that are deterministic during finite time intervals connected by discontinuous transitions (jumps). If the jumps are specified by their jump rates p_k one can introduce the relation [22]

$$d\xi_k = \frac{dn_k - p_k dt}{\sqrt{p_k}} e^{i\varphi} \tag{3.21}$$

which obeys condition (3.18). Here $dn = 1$ indicates the occurrence of a jump. For $dn = 0$ Eq. (3.20) becomes a deterministic Schrödinger equation. Incorporating Eq. (3.21) into Eq. (3.20) gives the relation $\alpha_k = \sqrt{p_k}\exp(-i\varphi)$. One can set $\varphi = 0$ without physical consequence. Thus one obtains the final form of the SSE

$$d|\psi\rangle = -iH_\mathrm{S}|\psi\rangle dt - \sum_k \left[\frac{1}{2}\left(p_k - L_k^\dagger L_k\right)|\psi\rangle dt + \left(\frac{L_k}{\sqrt{p_k}} - 1\right)|\psi\rangle dn\right]. \tag{3.22}$$

So far the jump rates p_k remain free parameters. They can be adapted for every single trajectory so that the wave function $|\psi\rangle$ is normalized, i.e. $p_k = \langle L_k^\dagger L_k\rangle$. The numerical algorithm of this standard quantum jump method is itemized in Appendix B. It will be used for reference when comparing with the newly developed quantum jump method in Subsec. 3.5.2 and in the pump-probe simulations in Chapter 4.

3.5.2 A new unraveling scheme for generalized quantum master equations

In the following let us consider the solution $\rho(t)$ of a generalized time-local Hermiticity-conserving QME

$$\frac{d\rho(t)}{dt} = A(t)\rho(t) + \rho(t)A^\dagger(t) + \sum_{k=1}^{M}\{C_k(t)\rho(t)E_k^\dagger(t) + E_k(t)\rho(t)C_k^\dagger(t)\} \tag{3.23}$$

with the total number M of dissipative channels and arbitrary operators $A(t)$, $C_k(t)$, and $E_k(t)$. Examples for these operators are given below. Here, the operators are restricted in such a way that the norm of the solution stays conserved. For readability the time arguments shall be omitted in the following.

In order to approach the problem let us define a state vector $(|\psi\rangle, |\phi\rangle)^T$ spanning a doubled Hilbert space as proposed in Ref. [12]. In contrast to Ref. [12] the RDM shall be reproduced by an ensemble average (denoted by overbars) of outer products of the vectors $|\psi\rangle$ and $|\phi\rangle$

$$\rho = \overline{|\psi\rangle\langle\phi| + |\phi\rangle\langle\psi|}\ . \tag{3.24}$$

A particular realization (trajectory) of the stochastic process will be denoted by the pair $(|\psi\rangle, |\phi\rangle)$ and the averaging is performed over all trajectories possibly including a weighted sum over pure initial states. An advantage of this averaging is the conservation of Hermiticity for every single trajectory in contrast to Ref. [12].

For the SSEs let us consider $2M$ independent possibly complex noise variables $\xi_k^i(t)$. The superscripts $i = 1, 2$ denote which of the two terms from the Hermitian pair in the sum in Eq. (3.23) is taken and subscripts denote the various dissipative channels. All stochastic differentials $d\xi_k^i(t)$ are assumed to have zero mean, to be normalized and uncorrelated [28]:

$$\overline{d\xi_k^i} = 0, \;\; \overline{d\xi_k^{i*} d\xi_l^j} = \delta_{ij}\delta_{kl} dt \; . \tag{3.25}$$

Next, as an ansatz one constructs a SSE which propagates the pair $(|\psi\rangle, |\phi\rangle)$

$$d|\psi\rangle \;\; = \;\; D_1|\psi\rangle dt + \sum_{k=1}^{M}\sum_{i=1}^{2} S_{1k}^i |\psi\rangle d\xi_k^i \; , \tag{3.26}$$

$$d|\phi\rangle \;\; = \;\; D_2|\phi\rangle dt + \sum_{k=1}^{M}\sum_{i=1}^{2} S_{2k}^i |\phi\rangle d\xi_k^i \; . \tag{3.27}$$

The operators D_1 and D_2 govern the deterministic and the operators S_{jk}^i govern the stochastic part of the evolution. In general, they may depend on the state vector and explicitly on time. After differentiating Eq. (3.24), neglecting all terms of higher than first order in dt, and assuming that ensemble averages always factorize [22] one obtains

$$d\rho = \left[D_1\overline{|\psi\rangle\langle\phi|} + D_2\overline{|\phi\rangle\langle\psi|}\right] dt + \sum_{k=1}^{M}\left[S_{1k}^1\overline{|\psi\rangle\langle\phi|}S_{2k}^{1\dagger} + S_{2k}^2\overline{|\phi\rangle\langle\psi|}S_{1k}^{2\dagger}\right] dt + \text{ H.c.} \tag{3.28}$$

Comparing with Eq. (3.23) one notes that S_{1k}^1 has to equal S_{2k}^2 and S_{2k}^1 has to equal S_{1k}^2. Moreover, one can see that $S_{2k}^1 = C_k + \alpha_k^1$ and $S_{2k}^2 = E_k + \alpha_k^2$ with α_k^1 and α_k^2 being arbitrary scalar functions of $(|\psi\rangle, |\phi\rangle)^T$ and possibly of time. Making the latter substitutions in Eq. (3.28) yields the constraint

$$D_1 = D_2 = A - \sum_{k=1}^{M}\left(\alpha_k^{2*}C_k + \alpha_k^{1*}E_k + \alpha_k^1\alpha_k^{2*}\right) \; . \tag{3.29}$$

Any quantum jump method is specified by jump rates p_k^i which have to be real scalar functions of $(|\psi\rangle, |\phi\rangle)$. If $n_k^i(t)$ is the number of jumps in channel k due to term i up to time t, the probability for $n_k^i(t)$ to increase by one, i.e. the expectation value of both dn_k^i and $(dn_k^i)^2$, is equal to $p_k^i dt$ during the infinitesimal time interval dt. Thus, the noise variables ξ_k^i obeying the conditions (3.25) are related to $dn_k^i(t)$ as [22]

$$d\xi_k^i = \frac{dn_k^i - p_k^i dt}{\sqrt{p_k^i}} e^{i\varphi} \; . \tag{3.30}$$

The phase factor $e^{i\varphi}$ leads merely to a phase shift in the wave vectors and cancels within each realization. So we can choose $\varphi = 0$ without loss of generality. Substituting Eq. (3.30) into Eqs. (3.26) and (3.27) one finds that $\alpha_k^i = -\sqrt{p_k^i}$. So the SSEs for our quantum jump method read

$$d|\psi\rangle = \left(A + \sum_{k=1}^{M} \frac{p_k^1 + p_k^2}{2}\right)|\psi\rangle dt + \sum_{k=1}^{M}\left[\left(\frac{E_k}{\sqrt{p_k^1}} - 1\right) dn_k^1 + \left(\frac{C_k}{\sqrt{p_k^2}} - 1\right) dn_k^2\right]|\psi\rangle, \tag{3.31}$$

$$d|\phi\rangle = \left(A + \sum_{k=1}^{M} \frac{p_k^1 + p_k^2}{2}\right)|\phi\rangle dt + \sum_{k=1}^{M}\left[\left(\frac{C_k}{\sqrt{p_k^1}} - 1\right) dn_k^1 + \left(\frac{E_k}{\sqrt{p_k^2}} - 1\right) dn_k^2\right]|\phi\rangle. \tag{3.32}$$

The jump rates p_k^1 and p_k^2 still remain as free parameters. In the statistical limit their values have no influence on any averaged physical quantity. Nevertheless, it turns out that they can strongly influence the convergence behavior of the jump algorithm, i.e. they determine the statistical error of the observables calculated. A detailed discussion of this influence and utilization of such free parameters can be found in Ref. [24]. Another freedom is that Eq. (3.23) is invariant with respect to a gauge transformation of the kind $C_k \to \kappa C_k$, $E_k \to E_k/\kappa$ if κ is a real, scalar function of time. Each single realization, and hence the stochastic process, is independent of this gauge transformation. However, usage of the latter offers us no further advantages.

To ensure an efficient scheme with fast convergence one has to require that the norm of every single trajectory is constant in time. Asking for $\langle\phi|\phi\rangle$, $\langle\psi|\psi\rangle$, etc. being constant in time does not create a stable scheme but the condition of norm preservation of $|\psi\rangle\langle\phi| + |\phi\rangle\langle\psi|$

$$\mathrm{tr}\left\{\frac{d}{dt}\left[|\psi\rangle\langle\phi| + |\phi\rangle\langle\psi|\right]\right\} = 0 \tag{3.33}$$

does. Unfortunately, applying this condition does not lead to positive values of the jump rates p_k^i for all trajectories at all times. However, since the p_k^i are arbitrary real functions, they can be replaced by their absolute values. The price to pay is that we have to introduce an additional weight factor for the trajectories which jumps between one and minus one. In addition, there is a small deviation of the norm from unity because in the regions where the p_k^i are replaced by their absolute values norm conservation is no longer guaranteed. However, in all our tests this deviation was far below 1% and neither affected numerical stability nor efficiency. The negative weights are actually needed to reconstruct RDMs which are, in general, not positive semidefinite. If the RDM stays positive semidefinite during its entire time evolution the negative weights of some trajectories are not needed, i.e., all trajectories can be normalized to unity and represent physically relevant pure states of the open quantum system. In the examples below the RDM can exhibit negative populations. This unphysical situation could probably be cured by applying an initial slippage to the initial state [33]. We note that these physically unreasonable RDMs occur because of unphysical initial states or because the QME is not physically correct or is applied in a parameter region where it is not valid. Nevertheless an unraveling scheme

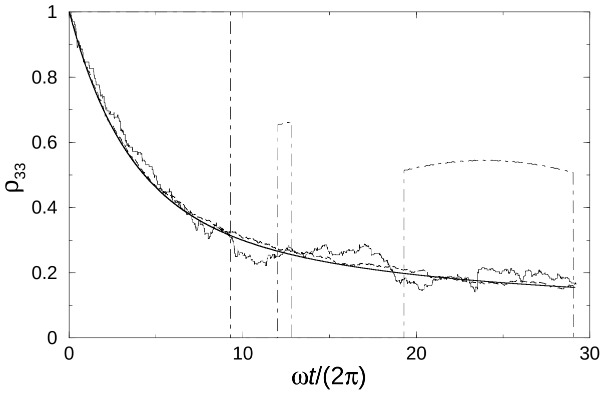

Figure 3.6: Time evolution of the third excited state of the harmonic oscillator in the quantum Brownian motion model for $\gamma = 10^{-3}\omega$, $kT = 4.5\omega$. The direct integration of the QME (thick solid line) is compared to the results of the quantum jump method with 1 trajectory (dot-dashed line), average of 100 (thin solid line) and 1000 (dotted line) trajectories.

has to be able to mimic also this unphysical behavior of the QME because in the ensemble average both should fully coincide.

The condition (3.33) applied to the QME (3.23) results in the additional constraint

$$A + A^\dagger = -\sum_{k=1}^{M}\left(E_k^\dagger C_k + C_k^\dagger E_k\right) \tag{3.34}$$

and if applied to the deterministic parts of the corresponding SSEs (3.31) and (3.32) it yields the total jump rate

$$p = -\frac{\langle\phi|A + A^\dagger|\psi\rangle + \langle\psi|A + A^\dagger|\phi\rangle}{\langle\phi|\psi\rangle + \langle\psi|\phi\rangle}. \tag{3.35}$$

All partial jump rates can be found subsequently making use of Eqs. (3.34) and (3.35):

$$p_k^1 = \frac{\langle\phi|C_k^\dagger E_k|\psi\rangle + \langle\psi|E_k^\dagger C_k|\phi\rangle}{\langle\phi|\psi\rangle + \langle\psi|\phi\rangle}, \tag{3.36}$$

$$p_k^2 = \frac{\langle\phi|E_k^\dagger C_k|\psi\rangle + \langle\psi|C_k^\dagger E_k|\phi\rangle}{\langle\phi|\psi\rangle + \langle\psi|\phi\rangle}. \tag{3.37}$$

The numerical algorithm of the new quantum jump method, which is slightly different from the standard one introduced in Subsec. 3.5.1, is summarized in Appendix B.

Let us briefly show how the proposed method can be applied to two typical physical problems: the quantum Brownian motion and dissipative electron transfer within Redfield theory. In both cases the systems are described by Markovian QMEs which do not have Lindblad structure. The model of Brownian motion [119] describes a particle with mass

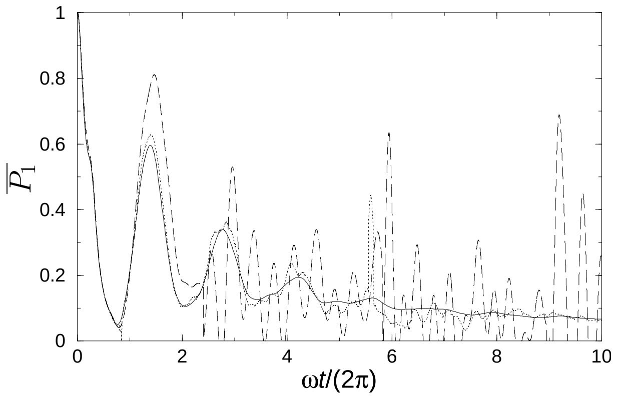

Figure 3.7: Relaxation of the donor population for the electron transfer model. The solid line shows the exact solution of the QME, the dashed line one arbitrary trajectory, the dotted line an average over 500 trajectories.

m, coordinate q, momentum p, and Hamiltonian H_S interacting with a thermal bath. In the high-temperature limit of a bath of harmonic oscillators the relevant QME has the form

$$\frac{d\rho}{dt} = -i\,[H_\mathrm{S}, \rho] - \frac{i\gamma}{2}\,[q, \{p, \rho\}] - m\gamma kT\,[q, [q, \rho]]\,, \tag{3.38}$$

where γ is the damping rate. Comparing with Eq. (3.23) one finds the operators of the jump algorithm ($M = 2$)

$$E_1 = \sqrt{\frac{\gamma}{2}}q,\ C_1 = -i\sqrt{\frac{\gamma}{2}}p, \tag{3.39}$$

$$E_2 = \sqrt{m\gamma kT}q,\ C_2 = E_2, \tag{3.40}$$

$$A = -iH_\mathrm{S} + \frac{i\gamma}{2}qp - m\gamma kTqq. \tag{3.41}$$

Modeling the particle as a harmonic oscillator with eigenfrequency ω one can compute the population dynamics depicted in Fig. 3.6. The initial state of the oscillator is the pure state $\rho_{33} = 1$. As can be seen, the agreement of the results using our stochastic method and a direct integration of the QME is already quite good for one thousand samples.

As a next test for the present quantum jump method we shall demonstrate the stochastic unraveling of the Redfield QME (2.9). Let us consider the model for electron transfer in which the system includes a single reaction coordinate with the Hamiltonian [52]

$$H_\mathrm{S} = H_1|1\rangle\langle 1| + H_2|2\rangle\langle 2| + v_{12}(|1\rangle\langle 2| + |2\rangle\langle 1|) \tag{3.42}$$

where H_1 and H_2 are the Hamiltonians of two coupled harmonic oscillators with equal frequency ω_0. We choose a potential configuration in the normal region with no barrier between the two harmonic potentials with strong electronic intercenter coupling. All

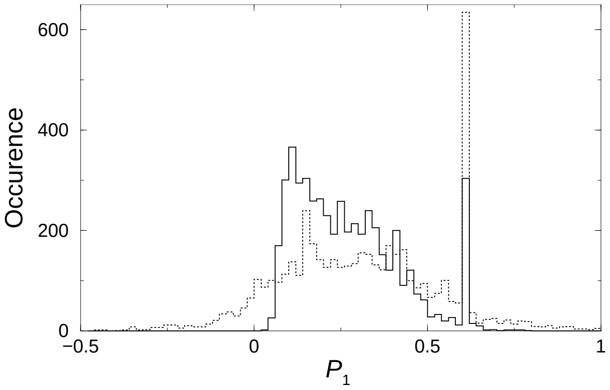

Figure 3.8: Occurrence of the expectation values of the population on the donor state produced by the new unraveling scheme for the Redfield QME (dotted line) and the standard normalized jump method for the Lindblad QME (solid line) at time $\omega t/(2\pi) = 3$, both with 5000 trajectories.

model parameters are the same as for case (a) in Sec. 2.6 (see Table 2.1 and Fig. 2.3). After rearrangement of Eq. (2.9) one can easily identify the operators involved in Eq. (3.23) ($M = 1$):

$$C_1 = K,\ E_1 = \Lambda,\ A = -iH_\mathrm{S} - K\Lambda. \tag{3.43}$$

A Gaussian wave packet located at the donor state $|1\rangle$, having energy slightly above the crossing of the harmonic potentials was chosen as initial state. The numerical simulation with about 1000 trajectories provides sufficiently converged and accurate results. Figure 3.7 shows the relaxation of the ensemble averaged donor population $\overline{P_1} = \overline{\langle\psi|1\rangle\langle 1|\phi\rangle} + \overline{\langle\phi|1\rangle\langle 1|\psi\rangle}$. A widely discussed property of the Redfield equation is that it does not strictly conserve positivity of the RDM [53]. Although $\overline{P_1}$ is always positive the tiny negative fraction in Fig. 3.8 is evidence for the existence of single realizations with negative P_1. In contrast, the simulation of the same system with the Lindblad QME, i.e. with DDA, by means of the standard quantum jump method [19, 29, 35, 30, 89] keeps all values of P_1 well confined between 0 and 1.

Besides the numerical efficiency, another benefit of the quantum trajectories is the better insight into the quantum mechanisms underlying the overall dynamics of the ensemble. Though it is impossible to give direct physical interpretation of every single trajectory one can extract information from the ensemble statistics. As we can see in Fig. 3.8 the distribution of the individual expectation values of the population is skew and comprises several modes. This is better seen in the phase space (Fig. 3.9). Several modes give rise to distinct pathways of the process as numbered in Fig. 3.9. The letter M stands for the main mode which disappears slowly with time to the advantage of three satellites denoted by S_1, S_2 and S_3. At certain time all modes coalesce to a single bell-like distribution which continues propagating in phase space while its maximum is approaching the equilibrium values $\langle p\rangle_{t\to\infty}$ and $\langle q\rangle_{t\to\infty}$. The variance of the final distribution indicates the presence of thermal fluctuations in the sample at finite temperature.

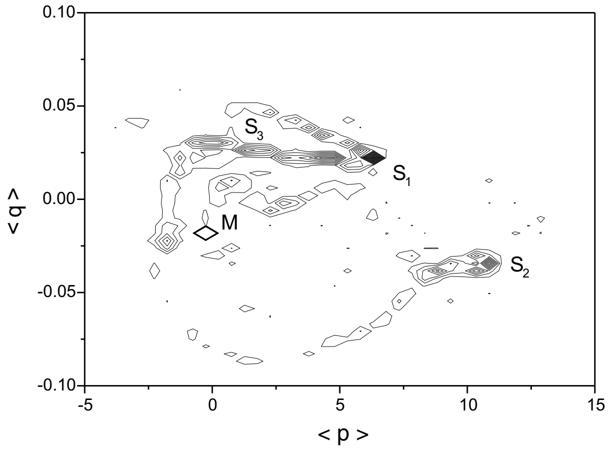

Figure 3.9: Contour plot of the correlated distribution of the expectation values of momentum $\langle p \rangle$ and position $\langle q \rangle$ for the electron transfer model at time $\omega t/(2\pi) = 3$ with 5000 trajectories.

Considering the efficiency of the stochastic method it is convenient to look at the relation between numerical effort and achieved accuracy. When the DDA is invoked together with RWA in the system-bath coupling one can obtain the Lindblad form (2.7) which can be solved by the standard quantum jump method [19, 29, 35, 30, 89] as well as by the new one. Thus, the numerical efficiency of both methods can be compared. The expectation values of most observables (like the population) are dispersed around the ensemble mean in a complicated distribution (Fig. 3.8). The standard deviation from the mean can be used as a measure for the statistical error, and hence for the accuracy. Figure 3.10 shows the accuracy of the new method applied to the Lindblad QME and to the Redfield QME and the accuracy of the standard quantum jump method applied to the Lindblad QME. Both methods are equally accurate for the Lindblad QME. However, solving the Redfield QME with the new method is less accurate with the same number of realizations. Thus, for well converged calculations one needs a much larger number of trajectories. Furthermore, each time step in the implementation of the new method requires $4M+9$ matrix-vector multiplications versus only 5 for the standard jump algorithm which means a significantly higher computational effort.

3.6 Summary

In this Chapter an estimation of the numerical efficiency of several methods for density matrix propagation has been given. The example of ET in a two-center system has been used for this purpose. A specific measure of the numerical effort has been introduced in order to compare methods with fixed time step and such ones with time step control (RK). Besides the method of reference (NP) the RK-NAG approach shows best performance for both cases of ER and DR. The advantage of the SIA propagator is that the accuracy improves with decreasing the time step in both representations and provides a reasonable

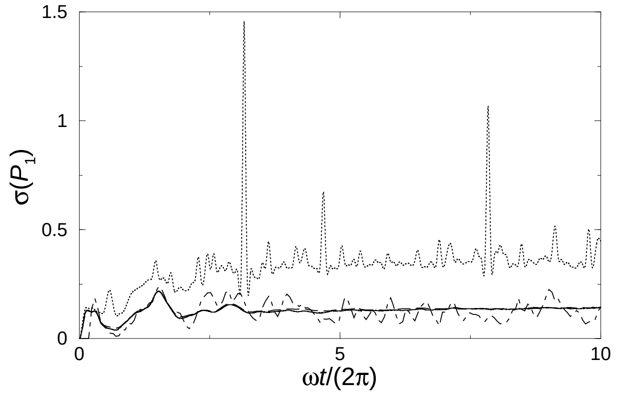

Figure 3.10: Standard deviation from the ensemble mean value of the population of the upper diabatic PES for 5000 trajectories. Dotted line and dashed line designate the accuracy of the new method applied to the Redfield QME and to the Lindblad QME respectively, and the solid line the standard quantum jump method for the Lindblad QME.

ratio between accuracy and numerical effort. That is not the case with the CP propagator which exhibits a saturation of accuracy and is therefore not convenient for very small time steps. The easy-to-implement SI gives reasonable performance for not too high accuracy. The present SI seems to be limited in accuracy due to the fixed coefficients.

The stochastic unraveling of QMEs is not constrained to Lindblad form anymore and opens new large fields of application for stochastic methods. This progress became possible with the use of the wave–function pair in the doubled Hilbert space and the derivation of stable, almost normalized SSEs. An efficient first-order quantum jump algorithm was proposed. The efficiency is determined by the behavior of the norm of every single trajectory. In this sense the jump rates were used as parameters to influence the efficiency.

Occurrence of negative population for single trajectories is by no means a problem of the proposed unraveling scheme. Rather it is related to the fact that the QMEs (3.23, 2.9) do not preserve the RDM positive semidefinite. It is known [33] that the negative eigenvalues of the RDM in the Redfield theory arise from the inconsistency between the initial RDM and the bath state, i.e. due to neglected initial correlations in the Born-Markov approximation. Satisfactory resolution of this problem is the slippage of the initial conditions as derived by Gaspard *et al.* [33]. In this method the so called slippage superoperator takes into account the short-time bath correlations. Applied to the initial RDM it introduces the necessary correlations into the initial state. This manipulation of the initial state ensures propagation of positive semidefinite RDM at any further moment of time.

The new stochastic method was successfully tested for a simple ET model using the Redfield QME and for quantum Brownian motion and should allow for better quantum dynamical simulation of large systems. It is also capable to unravel non-Markovian QMEs when they are in a time-local form like in the time-convolutionless formalism [12] or in methods using auxiliary density matrices to include the memory effects [80].

Chapter 4

Intramolecular electron transfer in betaine-30

4.1 Experimental and theoretical background

Betaine-30, also known as Reichardt's dye [99], is an organic compound whose color strongly varies with the polarity of the solvent in which it is dissolved. Thus, its long wavelength absorption band, assigned to the $S_0 \rightarrow S_1$ transition, is shifted over 10 000 cm^{-1} on going from non-polar (e.g. ethers) to polar solvents (e.g. water). This property is called solvatochromism. The transition $S_1 \rightarrow S_0$ represents back ET as an electron moves from the pyridinium ring, the donor, back into the phenoxide moiety, the acceptor (Fig. 4.1). No fluorescence has been observed which means that this transition proceeds via radiationless mechanisms, i.e. fast internal conversion. Not only the position of the band is solvent dependent but also its width and shape. This means that the solvent environment influences both the free energy gap ΔG and the Franck-Condon gap $|\Delta G| + \lambda$ between the PESs of S_0 and S_1. Polar solvents have stronger dipole-dipole interaction with the large dipole of the ground state, shift the ground state energy down and hence make the back-ET reaction more exothermic.

The full absorption band comprises a number of broadened single peaks arising from internal molecular vibrations and solvent motion. Such internal and external modes which undergo reorganization give rise to the effective reaction coordinate. Analyzing the band shape in various solvents all single-coordinate parameters were determined [51]. Furthermore, it was found [51] that the potential configurations were in the Marcus inverted region. Another peculiarity, which makes the theoretical treatment of betaine-30 more difficult, is the large intercenter coupling. Its value is comparable with the energy of the fastest molecular mode. It was shown [117] that in this case the classical theory of Marcus [72] failed to give meaningful rates. Nevertheless, Marcus theory was verified in the inverted region for systems with small electronic coupling [17]. Transient spectroscopies [2, 1, 117, 61] showed that reorganization of low frequency internal modes and solvation take place on the same very short timescale as the back ET itself. The ET rates in a variety of solvents as well as the reorganization energies arising from internal and solvent modes were determined with the help of transient spectra. Beard *et al.* [6]

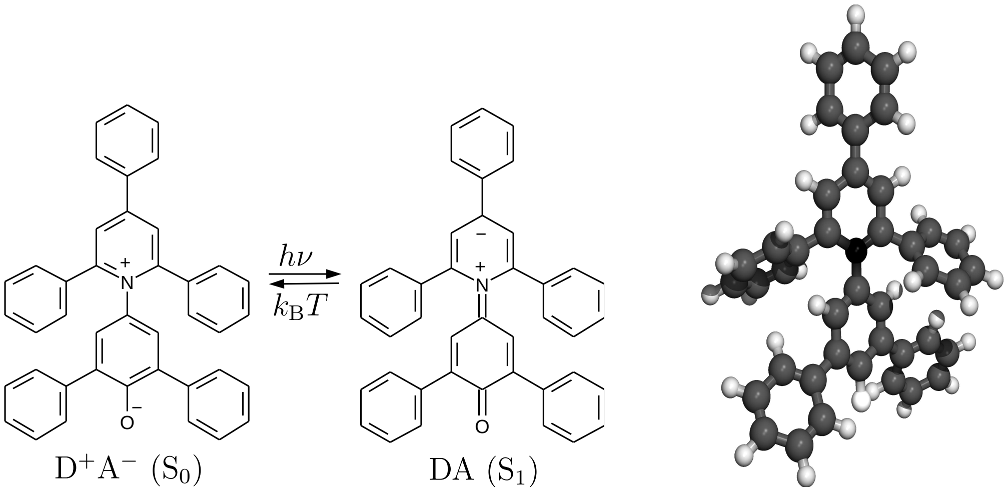

Figure 4.1: Left plot: schematic representation of the photoinduced ET transition from the excited DA state to the ground D^+A^- state in betaine-30. Right plot: relaxed three-dimensional structure of betaine-30 in ground state.

measured directly the intramolecular ET in betaine-30 in chloroform by means of the emitted electromagnetic wave after pulse laser excitation in strong electric field. They succeeded to extract two characteristic times, 300 fs and 1.5 ps. Concurrently, Hogiu *et al.* [42] observed the population in S_1 mode-selectively by picosecond time-resolved anti-Stokes Raman spectroscopy and showed that the rise times of the vibronic populations of several relevant modes correspond to the back-ET time. Other researchers employed resonant Raman spectroscopy [126, 125] and found a set of Raman-active internal modes coupled to the electron transition. However, their estimated internal reorganization energy (170 cm^{-1} with 9 internal modes and 120 cm^{-1} with 19 internal modes, respectively) is in disagreement with band-shape analysis (2499 cm^{-1}) [117] as well as with pump-probe spectroscopy (3370 cm^{-1}) [61]. On the other hand, the estimate for the solvent reorganization energy λ_s for acetonitrile in Refs. [126, 125], (6000 cm^{-1} and 4500 cm^{-1}, respectively) is much larger than the respective value in Ref. [117] (2221 cm^{-1}) or than theoretical calculations [68, 81] (3625 and 4260 cm^{-1}, respectively). As far as these parameters enter the quantum model for ET which is used in the current work it is very important to set their values carefully. Despite these discrepancies all authors have agreed that at least three modes play significant roles – a high frequency quantal internal mode, a low frequency classical internal mode and a solvent mode. Kovalenko *et al.* [61] estimated the characteristic time of the early stage involving solvation of S_1 and reorganization of the low-frequency mode to about 100 fs in acetonitrile. Another experimental finding, which also would concern the choice of a model, is the transient long-wavelength *dark state* absorption observed in different media [61]. The nature of the dark state is not clear yet. The authors of Ref. [61] suppose that the dark state is the conformationally relaxed excited state. Such a hypothesis is not supported by the low energy of the dark state absorption. In fact, the Franck-Condon gap between S_1 and the next optically accessible state S_2 is 19600 cm^{-1} and significantly larger than the maximum of the dark state absorption band, 12380 cm^{-1}. This ratio is very weakly solvent dependent. This is why the dark state might be more reasonably assigned to a non-relaxed configuration of the ground electronic state S_0. Since the decay time of the dark state absorption is quite long (1.2 ps in acetonitrile) the relaxation could be due to a slow low-frequency molecular mode. The theoretical confirmation of the latter hypothesis as well as the re-examination of the proposed two stage mechanism [61] are some of the goals of the present work.

The existing theoretical approaches to ET in betaine-30 can be divided into three types: i) the classical and semi-classical rate theories of Sumi-Marcus and Jortner-Bixon applied to betaine-30 [2, 1, 117], ii) quantum chemistry and molecular dynamics methods [44, 67, 68, 81], and iii) the RDM theory with use of a single reaction coordinate [27, 103]. All methods in the first group use system models comprising only two diabatic states (DA and D^+A^-). However, there are models involving a third mediator (bridge) state [8]. In the present investigation only a two-state model will be used. The RDM method allows for fully quantum-mechanical simulation of the short time ET dynamics, i.e. the spectroscopic signals can be calculated with sufficient time resolution in a straightforward manner.

In the present work the previous studies, which involve one-mode models and base mainly on the analysis of the population dynamics, are extended. A two-mode model is developed and solved accurately with use of RDM theory. In Sec. 4.2 the rates of ET in two media (acetonitrile and acetone) will be calculated using the two-mode model and compared with existing experimental data. Then the pump-probe spectra are computed with the two-mode model, compared with existing experimental spectra and discussed (Sec. 4.3). For these simulations two different parameter sets will be used. In the first parameter set, used in Sec. 4.2, a high-frequency internal mode and a solvent mode are considered basing on estimates by Walker *et al.* [117]. The rates, with which the present results will are compared, are taken from the same reference. In the second set, taken from Ref. [61] and used in Sec. 4.3, a low-frequency internal mode and a high-frequency internal mode are considered. Nevertheless, the parameters for the high-frequency internal mode differ in these two references. Two different parameter sets are prefered in the present work since the results have to be compared with two different experiments.

4.2 Population dynamics and electron transfer rates

As discussed in Sec. 2.4 the application of Redfield theory is more reasonable and accurate if multiple modes are included in the relevant system. On the other hand, recent pump-probe [61] and transient Raman [42] spectroscopies revealed the multi-mode nature of the back-ET transition. Staying in the limits of the Redfield theory it is not possible to test directly the accuracy change with employment of multi-mode models. Comparing the ET rates it is at least possible possible to verify the physical relevance of such an extension and this is the subject of this Section.

There is certain freedom in the construction of a two-mode model if deduced from the one-mode model. This is due to the fact that one can set arbitrarily large number of

Table 4.1: Parameters for the ET models of betaine-30 in two solvents. All values are given in cm^{-1} unless otherwise specified.

	ω_1	ω_2	ω_{eff}	λ_1	λ_2	λ_{eff}	$-\Delta G$	V	Γ	T, K
acetonitrile	2900	1600	1800	2014	1264	3145	11645	2500	10	298
acetone	1700	1600	1633	1813	1178	3096	10954	2500	9	298

Table 4.2: Rates of ET in betaine-30 in acetonitrile and in acetone.

	k_{ET}, ps^{-1}	
method	acetonitrile	acetone
DDA1	0.034	0.061
ER1	0.19	0.13
ER2	0.32	0.26
Sumi & Marcus [117]	10^{-4}	2×10^{-5}
Jortner & Bixon [117]	0.28	0.22
Walker *et al.* [117]	1.8	1.2
Experiment [117]	0.50 (2.0)	0.43 (1.4)

combinations of mode frequencies which satisfy the relation between the effective mode and modes in the two-mode model [122,115]. This is why we assign the reorganization energies of the solvent mode and of the internal mode, as well as the effective reorganization energies, approximately the same values as given in Ref. [117] (see Table 4.1). However, the reduction of a multi-mode model to the one-mode model is unique.

Using the parameters for betaine-30 listed in Table 4.1 all matrices that enter the Redfield equation (2.9) were constructed according to their multi-mode definitions as described in Sec. 2.4. Then Eq. (2.9) was solved numerically by means of direct propagation of the RDM. The population of the DA state was calculated applying the projection operator of this state to the RDM: $P_1(t) = \mathrm{Tr}(\rho(t)|1\rangle\langle 1|)$. Extracting the slowest decay exponent the ET rate k_{ET} was found. In Figs. 4.2 and 4.3 the population decay in the initially populated upper electronic surface is shown as a function of time for betaine-30 in acetonitrile and acetone, respectively. Three different versions of the RDM calculation are shown. First, the population is calculated with the DDA, introduced in Chapter 2, in a model with one effective mode (DDA1). This is compared to the results in the one-mode model with exact treatment of the intercenter coupling in ER (ER1). As can be seen in Table 4.2 the rate differs quite a bit from the earlier investigations [52] as was expected. In the two-mode model (ER2) the transfer rate becomes even larger and comparable to the rate calculated in the theory of Jortner and Bixon [48,117]. The rate calculated in Sumi-Marcus theory [113,117] is off about four orders of magnitude. This must be expected in the inverted region for systems with large electronic coupling $v_{12} \gg \omega_0$ where quantum effects prevail. The integral pump-probe signals were fitted by Walker *et al.* [117] to a

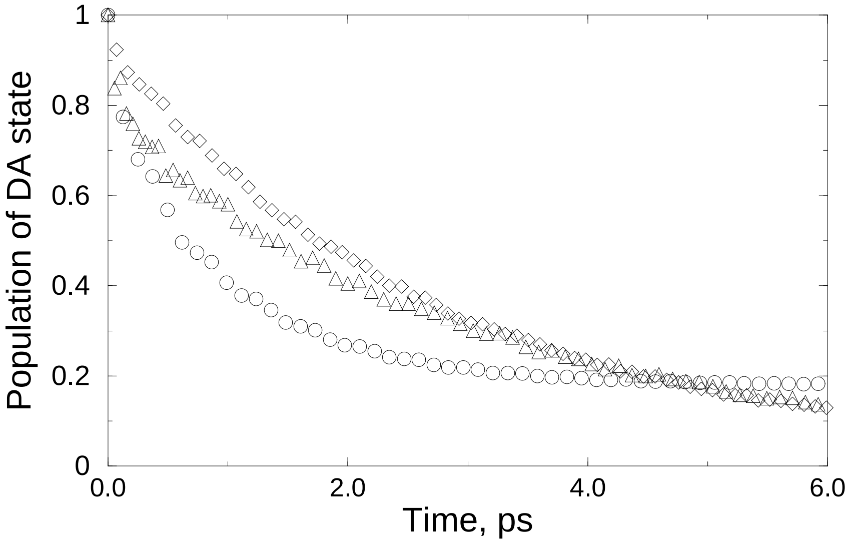

Figure 4.2: Population decay of the DA state of betaine-30 in acetonitrile for the one-mode model with diabatic damping approximation (DR0, circles), for the one-mode model with exact Λ (ER, triangles), and for the two-mode model with exact Λ (ER, rhombs).

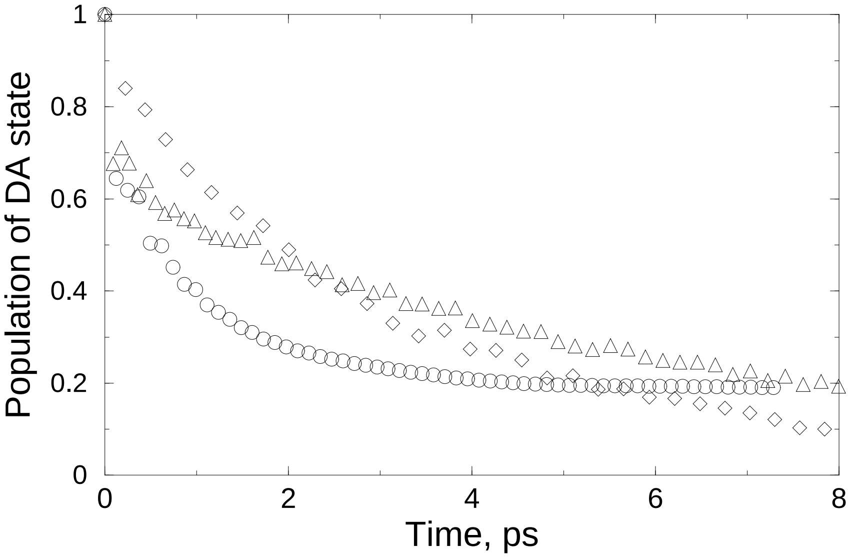

Figure 4.3: Population decay of the DA state of betaine-30 in acetone. See Fig. 4.2 for explanation of the symbols.

bi-exponential form. Though in that reference the faster component was declared to be the rate (given in parentheses in Table 4.2) it is compared here to the slower long-time exponent because the back-ET rate is determined by the slowest decaying process. It should be noted that the uncertainty in the experimental determination of k_{ET} is about 15 % [117].

4.3 Pump-probe spectroscopy

The recently developed techniques for ultrashort (femtosecond) pulse generation enabled the direct observation of molecular dynamics on the timescale of nuclear motion. Therefore, the physical processes as intramolecular vibrational energy redistribution, vibrational decoherence and relaxation can be detected in real time. As introduced, the transient absorption spectra have revealed many details about the mechanisms involved in the ET dynamics in betaine-30. In such an experiment (sketched in Fig. 4.4) a short laser pulse (pump pulse, $E_1(t)$) is shot through the sample. If the carrier frequency of the pulse is close to resonance with the $S_0 \rightarrow S_1$ transition energy the probe will absorb light and a wave packet (coherent superposition of vibronic states) will be created on S_1. With a second pulse (probe pulse, $E_2(t)$) the current state of the system is probed after a certain time delay $T_2 - T_1$. The non-linear transient emission-absorption signal contains the response of the system in direction $\mathbf{k}_2$ in which the probe pulse is propagating. It can be either decomposed by a polychromator [69, 60, 61], which results in frequency resolved spectrum, or immediately integrated [2, 1, 117].

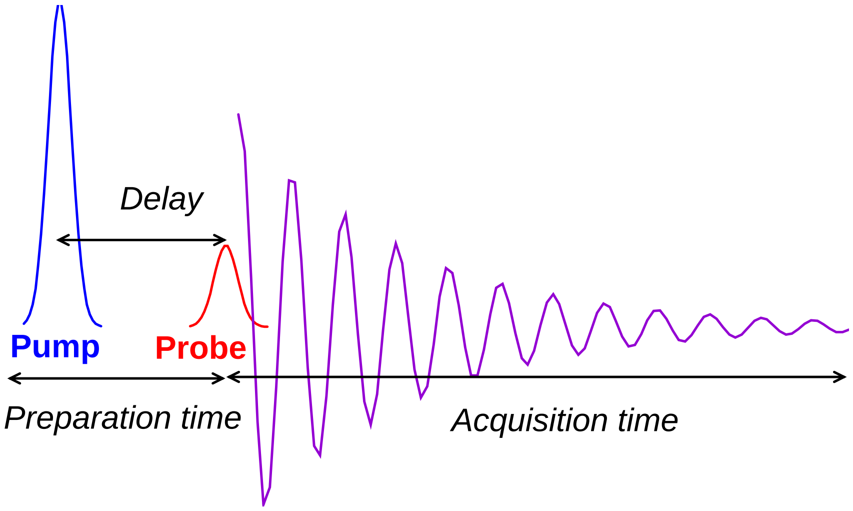

Figure 4.4: Sketch of a pump-probe pulse sequence abstracted from the details of the actual experimental setup [69].

4.3.1 Description of the method

First, one needs to model the field-matter interaction. The field applied can be generally written as

$$\mathbf{E}(\mathbf{r},t) = \sum_{j=1}^{2} \mathbf{e}_j \left[E_j(\mathbf{r},t) + E_j^*(\mathbf{r},t)\right] = \sum_{j=1}^{2} \left[\mathbf{e}_j \mathcal{E}_j e^{i\Omega_j t - i\mathbf{k}_j\cdot\mathbf{r}} + \text{c.c.}\right] \tag{4.1}$$

where $\mathbf{e}_j$ is the polarization vector, $\mathbf{k}_j$ the wave vector, Ω_j the carrier frequency, and $\mathcal{E}_j$ the pulse envelope of pulse j. In what follows, the vector notation will be omitted because the sample is assumed to be homogeneous, isotropic and optically thin. Using $E_j(\mathbf{r},t)$ the Hamiltonian of the system-field interaction can be expressed in dipole approximation, provided that the field is not very strong,

$$H_{\text{SF}}(t) = -\left[|0\rangle\mu_{01}\langle 1| + |1\rangle\mu_{10}\langle 0|\right] \mathrm{E}(\mathbf{r},t) \tag{4.2}$$

where μ_{01} is the dipole operator of the transition $\mathrm{S}_0 \rightarrow \mathrm{S}_1$. In this model the external field becomes a part of the relevant system as $H_{\text{SF}}(t)$ has to be incorporated into H_{S}. As previously discussed in Redfield theory one has to use the representation, in which H_{S} is diagonal. Here, this will not be done because one can assume that H_{SF} is a perturbation in H_{S} with lower order contributions than the other off-diagonal parts of H_{S} such as the intercenter coupling V.

A simulation of a pump-probe experiment can be conveniently done with the help of the RDM ρ_{S}. The total polarization $\mathrm{P}(\mathbf{r},t)$, which measures the response of the system in all directions and contains contributions of higher order with respect to the external field, can be calculated in terms of the quantum mechanical mean

$$\mathrm{P}(t) = \operatorname{tr}\left\{\rho(t)\left[|0\rangle\mu_{01}\langle 1| + |1\rangle\mu_{10}\langle 0|\right]\right\}. \tag{4.3}$$

Under the experimental conditions the detected signal in $\mathbf{k}_2$ direction is proportional only to a distinct component $P_{k_2}^{(3)}(t)$ of the total polarization P. This is why one has to separate all contributions in the calculated P. Besides perturbative approaches for calculation of various orders and directions of the polarization [92,60,107,83] an alternative technique was developed [106,21] and later used for calculation of pump-probe spectra of ET-systems [124,123] and photon echoes [82]. In the non-perturbative approach the total polarization $\mathrm{P}(\mathbf{r},t)$ is decomposed into Fourier series

$$\mathrm{P}(\mathbf{r},t) = P(\mathbf{r},t) + P^*(\mathbf{r},t) = \sum_{m,n} \left[P_{m,n}(t) e^{i(m\mathbf{k}_1 + n\mathbf{k}_2)\cdot\mathbf{r}} + \text{c.c.}\right]. \tag{4.4}$$

In order to obtain the pure third order from $P(t)$ one has to extract the linear terms first. This is done by calculating $P(t)$ without pump pulse, then without probe pulse and then subtracting these from $P(t)$ with both pump and probe pulse, i.e. $\widetilde{P} = P_{(\text{pump on})} - P_{(\text{pump only})} - P_{(\text{probe only})}$. The infinite number of directions is restricted under certain assumptions, discussed in more detail in Refs. [106,82]. Here is only a short overview

Table 4.3: Parameters for the two-mode model used for simulation of the pump-probe-spectra of betaine-30 in acetonitrile (units cm^{-1}).

mode, m	frequency, ω_m	reorg. energy, λ_m
1	1350	1430
2	209	1940
effective	1152	1216

1. The symmetry of a two-state system leads to the condition $m+n = \pm 1, \pm 2, \pm 3$, etc.
2. The weak field limit constrains the order of the decomposition (4.4) to 3, i.e. $|m| + |n| = 1, 3$.
3. Finally, the condition for resonance excitation imposes the additional relation $m + n = 1$.

Applying these restrictions to Eq. (4.4) one is able to identify that the remaining directions are $\mathbf{k}_1$, $\mathbf{k}_2$, $2\mathbf{k}_1 - \mathbf{k}_2$, and $2\mathbf{k}_2 - \mathbf{k}_1$. Calculating $\widetilde{P}$ for four values of the phase difference $\varphi_1 - \varphi_2 = \mathbf{k}_1 \cdot \mathbf{r} - \mathbf{k}_2 \cdot \mathbf{r}$ and solving a system of four linear equations one is able to determine the desired component [106]

$$P_{k_2}^{(3)}(t) = \frac{1}{2}\text{Re}\Big\{\widetilde{P}(\varphi_1 = 0) + \widetilde{P}(\varphi_1 = \pi/2) + \widetilde{P}(\varphi_1 = \pi) + \widetilde{P}(\varphi_1 = 3\pi/2)\Big\} \tag{4.5}$$

where $\varphi_2 = 0$ in all cases for simplicity. For this purpose the QME (2.9) must be solved numerically once for each value of φ_1 with and without probe. The total number of RDM propagation runs is nine including the run with probe pulse only. After the Fourier transforms $P_{k_2}^{(3)}(t, \Delta t) \rightarrow P_{k_2}^{(3)}(\omega, \Delta t)$ and $E_2(t, \Delta t) \rightarrow E_2(\omega, \Delta t)$, the normalized differential signal can be eventually calculated as [107, 92, 60]

$$\Delta D(\omega, \Delta t) = -\frac{2\omega \text{Im}\left[E_2^*(\omega, \Delta t) P_{k_2}^{(3)}(\omega, \Delta t)\right]}{|E_2(\omega, \Delta t)|^2} \ . \tag{4.6}$$

4.3.2 Results

The first problem, concerning the two-mode model for betaine-30, that has to be solved is the selection of two ET-relevant modes. In a recent transient Raman study [42] it was found that three high frequency modes (1603, 1360 and 1245 cm^{-1}) mainly take part in the vibrational energy redistribution during the back-ET transition. They were assigned to collective stretching motions of that pyridinium ring which has three phenyl rings in its vicinity. In addition, the authors suggested that the low frequency mode at 133 cm^{-1} (torsional motion between the pyridinium and phenoxide planes) plays a significant role as well. The signature of a fast relaxing high frequency mode (1350 cm^{-1}) was uncovered also by Kovalenko *et al.* [61] as an initial detuning of the stimulated emission

Table 4.4: Parameters for the pulses used for simulation of the pump-probe spectra.

pulse	carrier frequency Ω_j, nm	fwhm τ_j, fs	rel. energy, A_j	delay T_j, fs
E_1 (pump)	637	30	1	0
E_2 (probe)	637	5	0.25	300

peak from the excitation wavelength. Thus, the choice of representative modes as well as reorganization energies, shown in Table 4.3, was facilitated by the latter work. In the room-temperature regime the low-frequency mode can be treated classically. In fact, some authors [117, 67] used two different types of hybrid quantum-classical models and called the mode and the corresponding reorganization energy classical. This is why its spectroscopic value (133 cm^{-1}) is replaced here by $k_\mathrm{B}T$ which is 209 cm^{-1} at 300 K. The electronic coupling between the diabatic states v_{12} was taken 2800 cm^{-1} [117] and the free energy gap ΔG 10940 cm^{-1} [61]. The cutoff frequency of the bath spectral density is inversely proportional to the bath correlation time τ_c identified here with the relaxation time of acetonitrile which is $\tau_s = 0.5$ ps for room temperature [117]. Just one parameter, namely the system-bath coupling strength, remained free. An important point to note is that the corresponding effective single-mode model with the parameters in Table 4.3 yields population dynamics many times slower than the dynamics of the two-mode model. This is why considering a reduced one-mode model is meaningless and hence not performed here.

In order to achieve frequency resolution over a large spectral region an elaborate supercontinuum probing technique was used in the experiment [60, 61]. It was shown that the supercontinuum is equivalent to a chirped probe pulse [60]. For the sake of simplicity, the present simulation is restricted to non-chirped pulses. Considering a Gaussian pulse shape, characterized by its relative amplitude A_j and full width at half maximum (fwhm) τ_j

$$\mathcal{E}_j(t) = \frac{A_j}{\sigma_j\sqrt{2\pi}} \exp\left[-\frac{1}{2}\frac{(t-T_j)^2}{\sigma_j^2}\right] \quad \text{where} \quad \sigma_j = \tau_j/\sqrt{8\ln 2}\ , \tag{4.7}$$

the width of the probe pulse τ_2 has to be at least 10 fs to cover the spectral region between 500 and 900 nm for the laser wavelength of 637 nm. The optimal value has been found to be even shorter, $\tau_2 = 5$ fs in order to obtain a neat normalization in Eq. (4.6). All parameters of the external field are collected in Table 4.4.

It turned out that the calculation of a single pump-probe spectrum of betaine-30 using the model parameters in Table 4.3 is already an extremely demanding computational task. In particular, for the low frequency mode one needs a large number of basis functions (about 30 diabatic levels). On the other hand, to get high-quality Fourier transforms the acquisition time, respectively the propagation time, has to be very long. The larger the pump-probe delay the longer is the acquisition time required. Thus, the method for density matrix propagation is CPU-time-critical. This is why the simulation had to be done with resort to DDA and RWA in order to propagate the RDM by means of stochastic wave functions with use of the standard quantum jump method (see Sec. 3.5.1

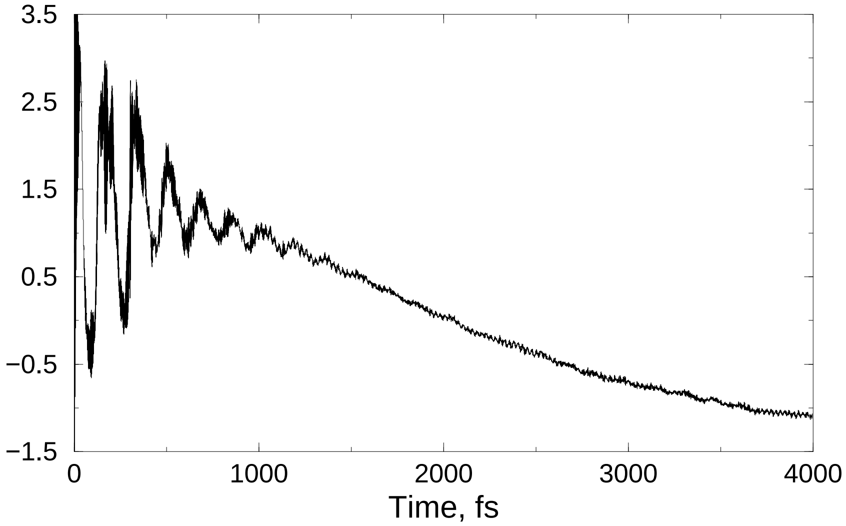

Figure 4.5: Decay of the total polarization. The system is probed 300 fs after the pump pulse.

and Appendix B) although the electronic coupling is very strong. The stochastic algorithm was parallelized with use of *Message Passing Interface* (MPI) [26] and the computations were carried out on a PC cluster with 48 nodes. The propagation time was limited to 4 ps. One thousand trajectories gave reasonable convergence.

Figure 4.5 shows the total polarization calculated with pump pulse centered at $t = 0$ and probe pulse at 300 fs. Coherent motion is prominent in the early evolution and is not seen after 1.5 ps. The revival periods exactly match the period of the low frequency mode at 209 cm^{-1}. The polarization decays with characteristic time of about 4 ps. One can hardly establish unique relations between these times and the times determined by Kovalenko *et al.* [61], 100 fs (solvation and low frequency mode reorganization) and 1.2 ps (back ET) respectively. However, the characteristic time of 4 ps is consistent with the ET-rate already calculated in Sec. 4.2. Again, the use of DDA in the case of strong electronic coupling can give rise to wrong rates. Apart from this slight differences, this result is in good qualitative agreement with the previously determined back-ET rate [117] and also with the concept of a two-stage mechanism [61]. In Chapter 2 it was noted that in the inverted region for strong electronic coupling the back-ET rate is determined by the damping rates. One can use the freedom of the present dissipation model and fit the damping rates so that the ET rate matches the experimental value. A better idea is either to develop a self-consistent model for the dissipation or to use a spectral density from molecular dynamics (MD) simulations.

To compare the simulated frequency-resolved transient emission/absorption spectrum with experiment one has to note that many details of the real system are not included in the model. In particular, the second excited state S$_2$ of betaine-30 is not taken into account in the model and hence the excited-state absorption detected in the blue region [61] is not supposed to show up in the simulation results. The experimental and the simulated

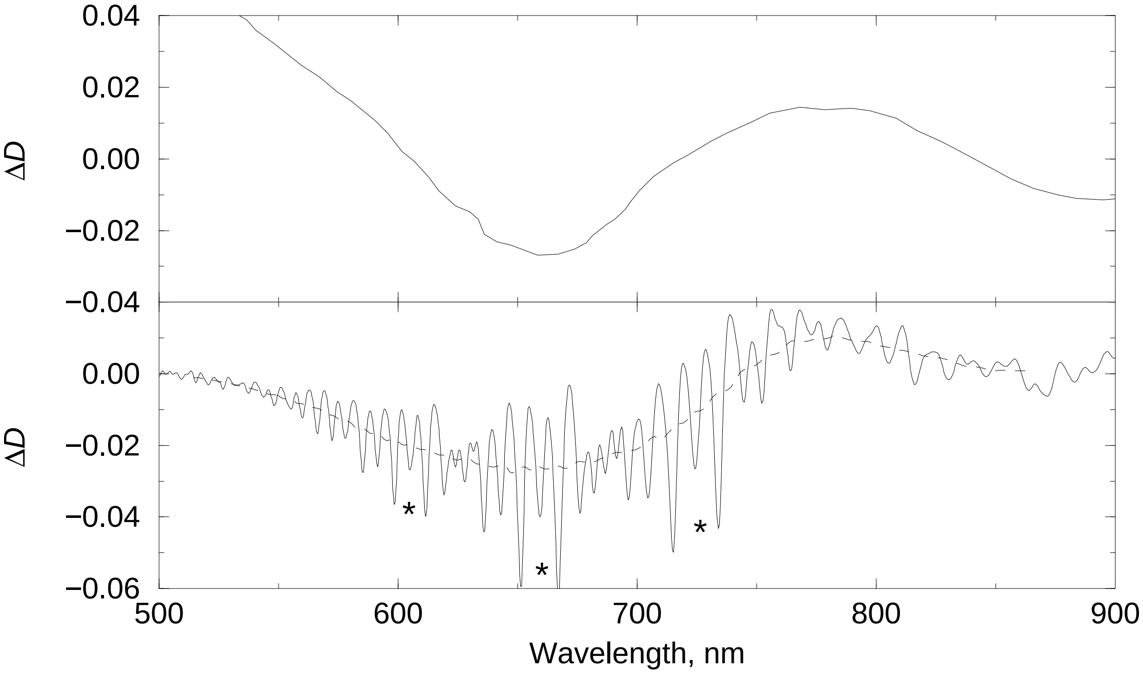

Figure 4.6: Comparison between the experimental (upper graph) and the simulated (lower graph) disperse spectrum in acetonitrile. The dashed curve is a running average of the simulated signal with length of one oscillation period. The experimental data were taken from Ref. [61].

frequency-resolved spectra are shown in Fig. 4.6. The sign convention in Eq. (4.6) is such that negative signal means emission, positive – absorption. The absolute intensity of the simulated spectrum is arbitrary in this simulation, so it was scaled into the range of the experimental one. The overall oscillatory structure of the simulated spectrum has apparently no physical meaning. This is very likely due to the insufficient acquisition time. Single tests with longer acquisition times gave weaker oscillations. The three doublets, marked with asterisks, may indicate the high frequency mode at 1350 cm^{-1}. If this is the correct interpretation of these patterns then the high frequency mode should not have relaxed 300 fs after the pump pulse. This is again a problem arising from the insufficient model for the spectral density. The splitting constant of the doublets, which is about 360 cm^{-1}, cannot be attributed to the low frequency mode at 209 cm^{-1}. Averaging the simulated spectrum with length of one oscillation period yields a representation which can be easily compared with the experimental spectrum. Both maxima of the stimulated emission and of the non-linear absorption at 660 and 780 nm respectively are in good quantitative agreement with the experiment. The transient non-linear absorption is very weak due to low occupation of the higher vibrational levels in the ground electronic state S_0. As already mentioned the absorption band between 500 and 600 nm should not appear in the simulation and in fact it does not.

A very essential point in the interpretation of the simulation results concerns the concept of a two-stage mechanism proposed in Ref. [61] in which one can distinguish between internal ET and back ET. Probing at delay of 300 fs after pump excitation should reveal the crossover between these two stages. The ultrafast vibrational relaxation of high-frequency modes within 10 fs is not resolved and not included as a particular stage. Therefore the faster stage of the proposed mechanism with characteristic time of about 100 fs [61] corresponds to the decay of coherent motion in the simulation as discussed above. Then the slower back ET to S_0 occurs by radiationless internal conversion with time 1.2 ps. This is the period of increase of the dark state absorption at 780 nm in the experimental spectra. In the present model absorption is possible only from the ground state S_0. Since the dark state absorption in the simulated spectrum is present at the same time and wavelength as in experiment the decay of the dark state should rather be related to the backward rearrangement in S_0. Summing up, the simulation results are conform with the scenario from Ref. [61] except for the interpretation of the dark state.

4.4 Summary

This numerical study was inspired by the recent advance in the femtosecond spectroscopy of betaine-30 and further motivated by the need of a better understanding of the photophysics of ET in this dye. By simple modeling of the system with one or two reaction modes and accurate quantum-mechanical treatment with use of the Redfield theory it was possible to approach the complicated physics of this system. The population dynamics was calculated using both the one-mode model and the two-mode model for two solvents, acetonitrile and acetone. The rate of ET was extracted from the slowest exponent in the population dynamics of the excited state and then compared with the rates from other theories and with the experimental rates. The rate predicted by the two-mode model is in better agreement with the experimental rate than the rate resulting from the one-mode model.

The simulation of the frequency-resolved transient spectra using the two reaction modes showed that the proposed modeling of the problem is capable to cover the essential mechanisms uncovered in recent experiments. In contrast, the minimal model involving one reaction mode fails for certain parameter sets. Both nonlinear absorption and stimulated emission maxima in the simulation are in very good quantitative agreement with experiment.

The question to which extent the use of DDA has influenced the results of the simulation ought to be posed in the conclusion. It cannot be answered uniquely until full, and hence very expensive, simulations are done without the use of DDA. The profound analysis of the behavior of this approximation in Chapter 2 has shown that in the configurations without barrier as well as in the inverted region the population dynamics is influenced only in the long-time limit even in the case of strong electronic coupling. Thus, it is rather expected that the future reference calculations with no resort to DDA will introduce qualitatively nothing new but certainly will improve the overall physical consistency of the results.

Future studies on this subject should follow a more precise modeling of the system-bath interaction, possibly in a self-consistent manner. For instance, the model can be coupled to MD simulations which provide more detailed and system-specific information about the spectral density of the bath.

Chapter 5

Photoinduced electron injection

5.1 Introduction

In recent years ET between molecular adsorbates and semiconductor nanomaterials and surfaces has been subject of much research [3]. The injection of an electron into the conduction band is a prototype reaction for a lot of electrochemical and photo-electrochemical interfacial processes such as photography, solar energy conversion, quantum dot devices, etc. [3]. Interfacial ET between discrete molecular levels and a conducting surface is the simplest of all surface reactions: it involves only the exchange of an electron, and so no bonds are broken.

The ultrafast nature of the charge injection from various adsorbed molecules to the conduction band of the semiconductor was shown in recent experiments [13, 16, 40]. The theoretical description of such experiments requires an adequate treatment of the ET dynamics and consideration of ultrashort time-scale phenomena such as coherences. This can be done using the RDM approach.

In previous studies Ramakrishna *et al.* [96] described the electron injection from a surface-attached chromophore to the conduction band of a semiconductor using the time-dependent Schrödinger equation, thus neglecting dissipation processes. With use of the same model pump-probe signals were calculated by means of the third-order polarization [95]. In a more recent work [97] the influence of the PES configuration of the donor on the decay of the donor population as well as the effect of varying the density of states of the quasicontinuum were investigated in detail. It was shown that the recurrence time, for which the electronic population of the donor state is recovered, is inversely proportional to the energy spacing between the electronic PES in the quasicontinuum. In the limiting case of an ideal continuum no recurrences can occur only after infinite period of time. This implies that the population of the donor state can decay irreversibly into the continuum without dissipative mechanisms. In addition the experimental studies on the system perylene-TiO_2 seem to support such an idea [13, 40]. Performing pump-probe spectroscopy with perylene-TiO_2 a vibrational wave packet, composed of the perylene normal modes, is initially prepared. Before substantial vibrational relaxation and dephasing have taken place the electron is injected into the TiO_2 conductance band within 150 fs after the pump pulse. Furthermore, the decay time shows no temperature dependence.

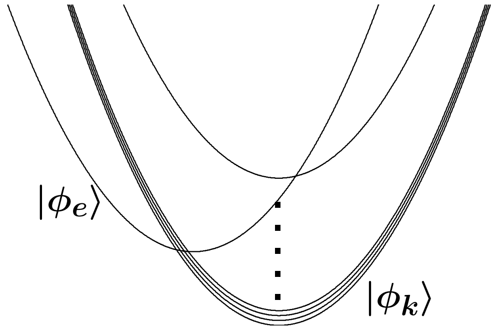

Figure 5.1: Scheme of the model PES for the excited state of the chromophore $|\phi_e\rangle$ and for the quasicontinuum states $|\phi_k\rangle$. Only four of all 31 quasicontinuum states are shown.

However, all these facts do not exclude the possibility that other dissipative mechanisms (not just vibrational relaxation and dephasing) might have significant contribution to the ET dynamics. In chromophores other than perylene faster vibrational relaxation and internal vibrational-energy redistribution can superimpose the coherent electron injection. The electron injection can even proceed from a thermalized excited donor state by means of a sequential mechanism being not so fast and efficient if it would start from a state with vibrational coherences. Alternative theoretical descriptions assume fast intramolecular redistribution [39, 114, 65]. In the present study vibrational relaxation is included employing Redfield theory without any restrictions concerning decoherence time, so that electron injection in more general cases can be treated. However, the calculation shall be limited to one PES configuration and one value of the system-bath coupling.

5.2 Model

The present study is based on the Hamiltonian (2.2) with system-bath separation and on the Redfield equation (2.9). The bath is treated quantum-mechanically and consists of uncoupled harmonic oscillators. The system-bath interaction is taken to be linear in the reaction coordinate as well as in the bath coordinates. Neither the RWA nor the SA are invoked.

The peculiarity of the model is the way how the conduction band is formulated as part of the system Hamiltonian H_S. It will be discretized by means of a manifold of vibronically uncoupled harmonic diabatic states to which we refer as quasicontinuum. The ground and the excited state of the chromophore are modeled by displaced diabatic potentials. The excited state of the chromophore is coupled to all states in the quasicontinuum through a single effective reaction mode. So, the Hamiltonian modeling the relevant system reads

$$H_\mathrm{S} = \sum_{i=g,e,k} H_i |\phi_i\rangle\langle\phi_i| + \sum_k (V_{ke}|\phi_k\rangle\langle\phi_e| + V_{ek}|\phi_e\rangle\langle\phi_k|). \tag{5.1}$$

Here g stands for the ground state, e for the excited state (donor state), and k for the quasicontinuum. As in Ref. [95] we choose the frequency of the reaction mode to be

$\omega_0 = 0.1$ eV. The electronic coupling between the excited state ϕ_e and the quasicontinuum states ϕ_k is assumed to be constant: $V_{ek} = 0.1$ eV. The Hamiltonian H_S is diagonalized and the RDM is propagated in the eigenstate representation (ER) so that the DDA is not performed. A box-shaped uniform density of states is used, i.e. the diabatic states of the quasicontinuum are equidistant. Instead of modeling the excitation from the ground state explicitly a δ-pulse will be assumed. The excited state PES is shifted with reorganization energy $0.67\omega_0$ along the reaction coordinate with respect to the ground state PES. This choice results in an initial vibrational wave packet on the excited state with significant population in the lowest 5 vibrational states. The shift between the excited state PES and the quasicontinuum parabola corresponds to a reorganization energy $2.7\omega_0$. A quantum model for the thermal bath is employed considering uncoupled harmonic oscillators. The bath is characterized by its spectral density which is taken to be of Ohmic form with exponential cutoff as defined in Eq. (2.36). Again, the normalization prefactor η is determined in such a way that the spectral densities in DR and ER coincide at ω_0 (see Chapter 2). The damping rate equals $\Gamma = \omega_0/10$ in the present simulation.

To be able to study the effects of dissipation we do not model the quasicontinuum with such a large number of electronic states as in Ref. [95]. In that work a band of width 2 eV was described using an energy difference of 2.5 meV leading to 801 electronic surfaces. These calculations are already demanding using wave function propagation but almost impossible using direct density matrix propagation. For treating such a large system one would have to use the stochastic wave function scheme as described in Chapter 3. We use a much simpler model and describe only that part of the conduction band which really takes part in the injection process. The total width of the conduction band may be significantly larger. In the following, a band of width 0.75 eV is treated with 31 electronic surfaces. In each of these electronic states five vibrational states are taken into account. The energy difference between the lowest state of the quasicontinuum and the minimum of the excited-state PES of the chromophore is equal to one half of the band width. We are aware that this is only a minimal model but hope that it catches the effects of vibrational dissipation on the electron injection process.

5.3 Results

Two different populations arising in the process of electron injection can help us uncover the influence of vibrational dissipation. The time-dependent population of the electronic states in the conduction band is calculated as the sum over the vibrational levels of each electronic surface $P(k,t) = \sum_n P_{k,n}(t) = \sum_n \rho_{kn,kn}(t)$. As a second quantity we look at the time-dependent population of the vibrational levels of the excited molecular state $P_e(m,t) = \rho_{em,em}$. These two probability distributions give some hints on the effect of dissipation.

Figure 5.2 shows the electronic population for the quasicontinuum, i.e. the probability distribution of the injected electron, versus the energy of the conduction band. As described above, the four lowest vibrational states are populated significantly at $t = 0$. The structure arising in the left panel of Fig. 5.2 was already explained by Ramakrishna

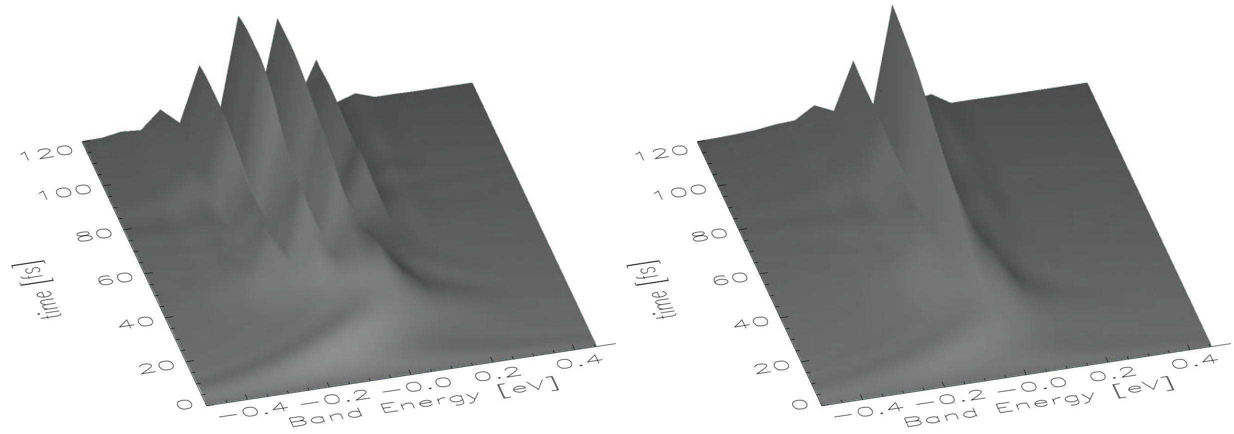

Figure 5.2: Probability distribution of the injected electron $P(k,t)$ without dissipation (left panel) and with dissipation (right panel).

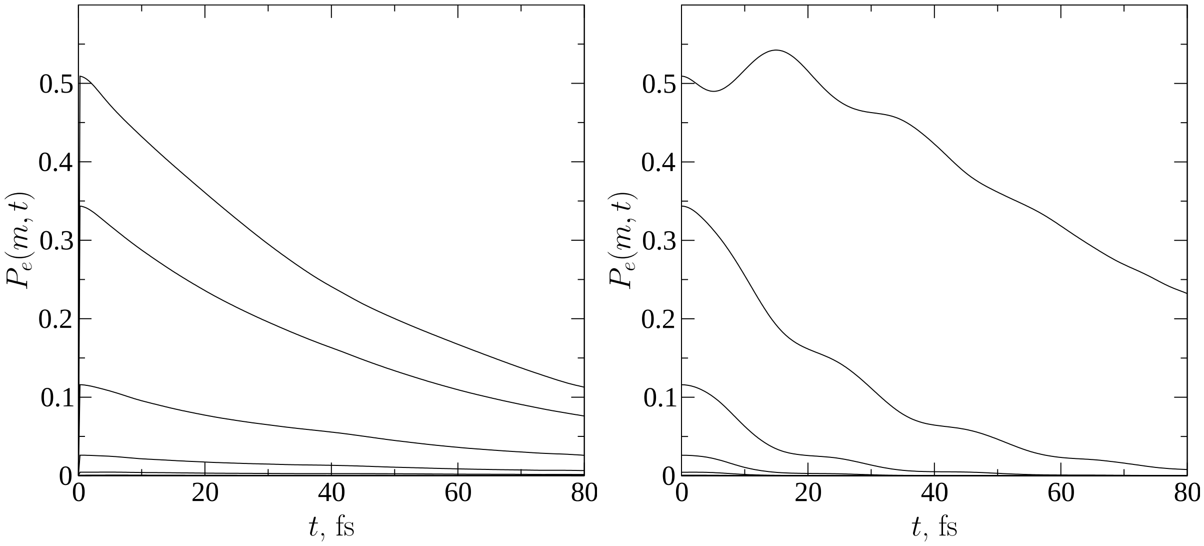

Figure 5.3: Population of the vibrational levels of the excited molecular state $P_e(m,t)$ without dissipation (left panel) and with dissipation (right panel). The lowest vibrational state is populated most at $t = 0$. The higher the vibrational quantum number the less populated is the level.

et al. [95]. Using the golden rule it can be estimated as

$$P(k,t) \propto \sum_{m,n} P_e(m,t=0)|\langle \chi_{em}|\chi_{kn}\rangle|^2 \delta(E_0 + m\omega_0 - E_k - n\omega_0) \tag{5.2}$$

where $|\chi_{em}\rangle$ and $|\chi_{kn}\rangle$ are the vibronic parts of the wave packet in the excited and quasicontinuum states, respectively. The energy E_0 denotes the center of the band. One can see that the probability distribution of the injected electron is nothing else but a Franck-Condon progression with peaks that are separated by ω_0 and broadened according to the electronic coupling with the donor state. The amplitudes of the peaks depend on the Franck-Condon factors $f(em;kn) = \langle \phi_{em}|\phi_{kn}\rangle$. All vibronic populations of the donor state $P_e(m,t)$ undergo a monotonous decay close to exponential at equal decay rates as shown in Fig. 5.3, in the left plot. They decay practically completely before the time at which the first recurrence starts, i.e. before $2\pi\hbar/(0.75/30) = 165$ fs[1]. This situation corresponds to a decay in the wide band limit [97].

Turning on the dissipation the following effects can be seen. The vibrational populations in the excited state of the chromophore are not only transfered into the quasicontinuum states but also relax within the excited state (see right plot in Fig. 5.3). Note that the population of the lowest vibronic level is initially increasing due to damping of higher levels but later (after 15 fs) decaying into the quasicontinuum. Oscillatory features in population decay become well pronounced with dissipation. The decay rates for all populated vibronic levels are different in contrast to the case without dissipation. As a result, the population distribution of the injected electron in the conduction band becomes narrower with the inclusion of dissipation as shown in Fig. 5.2 in the right plot. The recurrence of population from the quasicontinuum states is inhibited with dissipation due to damping and to dephasing in the quasicontinuum states. Only those parts of the wave packet which are still high enough in energy and interfere constructively with their counterpart in the chromophore can return to the donor state.

To summarize, we extended the work by Ramakrishna, Willig, and May [95] by including relaxation processes into the description of electron injection into the conduction band of a semiconductor. This will, at least, become important for modeling electron injection from a donor state with ultrafast vibrational relaxation or in the presence of a fluid surrounding the attached molecule (fast solvation). A variation of configuration parameters of the chromophore states and of the quasicontinuum, an inclusion of more than one reaction modes as well as applying various spectral densities of the bath are possibilities that the present model for dissipation offers but which are not explored in this study. It would be interesting to find the parameters which constitute the crossover between the regime with dominant coherent mechanism and the regimes with strong influence of the vibrational dissipation. Using the time evolution of the RDM the third-order polarization in a pump-probe experiment can be simulated and thus the pump-probe signal can be calculated, e.g. as was done for betaine-30 in Chapter 4.

---

[1] This simulation was carried out up to 120 fs only.

Chapter 6

Exciton transfer in biological systems

6.1 Introduction

Plants, algae, and some bacteria collect and transform the energy of sunlight into chemical energy with remarkably high efficiency. First, the light from a broad spectral range is absorbed by the antenna systems. The excitation is then transfered in a number of steps to the reaction center where a charge transfer takes place. This creates a non-equilibrium potential which drives reactions of synthesis. The antenna systems have very complicated supramolecular structure containing mainly chlorophyll molecules, carotenoids and proteins. In some bacterial photosystems, like *Rhodopseudomonas acidophila*, the arrangement of the peripheral light-harvesting antenna (LH2) is characterized by a symmetric ring structure. Recently, X-ray studies [78] found that the LH2 of these bacteria is composed of nine identical units each of which is formed of two proteins with bound bacteriochlorophylls. The units are located in space in such a way that a ring with radius about 2.5 nm of 18 chlorophyll molecules is sandwiched between the protein subunits. The structure can be also viewed as a ring with 9 dimers as shown in Fig. 6.1. Each chlorophyll molecule is coupled stronger to its partner in the dimer than to the molecules in the neighboring dimers. The nonrigid environment of the protein gives rise to static and dynamic disorder, i.e. local deviations in the spectral properties of every single chlorophyll molecule. If the fluctuations of the protein environment have much shorter correlation time compared to the characteristic timescale of the excitation transfer the disorder is regarded as dynamic. In the opposite limiting case static disorder is considered.

As the chlorophyll sites in the ring are coupled by dipole-dipole and exchange interactions the excitation can be delocalized over the ring and the dynamics of the system can be modeled by propagating a particle (exciton) in the ring structure. In the presence of disorder the dynamics of the exciton motion has incoherent relaxation behavior. Recent femtosecond spectroscopies provided a clear insight into the dynamics of energy transfer and relaxation in bacterial photosystems [85]. They detected a ultrafast decay of the anisotropy of fluorescence which is an experimental evidence for the incoherent behavior of the exciton dynamics.

The first theoretical approach to the coupled coherent and incoherent motion of excitons developed by Haken, Strobl and Reineker is based on the stochastic Liouville equa-

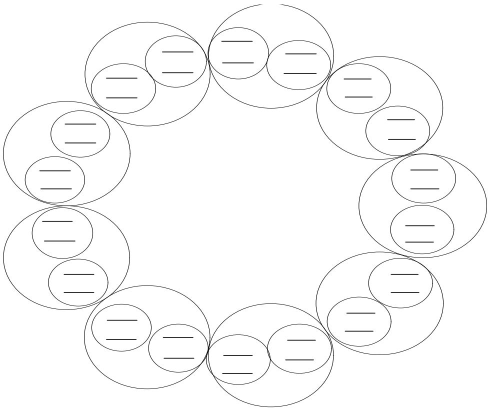

Figure 6.1: Sketch of the model ring structure. The dimers are depicted by large circles and the sites with single chlorophyll molecules by small circles.

tion (see Ref. [100] for a review). The coherent dynamics is described by a Hamiltonian containing the excitation energies at all sites (e.g. chlorophyll molecules) and the transfer matrix elements which model the Coulomb and exchange interactions between sites. The vibrations of the environment, parameterized as fluctuations of the excitation energies and of the transfer matrix elements, give rise to incoherent motion. Averaging over the fluctuations results in the stochastic Liouville equation for the density matrix. In another method [50] the incoherent exciton dynamics is described by the generalized master equation which has been applied to this problem without Markov approximation as well. Recently, Redfield theory was set up to describe the exciton propagation in a model ring structure with 18 chromophore molecules each described by a two-level system [41]. Taking into account the simultaneous influence of static and dynamic disorder this study gave an extension to the investigation by Kumble and Hochstrasser [63] who included only the effects of static disorder. One of the conclusions [41] was that the simulated time-dependent anisotropy of fluorescence is in agreement with experiment for lower values of the static disorder than in Ref. [63] due to the inclusion of dynamic disorder. There seem to exist different sets of microscopic parameters (especially with variation of static and dynamic disorder) which agree with experiment. Thus, there are still open questions concerning which physical effects and mechanisms are relevant for the behavior observed in experiments. In addition to dynamic disorder non-Markovian effects, related to the system-bath interaction, will be taken into account in the present work. For this purpose the time-convolutionless formulation of the QME of Čápek [14] will be used and numerically compared to Redfield theory.

6.2 Model

The total Hamiltonian of the model system reads [41]

$$H = H^0_{\rm ex} + H_{\rm s} + H_{\rm ph} + H_{\rm ex-ph} \tag{6.1}$$

where

$$H^0_{\rm ex} = \sum_{m,n} J_{mn} a^\dagger_m a_n \tag{6.2}$$

$$H_{\rm s} = \sum_m \epsilon_m a^\dagger_m a_m \tag{6.3}$$

$$H_{\rm ph} = \sum_\xi \omega_\xi b^\dagger_\xi b_\xi \tag{6.4}$$

$$H_{\rm ex-ph} = \frac{1}{\sqrt{N_{\rm B}}} \sum_{m,\xi} G^m_\xi \omega_\xi a^\dagger_m a_m (b^\dagger_\xi + b_{-\xi}). \tag{6.5}$$

The first term $H^0_{\rm ex}$ describes the transfer of a single exciton from one site of the ring to another. Operator $a^\dagger_m$ creates an exciton at site m while operator a_n destroys the exciton at site n. The non-diagonal elements of J_{mn} are transfer integrals and the diagonal elements are the local energies of the sites. The second term in Eq. (6.1) takes into account the fluctuations ϵ_m of the site energies J_{mm} assuming a Gaussian distribution with standard deviation Δ. The decay time of the time-correlation function of these fluctuations is assumed to be sufficiently long compared to the timescale of the exciton dynamics. Thus, the term $H_{\rm s}$ is regarded as static disorder. The next term, $H_{\rm ph}$ describes the phonon bath and the operators $b^\dagger_\xi$ and b_ξ create and annihilate a phonon, respectively. The exciton-phonon coupling term $H_{\rm ex-ph}$ is assumed to be site-diagonal and linear in the lattice displacements, i.e. it has the bilinear form (2.4). Dynamic disorder in the system is related to the exciton-phonon interaction $H_{\rm ex-ph}$, i.e. the dissipation. The first two terms of the total Hamiltonian (6.1) are regarded as a relevant part (see Eq. (2.2)) whose dynamics is described by an exciton RDM.

Considering a symmetric ring with $N_{\rm S}$ sites each with the same local energy J_{mm} and coupling only between neighboring sites, i.e. $J_{mn} = J(\delta_{m,n+1} + \delta_{m,n-1})$, the diagonalization of $H^0_{\rm ex}$ leads to the eigenstates (Frenkel excitons)

$$|\alpha\rangle = \frac{1}{\sqrt{N_{\rm S}}} \sum_{n=0}^{N_{\rm S}-1} e^{2\pi i k n / N_{\rm S}} |n\rangle \tag{6.6}$$

with the eigenenergies $E_\alpha = -2J\cos\alpha$, where $\alpha = 2\pi k/N_{\rm S}$, $k = 0, \pm1, \pm2, \ldots, \pm N_{\rm S}/2$. For a symmetric coplanar arrangement of site transition moments $\boldsymbol{\mu}_\alpha$ dipole-allowed transitions populate only the degenerate $k = \pm1$ levels of the ideal ring. When static disorder of the site energies is present ($\Delta \neq 0$) the eigenstates $|a\rangle$ of the Hamiltonian $H^0_{\rm ex} + H_{\rm s}$ correspond to mixtures of $|\alpha\rangle$ and an excitation will prepare a superposition of the $|\alpha\rangle$ states.

The dipole strength $\boldsymbol{\mu}_\alpha$ of state $|\alpha\rangle$ of the ideal ring $\boldsymbol{\mu}_a$ and the dipole strength of state $|a\rangle$ of the ring with static disorder read

$$\boldsymbol{\mu}_\alpha = \sum_{n=1}^{N_{\rm S}} c^\alpha_n \boldsymbol{\mu}_n, \qquad \boldsymbol{\mu}_a = \sum_{n=1}^{N_{\rm S}} c^a_n \boldsymbol{\mu}_n, \tag{6.7}$$

where c_n^α and c_n^a are the expansion coefficients of the eigenstates of the ideal and disordered rings, respectively, in site representation. Kumble and Hochstrasser [63] concluded, that in the case of pump-pulse excitation the dipole strength is simply redistributed among the exciton levels due to disorder. So the amplitudes of site excitations and the phase relationships in the initial state are necessarily identical to that of an equal superposition of $k = \pm 1$ excitons of the ideal ring. Thus, the excitation with a pump pulse of sufficiently wide spectral bandwidth will always prepare the same initial state, irrespective of the actual eigenstates of the real ring. This initial state is entirely determined by the selection rules of the ring without static disorder. After pulse excitation from an external field with polarization $\boldsymbol{e}_x$ the initial condition for the RDM is given by [85]

$$\rho_{\alpha\alpha'}(t = 0; \boldsymbol{e}_x) = \frac{1}{A}(\boldsymbol{e}_x \cdot \boldsymbol{\mu}_\alpha)(\boldsymbol{e}_x \cdot \boldsymbol{\mu}'_\alpha) \; . \tag{6.8}$$

where

$$A = \sum_\alpha (\boldsymbol{e}_x \cdot \boldsymbol{\mu}_\alpha)(\boldsymbol{e}_x \cdot \boldsymbol{\mu}_\alpha) \; . \tag{6.9}$$

The time-dependent anisotropy of fluorescence

$$r(t) = \frac{\langle S_{xx}(t)\rangle - \langle S_{xy}(t)\rangle}{\langle S_{xx}(t)\rangle + 2\langle S_{xy}(t)\rangle} \tag{6.10}$$

is a measure for the survival time of the exciton. It arises from the difference of the fluorescence signal upon pumping and probing with x- and y-polarized pulses and is experimentally detectable. The angular brackets in Eq. (6.10) denote the ensemble average as well as the average over the direction of the laser pulses with fixed relative directions $\boldsymbol{e}_x$ and $\boldsymbol{e}_y$. The signals $S_{xy}(t)$ can be calculated with use of the exciton RDM [41] as

$$S_{xy}(t) = A \int d\omega \sum_{a,a'} \rho_{aa'}(t)(\boldsymbol{e}_y \cdot \boldsymbol{\mu}_{a'})(\boldsymbol{e}_y \cdot \boldsymbol{\mu}_a)[\delta(\omega - \omega_{a'0}) + \delta(\omega - \omega_{a0})] \; . \tag{6.11}$$

The Hamiltonian (6.1) allows the use of Redfield theory provided that the exciton dynamics is not very fast and its coupling to the bath is weak. The dynamical problem can be then formulated by constructing the Redfield relaxation tensor $\mathcal{R}$ which enters the Redfield QME (2.10). Alternative description for the the dissipative exciton dynamics was proposed by Čápek [14] who derived a convolutionless master equation for the exciton RDM

$$\frac{d}{dt}\rho(t) = -i[H, \rho(t)] + i\delta\Omega(t)\rho(t). \tag{6.12}$$

It turned out [41] that for $t \to \infty$ the time-dependent relaxation tensor $i\delta\Omega(t)$ is identical with the Redfield tensor $\mathcal{R}$. Furthermore, it was shown [15] that the SA commonly used in the Redfield method can distort the correct short time evolution of physical quantities calculated by means of the RDM for exciton transfer problems. This is why SA will not be used in the present work. In order to take into account the non-Markovian effects the full time dependence of $\delta\Omega(t)$ [14, 56] has to be used rather than its long time approximation Eq. (2.10). Here we refer to the original work [14] for the derivation and for a detailed

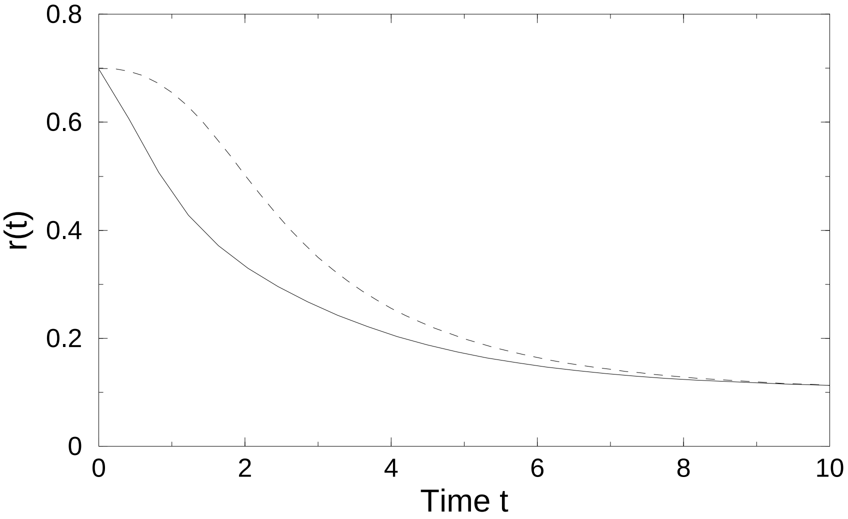

Figure 6.2: Decay of the anisotropy of fluorescence for a symmetric ring of 18 chromophore sites calculated with the Redfield equation (solid line) and with the non-Markovian QME (6.12) (dashed line). All units are relative to the transfer integral J_{12}. For example $t = 1$ corresponds to 21.1 fs for $J_{12} = 250\ \text{cm}^{-1}$. The results presented are for temperature $T = 1$ which is about 300 K for $J_{12} = 250\ \text{cm}^{-1}$, static disorder $\Delta = 0.2J_{12}$ and dynamic disorder $j_0 = 0.4J_{12}$.

discussion on Čápek's equation. Keeping the notation from Ref. [14] the tensor elements of $\delta\Omega(t)$ read

$$i\delta\Omega_{nm,qp}(t) = -\delta_{nq}\delta\mathcal{A}^{p}_{mn}(t) - \delta_{mp}\delta\mathcal{A}^{q*}_{nm}(t), \tag{6.13}$$

where

$$\begin{aligned}\delta\mathcal{A}^{p}_{mn}(t) &= \frac{1}{N_{\mathrm{B}}}\int\limits_0^t d\tau \sum_{\xi}\omega_{\xi}^2(G^m_{-\xi} - G^n_{-\xi})\sum_r G^r_{\xi}\left[(1+n(\omega_\xi))\,e^{i\omega_\xi\tau} + n(\omega_\xi)e^{-i\omega_\xi\tau}\right] \\ &\quad\times\sum_{aa'}\langle r|a\rangle\langle a|m\rangle\langle p|a'\rangle\langle a'|r\rangle e^{i\omega_{aa'}\tau}\end{aligned} \tag{6.14}$$

and $n(\omega) = 1/(e^{\beta\omega} - 1)$ is the Bose-Einstein distribution function. It should be noted that Eq. (6.12) is local in time although the relaxation tensor (6.13) contains a second-order kernel. The non-Markovian effects contained in $\delta\Omega(t)$ vanish within a short memory time τ_m. However, τ_m can influence strongly the dynamics at the early stage as shall be shown below.

The parameters in the present calculations are taken from Ref. [41]. As introduced, one has to distinguish the coupling between sites within one dimer by using the intra-dimer transfer integral J_{12} which is used as energy unit for all other parameters. The respective inter-dimer transfer integral was taken $J_{23} = 0.7J_{12}$. The bath is extended to a bath with infinite number of uncoupled harmonic oscillators, i.e. $N_{\mathrm{B}} \to \infty$, with spectral density

$$J(\omega) = \Theta(\omega) j_0 \frac{\omega^2}{2\omega_c^3} e^{-\omega/\omega_c} \tag{6.15}$$

where $\Theta(\omega)$ is the step function and ω_c the cut-off frequency. In this calculation $\omega_c = 0.2J_{12}$ and $j_0 = 0.4J_{12}$. The static disorder Δ and the temperature T are varied.

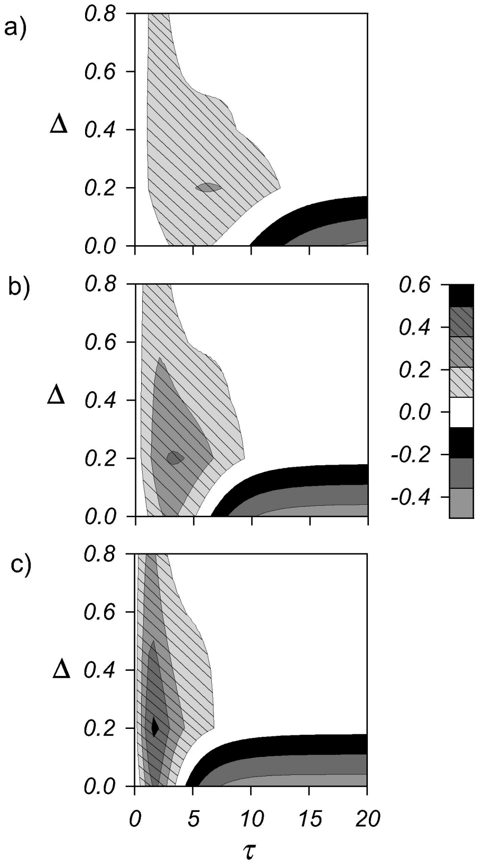

Figure 6.3: Difference between the non-Markovian and Markovian results of the anisotropy of fluorescence r for a symmetric ring at different times t and for different values of the static disorder Δ displayed for low (a), middle (b) and high temperatures (c).

For numerical time propagation of the density matrix ρ, i.e. for solving of Eq. (6.12), the SIA method [91] was used. This method was applied to an electron transfer problem with a stationary relaxation superoperator $\mathcal{R}$ [55] but it can be applied very successfully in the case of weak time dependence of $\mathcal{R}$ as well. It was pointed out that the advantage of the SIA method with respect to the standard RK scheme is the low computational costs for moderate accuracy [55]. Furthermore, the expansion coefficients are adapted at each time to a fixed time step with a prespecified tolerance in contrast to the RK scheme in which the time step has to be adapted. A uniform time grid is important for the averaging of various realizations at the same time points without interpolation. In order to reduce the computation time the code was parallelized by means of MPI [26] and the computation was performed on a cluster of 192 Pentium III nodes. Thus, only a sequence of 52 realizations of the static disorder had to be run on one node instead of all 9984 realizations in the case of serial implementation.

6.3 Results

We have used the non-Markovian dynamical equations for the exciton RDM ρ in Čápek's form Eq. (6.12) to express the time dependence of the optical properties of the model LH2 ring of BChls in the femtosecond time range. The simulated anisotropy of fluorescence is shown in Fig 6.2. It can be immediately seen that the non-Markovian correction gives rise to retardation of the decay even in this high temperature case. For long times ($t > 10$) Markovian and non-Markovian results converge to the same equilibrium value. In Ref. [63], the anisotropy of fluorescence of the LH2 ring decreases from 0.7 to $0.3 - 0.35$ and subsequently reaches a final value of 0.4. One needs a strength of static disorder of $\Delta \approx 0.4 - 0.8J$ to reach a decay time below 100 fs.

In the previous calculation [41] dynamic disorder (in addition to the static one) was also considered using Redfield theory. It led to faster decay during the initial stage. Smaller values of Δ than predicted in Ref. [63] would be sufficient to guarantee the decrease of the anisotropy $r(t)$ during the first 100 fs. The same is true if we use Čápek's non-Markovian equations [14]. According to our results (Fig. 6.3) the non-Markovian effects play a larger role at higher temperatures in which case the decay of anisotropy of fluorescence becomes slower. The time at which the anisotropy of fluorescence drops to 0.4 becomes longer by up to 50 %. So non-Markovian effects are by no means small at higher temperatures. There is a possible explanation of this finding. In Chapter 2 it was noted that the memory time τ_m, which is characteristic for the magnitude of non-Markovian effects, is system-specific as well [74]. In particular, initial correlations in $\rho(t = 0)$, which are neglected in this numerical simulation, can strongly influence the memory time. Their interplay with dynamic disorder and temperature can diversely change the memory time. Thus, initial correlations have to be taken into account in future studies.

Chapter 7

Conclusion

In this dissertation multilevel Redfield theory was used to numerically approach three different transfer problems. In addition, a few theoretical aspects concerning the modeling of coupled diabatic states in the framework of Redfield theory as well as numerical methods for solution of the Redfield QME were considered.

Of special interest was the influence of the intercenter coupling on the dissipation the neglect of which leads to the DDA. This issue is relevant not only for the ET model considered here but also for all microscopic models containing coupled diabatic states. With the help of first-order perturbation expansion in the electronic coupling it became possible to find an analytical expression for the relaxation operator Λ in DR. The population dynamics of a model two-center ET system in the case of the zeroth order of this perturbative treatment DR0, which is equivalent to DDA, was then compared with the dynamics adding the first order contribution (DR1) and using the exact formulation for Λ in ER. The DDA yields wrong population dynamics even for very small intercenter coupling in configurations with barrier as well as in the cases in which the energy levels of both diabatic states are not in resonance. Taking the first order contributions into account gave surprisingly good results — in the case of weak electronic coupling ($v = 0.1\omega_0$) they completely converged to the exact ER results. In these favorable cases the use of the DR1 rather than the ER formulation for Λ is advantageous due to the following reasons. First, one does not need to diagonalize the Hamiltonian of the relevant system H_S which for problems of high dimension and (or) large basis size is a tough, and sometimes, infeasible numerical task. Second, the populations are calculated by simple tracing which is a cheaper operation than matrix-matrix multiplication in the case of ER. Third, the perturbative approach allows one to separate the contributions from DR0 and DR1 at each moment of time and make conclusions about the mechanisms involved in the specific case. Benefiting from the latter feature different potential configurations of the ET model were analyzed by numerical comparison between DR0 and DR1. Small, moderate and strong electronic coupling and four representative potential configurations were considered. It was found that in the configurations with barrier, in which at least one level of the excited state lies below the crossing point of the diabatic potentials, the thermally assisted transfer mechanisms in DR1 predominate the purely coherent mechanism within DR0, particularly in the long-time limit. In contrast, in the case of configurations without barrier and in the Marcus inverted region, the coherent mechanisms contribute exclusively to the transfer dynamics. The role of the dissipation in the latter cases is reduced to damping within each diabatic state. Moreover, the damping rate determines the ET rate provided that the former is much smaller than the electronic coupling. For configurations within these limits and for small electronic coupling the DDA is by all means justified.

Further on, various numerical solving schemes for time-local QMEs were tested for their efficiency. The first group of direct propagation methods for the RDM included two versions of the Runge-Kutta method (RK), the short-iterative-Arnoldi (SIA) propagator, the Chebyshev polynomial (CP) propagator, the Newtonian polynomial (NP) propagator, and the symplectic integrator (SI). The Redfield equation was solved for a two-state single-coordinate ET model in DR and in ER. Apart from the highly accurate NP, which was used as a benchmark, the RK method from NAG exhibits the best performance both in DR and in ER. The other RK implementation, of the *Numerical Recipes* has a much worse performance in ER than in DR. The CP has limited accuracy of $\varepsilon \approx 10^{-8}$ even for very large numerical effort. A reasonable trade-off between numerical effort and accuracy is achieved using SIA with almost no change going from DR to ER.

Besides direct RDM propagators the stochastic wave function method was also implemented. This method allows to approach problems with very high dimensions or with a requirement for a large basis set. For a long time the approach had been limited to QMEs of Lindblad form. As the Redfield equation is not in Lindblad form we were motivated to develop a new stochastic unraveling scheme for generalized time-local QMEs. The new jump method is based on a doubled Hilbert space in which the state of the system is described by a pair of wave functions. Using the new method the QME for quantum Brownian motion and the Redfield QME for ET were successfully solved. However, the performance of the method has still to be verified with such an initial RDM for which no negative eigenvalues occur in time. This can be done with use of slippage of the initial conditions.

A real system with photoinduced ET in the inverted regime was also considered in the present studies. The system investigated here, betaine-30, is known to be very difficult due to the strong electronic intercenter coupling and to the low frequency mode relevant for the ET dynamics. In spite of this, the fully quantum-mechanical treatment based on the RDM with a model comprising two reaction modes yields rather meaningful results. First, the rates obtained in the two-mode model are in better agreement with experiment than the rates evaluated with the one-mode model. In addition, the recently proposed concept of two-stage mechanisms of ET in betaine-30 could be confirmed by the simulated pump-probe spectra. The nonlinear absorption and the stimulated emission maxima in the simulated transient at delay time of 300 fs are located exactly at the same wavelengths as those in the experimental spectra. In the future simulations without use of DDA will be carried out in order to revise the present conclusions. The expectations are that they will bring minor quantitative novelties as the long-time dynamics only is supposed to be affected by the use of DDA. Both the rate calculations and the simulated pump-probe spectra of betaine-30 showed that a more accurate, possibly self-consistent model for the spectral density is necessary for quantitatively correct results. A possibility in this respect is offered by molecular dynamics simulations. This remains outside the scope of the present thesis.

Extending the work by Ramakrishna, Willig, and May vibrational dissipation was included into the description of photoinduced electron ET between a surface-attached chromophore (perylene) and a semiconductor (TiO_2). The conduction band of TiO_2, acting as acceptor, was modeled with a quasi-continuum of discrete diabatic states. Using the Redfield QME this specific ET model was solved numerically. The structure of the electronic populations in the conduction band, found previously by Ramakrishna *et al.* by solving the time-dependent Schrödinger equation, was reproduced here in the case of coherent dynamics. Turning on the dissipation this distribution becomes narrower because of vibrational relaxation within the excited state of the chromophore. Furthermore, due to dephasing and damping in the electronic states of the quasi-continuum the population recurrences in the excited state of the chromophore become weaker with time. Thus, the relaxation effects (damping and dephasing), already known from simple ET models, modify the dynamics of the injected electron in a specific way.

The formulation of Redfield theory allowed to treat also other transfer processes such as photoinduced exciton transfer in a ring of 18 coupled two-level subsystems each modeling a bacteriochlorophyll molecule. The new issue in the current work is the inclusion of non-Markovian effects using a time-convolutionless QME for the RDM. They give rise to significant retardation of the decay of the anisotropy of fluorescence. It was found that non-Markovian effects influence the dynamics stronger for higher temperatures. This can be only due to the fact that the memory time τ_m, for which the memory kernel decays, is dependent on but not necessarily identical with the bath correlation time τ_c. The memory time depends also on the choice of the initial RDM. Initial correlations can play a decisive role in the characterization of non-Markovian effects. This is why they have to be taken into account in future studies.

Appendix A

Calculation of Λ_{nm}

The purpose of this appendix is to show some more details for the evaluation of $\langle n|\Lambda|m\rangle$. To calculate

$$\langle n|K^{\mathrm{I}}(-t)|m\rangle \;=\; \sum_{i,j}\langle n|e^{-iHt}|i\rangle\langle i|K|j\rangle\langle j|e^{iHt}|m\rangle \tag{A.1}$$

the operator identity [64]

$$e^{-i(H_0+V)t} = e^{-iH_0t}\left(1 - i\int\limits_0^t dt' e^{it'H_0}Ve^{-it'(H_0+V)}\right) \;, \tag{A.2}$$

which can easily be proven by multiplying both sides with e^{iH_0t} and differentiating with respect to t, is used iteratively. It yields

$$\begin{aligned}\langle n|e^{-iHt}|i\rangle &= \langle n|e^{-iH_0t}[1 - i\int\limits_0^t dt' e^{it'H_0}Ve^{-it'H_0}]|i\rangle + \mathcal{O}(V^2)\\ &= e^{-iE_it}\delta_{ni} - ie^{-iE_nt}\langle n|V|i\rangle\int\limits_0^t dt' e^{i(E_n-E_i)t'} + \mathcal{O}(V^2)\\ &= e^{-iE_it}\delta_{ni} - \frac{\langle n|V|i\rangle}{E_n - E_i}(e^{-iE_it} - e^{-iE_nt}) + \mathcal{O}(V^2)\end{aligned} \tag{A.3}$$

assuming that $E_n \neq E_i$. Here and in the following we only give the general expressions for the matrix elements. If a singularity can appear due to coinciding frequencies the appropriate expression can be obtained by taking the proper limit.

Thus the matrix element (A.1) is given by

$$\begin{aligned}\langle n|K^{\mathrm{I}}(-t)|m\rangle &= e^{i\omega_{mn}t}\langle n|K|m\rangle\\ &\quad -\sum_j\langle n|K|j\rangle\frac{\langle j|V|m\rangle}{\omega_{jm}}(e^{i\omega_{mn}t} - e^{i\omega_{jn}t})\\ &\quad -\sum_i\langle i|K|m\rangle\frac{\langle n|V|i\rangle}{\omega_{ni}}(e^{i\omega_{mi}t} - e^{i\omega_{mn}t}) + \mathcal{O}(V^2)\;.\end{aligned} \tag{A.4}$$

This result is inserted into Eq. (2.30). One has to evaluate integrals of the kind

$$\int_0^\infty dt e^{-\epsilon t} e^{-i(\omega-\omega_{mn})t} = \frac{-i}{\omega - \omega_{mn} - i\epsilon} \tag{A.5}$$

which contain a convergence parameter ϵ. Using the well known Plemelj identity

$$\lim_{\epsilon\to 0} \frac{1}{x \pm i\epsilon} = PV\frac{1}{x} \mp i\pi\delta(x) \tag{A.6}$$

one gets for the first term of the matrix element of Λ

$$\langle n|\Lambda|m\rangle = \frac{\pi}{1-e^{-\beta\omega_{mn}}}[J(\omega_{mn}) - J(-\omega_{mn})]\langle n|K|m\rangle + (\text{Lamb shift}) + \ldots$$

The Lamb shift is the imaginary part of the matrix element of Λ and leads to an energy shift in the quantum master equation. This term is a small correction [34] and is neglected in Redfield theory. The other terms of the matrix elements are calculated in the same fashion yielding

$$\begin{aligned}\langle n|\Lambda|m\rangle = {} & \frac{\pi}{1-e^{-\beta\omega_{mn}}}[J(\omega_{mn}) - J(-\omega_{mn})]\langle n|K|m\rangle \\ & - \sum_j \langle n|K|j\rangle \frac{\langle j|V|m\rangle}{\omega_{jm}} \left\{ \frac{\pi}{1-e^{-\beta\omega_{mn}}}[J(\omega_{mn}) - J(-\omega_{mn})] \right. \\ & \left. - \frac{\pi}{1-e^{-\beta\omega_{jn}}}[J(\omega_{jn}) - J(-\omega_{jn})] \right\} \\ & - \sum_i \langle i|K|m\rangle \frac{\langle n|V|i\rangle}{\omega_{ni}} \left\{ \frac{\pi}{1-e^{-\beta\omega_{mn}}}[J(\omega_{mn}) - J(-\omega_{mn})] \right. \\ & \left. - \frac{\pi}{1-e^{-\beta\omega_{mi}}}[J(\omega_{mi}) - J(-\omega_{mi})] \right\} \; . \end{aligned} \tag{A.7}$$

Appendix B

Stochastic wave function algorithm

B.1 The standard quantum jump method

This algorithm gives the numerical solution of the SSE (3.22). The initial density matrix $\rho_{\mathrm{S}}(0)$, describing in general a mixed state, is represented by a set of ket-vectors $|\psi_{i,s}(0)\rangle$ such that

$$\rho_{\mathrm{S}}(0) = \sum_{i=1}^{N_e} w_i \frac{1}{N_{\mathrm{S}}} \sum_{s=1}^{N_{\mathrm{S}}} |\psi_{i,s}(0)\rangle\langle\psi_{i,s}(0)| \tag{B.1}$$

where w_i are the eigenvalues of $\rho_{\mathrm{S}}(0)$ and N_{S} is the number of trajectories (stochastic realizations) which for simplicity is chosen the same for each pure state (eigenvector of $\rho_{\mathrm{S}}(0)$). Next, using the Lindblad operators from Eq. (2.7) one defines an effective non-Hermitian Hamiltonian

$$H_{\mathrm{eff}} = H_{\mathrm{S}} + \frac{i}{2} \sum_k L_k^\dagger L_k \ . \tag{B.2}$$

Starting at $t = 0$ the following procedure runs independently for each trajectory $|\psi_{i,s}(t)\rangle$

```
1. store/send $|\psi_{i,s}(t)\rangle$ for averaging
2. calculate $p_k = \langle\psi_{i,s}(t)|L_k^\dagger L_k|\psi_{i,s}(t)\rangle$
3. extract a random number $\epsilon \in (0,1)$
4. if $\epsilon > dt \sum_k p_k$ then
       ∗ find $|\psi_{i,s}(t+dt)\rangle$ solving $d|\psi_{i,s}(t)\rangle/dt = -iH_{\mathrm{eff}}|\psi_{i,s}(t)\rangle$
       ∗ let $t = t + dt$
       ∗ renormalize $|\psi_{i,s}(t)\rangle$
       ∗ go to step 1
   else
       ∗ perform a jump using the probabilities $p_k dt$: $|\psi_{i,s}(t)\rangle \rightarrow L_k|\psi_{i,s}(t)\rangle/\sqrt{p_k}$
       ∗ go to step 2
```

Either at the end of the time propagation or at each step during the propagation the solution $\rho_\mathrm{S}(t)$ of the Lindblad QME (2.7) is obtained by averaging over all single realizations $|\psi_{i,s}(t)\rangle$ taken from step 1

$$\rho_\mathrm{S}(t) = \sum_{i=1}^{N_e} w_i \frac{1}{N_\mathrm{S}} \sum_{s=1}^{N_\mathrm{S}} |\psi_{i,s}(t)\rangle\langle\psi_{i,s}(t)| \ . \tag{B.3}$$

One does not need to recover the RDM in order to compute the ensemble-averaged expectation value of an observable A. In this case it is numerically advantageous to use the wave functions directly:

$$\overline{\langle A(t)\rangle} = \sum_{i=1}^{N_e} w_i \frac{1}{N_\mathrm{S}} \sum_{s=1}^{N_\mathrm{S}} \langle\psi_{i,s}(t)|A|\psi_{i,s}(t)\rangle \ . \tag{B.4}$$

B.2 The new quantum jump method

This algorithm gives the numerical solution of the SSEs (3.31) and (3.32). The wave functions $|\psi_{i,s}(0)\rangle$ and $|\phi_{i,s}(0)\rangle$ are constructed so that

$$\rho_\mathrm{S}(0) = \sum_{i=1}^{N_e} w_i \frac{1}{N_\mathrm{S}} \sum_{s=1}^{N_\mathrm{S}} \left[|\phi_{i,s}(0)\rangle\langle\psi_{i,s}(0)| + |\psi_{i,s}(0)\rangle\langle\phi_{i,s}(0)|\right] \ . \tag{B.5}$$

and propagated jointly (as pairs) as follows starting with $t = 0$

```
1. store/send $|\psi_{i,s}(t)\rangle$ and $|\phi_{i,s}(t)\rangle$ for averaging
2. calculate $p_k^1$ and $p_k^2$ according to Eqs. (3.36) and (3.37)
3. extract a random number $\epsilon \in (0,1)$
4. if $\epsilon > dt \sum_k (p_k^1 + p_k^2)$ then
       * find $|\psi_{i,s}(t+dt)\rangle$ and $|\phi_{i,s}(t+dt)\rangle$ solving
         $d|\psi_{i,s}(t)\rangle/dt = A|\psi_{i,s}(t)\rangle$ and $d|\phi_{i,s}(t)\rangle/dt = A|\phi_{i,s}(t)\rangle$ respectively
       * let $t = t + dt$
       * renormalize $|\psi_{i,s}(t)\rangle$ and $|\phi_{i,s}(t)\rangle$
       * go to step 1
   else
       * if $\epsilon \leq dt \sum_k p_k^1$ then
           – jump with probability $p_k^1 dt$:
             $|\psi_{i,s}(t)\rangle \rightarrow E_k|\psi_{i,s}(t)\rangle/\sqrt{p_k^1}$ and $|\phi_{i,s}(t)\rangle \rightarrow C_k|\psi_{i,s}(t)\rangle/\sqrt{p_k^1}$
         else
           – jump with probability $p_k^2 dt$:
             $|\psi_{i,s}(t)\rangle \rightarrow C_k|\psi_{i,s}(t)\rangle/\sqrt{p_k^2}$ and $|\phi_{i,s}(t)\rangle \rightarrow E_k|\psi_{i,s}(t)\rangle/\sqrt{p_k^2}$
```

- $*$ go to step 2

The ensemble-averaged expectation value of an observable A is calculated as

$$\overline{\langle A(t)\rangle} = \sum_{i=1}^{N_e} w_i \frac{1}{N_{\mathrm{S}}} \sum_{s=1}^{N_{\mathrm{S}}} \left[\langle \psi_{i,s}(t)|A|\phi_{i,s}(t)\rangle + \mathrm{c.c.}\right] \ . \tag{B.6}$$

Both methods (Sec. B.1 and Sec. B.2) can be parallelized using MPI [26]. In such an implementation every single stochastic trajectory is propagated by a different process. Only the averaging operations (B.4) and (B.6) are done at certain times by means of collective communications. In this way the task can be efficiently distributed on a cluster of PCs.

Bibliography

[1] E. Åkesson, A. E. Johnson, N. E. Levinger, G. C. Walker, T. P. DuBruil, and P. F. Barbara, *Temperature dependence of the inverted regime electron transfer kinetics of betaine-30 and the role of molecular modes*, J. Chem. Phys. **96**, 7859 (1992).

[2] E. Åkesson, G. C. Walker, and P. F. Barbara, *Dynamic solvent effects on electron transfer rates in the inverted regime: Ultrafast studies on the betaines*, J. Chem. Phys. **95**, 4188 (1991).

[3] J. B. Asbury, E. Hao, Y. Wang, H. N. Ghosh, and T. Lian, *Femtosecond IR Study of Excited-State Relaxation and Electron-Injection Dynamics of* $Ru(dcbpy)_2(NCS)_2$ *in Solution and on Nanocrystalline* TiO_2 *and* Al_2O_3 *Thin Films*, J. Phys. Chem. B **103**, 3110 (1999).

[4] G. Ashkenazi, R. Kosloff, S. Ruhman, and H. Tal-Ezer, *Newtonian propagation methods to the photodissociation dynamics of* I_3^-, J. Chem. Phys. **103**, 10005 (1995).

[5] P. F. Barbara, T. J. Meyer, and M. A. Ratner, *Contemporary issues in electron transfer research*, J. Phys. Chem. **100**, 13148 (1996).

[6] M. C. Beard, G. M. Turner, and C. A. Schmuttenmaer, *Measurement of Electromagnetic Radiation Emitted during Rapid Intramolecular Electron transfer*, J. Am. Chem. Soc. **122**, 11541 (2000).

[7] M. Berman, R. Kosloff, and H. Tal-Ezer, *Solution of the time-dependent Liouville-von Neumann equation: dissipative evolution*, J. Phys. A: Math. Gen. **25**, 1283 (1992).

[8] M. Bixon and J. Jortner, *Electron transfer – from isolated molecules to biomolecules*, Adv. Chem. Phys. **106&107**, 35 (1999).

[9] K. Blum, *Density Matrix Theory and Applications*, Plenum Press, New York – London, 1996.

[10] R. W. Brankin, I. Gladwell, and L. F. Shampine, *RKSUITE: A suite of Runge-Kutta codes for the initial value problems for ODEs.*, Tech. Report SoftReport 92-S1, Department of Mathematics, Southern Methodist University, Dallas, TX, 1992, Available online at `http://www.netlib.no/netlib/ode/rksuite`.

[11] H.-P. Breuer, B. Kappler, and F. Petruccione, *Stochastic wave-function approach to the calculation of multitime correlation functions of open quantum systems*, Phys. Rev. A **56**, 2334 (1997).

[12] ———, *Stochastic wave-function method for non-Markovian quantum master equations*, Phys. Rev. A **59**, 1633 (1999).

[13] B. Burfeindt, T. Hannappel, W. Storck, and F. Willig, *Measurement of Temperature-Independent Femtosecond Interfacial Electron Transfer from an Anchored Molecular Electron Donor to a Semiconductor as Acceptor*, J. Phys. Chem. **100**, 16463 (1996).

[14] V. Čápek, *Carrier transfer in inhomogeneous media*, Z. Phys. B **99**, 261 (1996).

[15] V. Čápek, I. Barvík, and P. Heřman, *Towards proper parametrization in the exciton transfer and relaxation problem: dimer*, Chem. Phys. **270**, 141 (2001).

[16] N. J. Cherepy, G. P. Smestad, M. Grätzel, and J. Z. Zhang, *Ultrafast Electron Injection: Implications for a Photoelectrochemical Cell Utilizing an Anthocyanin Dye-Sensitized TiO_2 Nanocrystalline Electrode*, J. Phys. Chem. B **101**, 9342 (1997).

[17] G. L. Closs, L. T. Calcaterra, N. J. Green, K. W. Penfield, and J. R. Miller, *Distance, Stereoelectronic Effects, and the Marcus Inverted Region in Intramolecular Electron Transfer in Organic Radical Anions*, J. Phys. Chem. **90**, 3673 (1986).

[18] M. Cuperlovic, G. H. Meresi, W. E. Palke, and J. T. Gerig, *Spin Relaxation and Chemical Exchange in NMR Simulation*, J. Magn. Reson. **142**, 11 (2000).

[19] J. Dalibard, Y. Castin, and K. Mølmer, *Wave-Function Approach to Dissipative Processes in Quantum Optics*, Phys. Rev. Lett. **68**, 580 (1992).

[20] W. B. Davis, M. R. Wasielewski, R. Kosloff, and M. A. Ratner, *Semigroup Representations, Site Couplings, and Relaxation in Quantum Systems*, J. Phys. Chem. A **102**, 9360 (1998).

[21] W. Domcke and G. Stock, *Theory of ultrafast nonadiabatic excited-state processes and their spectroscopic detection in real time*, Adv. Chem. Phys. **100**, 1 (1997).

[22] F. E. van Dorsselaer and G. Nienhuis, *Quantum trajectories generalized*, J. Opt. B: Quantum Semiclass. Opt. **2**, L5 (2000).

[23] D. Egorova, A. Kühl, and W. Domcke, *Modeling of ultrafast electron-transfer dynamics: multi-level Redfield theory and validity of approximations*, Chem. Phys. **268**, 105 (2001).

[24] T. Felbinger and M. Wilkens, *Stochastic Wave-function Simulation of Two-time Correlation Functions*, J. Mod. Opt. **46**, 1401 (1999).

[25] A. K. Felts, W. T. Pollard, and R. A. Friesner, *Multilevel Redfield treatment of bridge-mediated long-range electron transfer: A mechanism for anomalous distance dependence*, J. Phys. Chem. **99**, 2929 (1995).

[26] Message Passing Interface Forum, *MPI: A message-passing interface standard*, Tech. Report CS-94-230, Computer Science Dept., University of Tennessee, Knoxville, TN, 1994, Available online at `http://www-unix.mcs.anl.gov/mpi/index.html`.

[27] C. Fuchs and M. Schreiber, *Electron transfer of betaine-30 in the inverted region*, J. Chem. Phys. **105**, 1023 (1996).

[28] C. W. Gardiner, *Handbook of Stochastic Methods*, Springer, Berlin, 1985.

[29] C. W. Gardiner, A. S. Parkins, and P. Zoller, *Wave-function quantum stochastic differential equations and quantum-jump simulation methods*, Phys. Rev. A **46**, 4363 (1992).

[30] B. M. Garraway and P. L. Knight, *Comparison of quantum-state diffusion and quantum-jump simulations of two-photon processes in a dissipative environment*, Phys. Rev. A **49**, 1266 (1994).

[31] B. M. Garraway and K.-A. Suominen, *Wave-packet dynamics: new physics and chemistry in femto-time*, Rep. Prog. Phys. **58**, 365 (1995).

[32] P. Gaspard and M. Nagaoka, *Non-Markovian stochastic Schrödinger equation*, J. Chem. Phys. **111**, 5676 (1999).

[33] ______, *Slippage of initial conditions for the Redfield master equation*, J. Chem. Phys. **111**, 5668 (1999).

[34] E. Geva, E. Rosenman, and D. Tannor, *On the second-order corrections to the quantum canonical equilibrium density matrix*, J. Chem. Phys. **113**, 1380 (2000).

[35] N. Gisin and I. C. Percival, *The quantum-state diffusion model applied to open systems*, J. Phys. A: Math. Gen. **25**, 5677 (1992).

[36] I. Goychuk, L. Hartmann, and P. Hänggi, *Semiclassical electron transfer: Zusman equations versus Langevin approach*, Chem. Phys. **268**, 151 (2001).

[37] S. K. Gray, D. W. Noid, and B. G. Sumpter, *Symplectic integrators for large scale molecular dynamics simulations: A comparison of several explicit methods*, J. Chem. Phys. **101**, 4062 (1994).

[38] H. Guo and R. Chen, *Short-time Chebyshev propagator for the Liouville-von Neumann equation*, J. Chem. Phys. **110**, 6626 (1999).

[39] L.-H. Guo, S. Mukamel, and G. McLendon, *Photophysical Probes of a Protein/Semiconductor Electrode Interface*, J. Am. Chem. Soc. **117**, 546 (1995).

[40] T. Hannappel, B. Burfeindt, W. Storck, and F. Willig, *Measurement of Ultrafast Photoinduced Electron Transfer from Chemically Anchored Ru-Dye Molecules into Empty Electronic States in a Colloidal Anatase TiO_2 Film*, J. Phys. Chem. B **101**, 6799 (1997).

[41] P. Heřman, U. Kleinekathöfer, I. Barvík, and M. Schreiber, *Influence of static and dynamic disorder on the anisotropy of emission in the ring antenna subunits of purple bacteria photosynthetic systems*, Chem. Phys. **275**, 1 (2002).

[42] S. Hogiu, W. Werncke, M. Pfeiffer, J. Dreyer, and T. Elsaesser, *Mode-specific vibrational excitation and energy redistribution after ultrafast intramolecular electron transfer*, J. Chem. Phys. **113**, 1587 (2000).

[43] W. Huisinga, L. Pesce, R. Kosloff, and P. Saalfrank, *Faber and Newton polynomial integrators for open-system density matrix propagation*, J. Chem. Phys. **110**, 5538 (1999).

[44] T. Ishida and P. J. Rossky, *Solvent Effects on Solute Electronic Structure and Properties: Theoretical Study of a Betaine Dye Molecule in Polar Solvents*, J. Phys. Chem. A **105**, 558 (2001).

[45] J. M. Jean, *Vibrational coherence effects on electronic curve crossing*, J. Chem. Phys. **104**, 5638 (1996).

[46] ______, *Excitation Effects on the Quantum Dynamics of Two-Dimensional Photoinduced Nonadiabatic Processes*, J. Phys. Chem. A **102**, 7549 (1998).

[47] J. M. Jean, R. A. Friesner, and G. R. Fleming, *Application of a multilevel Redfield theory to electron transfer in condensed phases*, J. Chem. Phys. **96**, 5827 (1992).

[48] J. Jortner and M. Bixon, *Intramolecular vibrational excitations accompanying solvent-controlled electron transfer reactions*, J. Chem. Phys. **88**, 167 (1988).

[49] C. Kalyanaraman and D. G. Evans, *Symplectic integrators for the multilevel Redfield equation*, Chem. Phys. Lett. **324**, 459 (2000).

[50] V. M. Kenkre, *The Master Equation Approach: Coherence, Energy Transfer, Annihilation, and Relaxation*, in: Exciton Dynamics in Molecular Crystals and Aggregates (G. Höhler, ed.), Springer Tracts in Modern Physics, vol. 94, Springer, Berlin, 1982, pp. 1–109.

[51] A. M. Kjaer and J. Ulstrup, *Solvent Bandwidth Dependence and Band Asymmetry Features of Charge-Transfer Transitions in N-Pyridinium Phenolates*, J. Am. Chem. Soc. **109**, 1934 (1987).

[52] U. Kleinekathöfer, I. Kondov, and M. Schreiber, *Perturbative treatment of intercenter coupling in the framework of Redfield theory*, Chem. Phys. **268**, 121 (2001).

[53] D. Kohen, C. C. Marston, and D. J. Tannor, *Phase space approach to theories of quantum dissipation*, J. Chem. Phys. **107**, 5236 (1997).

[54] D. Kohen and D. J. Tannor, *Classical-quantum correspondence in the Redfield equation and its solutions*, J. Chem. Phys. **107**, 5141 (1997).

[55] I. Kondov, U. Kleinekathöfer, and M. Schreiber, *Efficiency of different numerical methods for solving Redfield equations*, J. Chem. Phys. **114**, 1497 (2001).

[56] M. V. Korolkov and G. K. Paramonov, *State-selective vibrational excitation of diatomic molecules coupled to a quasiresonant environment: Markov approximation and non-Markov approach*, Phys. Rev. A **55**, 589 (1997).

[57] R. Kosloff, *Propagation Methods for Quantum Molecular Dynamics*, Annu. Rev. Phys. Chem. **45**, 145 (1994).

[58] ______, *Quantum Molecular Dynamics on Grids*, in: Dynamics of Molecules and Chemical Reactions (R. E. Wyatt and J. Z. H. Zhang, eds.), Marcel Dekker, New York, 1996, pp. 185–230.

[59] R. Kosloff, M. A. Ratner, and W. B. Davis, *Dynamics and relaxation in interacting systems: Semigroup methods*, J. Chem. Phys. **106**, 7036 (1997).

[60] S. A. Kovalenko, A. L. Dobryakov, J. Ruthmann, and N. P. Ernsting, *Femtosecond spectroscopy of condensed phases with chirped supercontinuum probing*, Phys. Rev. A **59**, 2369 (1999).

[61] S. A. Kovalenko, N. Eilers-König, T. A. Senyushkina, and N. P. Ernsting, *Charge Transfer and Solvation of Betaine-30 in Polar Solvents – A Femtosecond Broadband Transient Absorption Study*, J. Phys. Chem. A **105**, 4834 (2001).

[62] O. Kühn, V. May, and M. Schreiber, *Dissipative vibrational dynamics in a curve-crossing system*, J. Chem. Phys. **101**, 10404 (1994).

[63] R. Kumble and R. M. Hochstrasser, *Disorder-induced exciton scattering in the light-harvesting systems of purple bacteria: Influence on the anisotropy of emission and band-band transitions*, J. Chem. Phys. **109**, 855 (1998).

[64] B. B. Laird, J. Budimir, and J. L. Skinner, *Quantum-mechanical derivation of the Bloch equations: Beyond the weak coupling limit*, J. Chem. Phys. **94**, 4391 (1991).

[65] J. M. Lanzafame, S. Palese, D. Wang, R. J. D. Miller, and A. A. Muenter, *Ultrafast Nonlinear Optical Studies of Surface Reaction Dynamics: Mapping the Electron Trajectory*, J. Phys. Chem. **98**, 11020 (1994).

[66] C. Leforestier, R. H. Bisseling, C. Cerjan, M. D. Feit, R. Friesner, A. Guldberg, A. Hammerich, G. Jolicard, W. Karrlein, H.-D. Meyer, N. Lipkin, O. Roncero, and R. Kosloff, *A Comparison of Different Propagation Schemes for the Time Dependent Schrödinger Equation*, J. Comp. Phys. **94**, 59 (1991).

[67] J. Lobaugh and P. J. Rossky, *Computer simulation of the excited state dynamics of betaine-30 in acetonitrile*, J. Phys. Chem. A **103**, 9432 (1999).

[68] ———, *Solvent and Intramolecular effects on the Absorption Spectrum of Betaine-30*, J. Phys. Chem. A **104**, 899 (2000).

[69] A. Lochschmidt, N. Eilers-König, N. Heineking, and N. P. Ernsting, *Femtosecond Photodissociation Dynamics of Bis(julolidine) Disulfide in Polar and Apolar Solvents*, J. Phys. Chem. A **103**, 1776 (1999).

[70] N. Makri, *Quantum Dissipative Dynamics: A Numerically Exact Methodology*, J. Phys. Chem. A **102**, 4414 (1998).

[71] N. Makri, E. Sim, D. Makarov, and M. Topaler, *Long-time quantum simulation of the primary charge separation in bacterial photosynthesis*, Proc. Natl. Acad. Sci. USA (Biophysics) **93**, 3926 (1996).

[72] R. A. Marcus, *On the Theory of Oxidation-Reduction Reactions Involving Electron Transfer*, J. Chem. Phys. **24**, 966 (1956).

[73] ———, *Electron transfer reactions in chemistry. Theory and experiment*, Rev. Mod. Phys. **65**, 599 (1993).

[74] V. May and O. Kühn, *Charge and Energy Transfer Dynamics in Molecular Systems*, Wiley-VCH, Berlin, 2000.

[75] V. May, O. Kühn, and M. Schreiber, *Density matrix description of ultrafast dissipative wave packet dynamics*, J. Phys. Chem. **97**, 12591 (1993).

[76] V. May and M. Schreiber, *Electron-transfer dynamics in a donor-acceptor complex*, Chem. Phys. Lett. **181**, 267 (1991).

[77] ———, *Density-matrix theory of charge transfer*, Phys. Rev. A **45**, 2868 (1992).

[78] G. McDermott, S. M. Prince, A. A. Freer, A. M. Hawthornwaite-Lawless, M. Z. Paziz, R. J. Cogdell, and N. W. Isaacs, *Crystal structure of an integral membrane light-harvesting complex from photosynthetic bacteria*, Nature **374**, 517 (1995).

[79] R. I. McLachlan and P. Atela, *The accuracy of symplectic integrators*, Nonlinearity **5**, 541 (1992).

[80] C. Meier and D. J. Tannor, *Non-Markovian evolution of the density operator in the presence of strong laser fields*, J. Chem. Phys. **111**, 3365 (1999).

[81] S. R. Mente and M. Maroncelli, *Computer Simulations of the Solvatochromism of Betaine-30*, J. Phys. Chem. B **103**, 7704 (1999).

[82] S. Meyer and V. Engel, *Non-perturbative wave-packet calculations of time-resolved four-wave-mixing signals*, Appl. Phys. B **71**, 293 (2000).

[83] S. Mukamel, *Principles of Nonlinear Optical Spectroscopy*, Oxford University Press, New York – Oxford, 1995.

[84] The Numerical Algorithms Group Ltd, *Fortran Library*, Mark 18 (Oxford), `http://www.nag.co.uk/numeric/fl/manual/html/FLlibrarymanual.asp`.

[85] V. Nagarajan, E. T. Johnson, J. C. Williams, and W. W. Parson, *Femtosecond Pump-Probe Spectroscopy of the B850 Antenna Complex of Rhodobacter sphaeroides at Room Temperature*, J. Phys. Chem. B **103**, 2297 (1999).

[86] P. Nettesheim, W. Huisinga, and C. Schütte, *Chebyshev Approximation for Wave Packet Dynamics: better than expected*, Tech. Report SC 96-47, Konrad-Zuse-Zentrum für Informationstechnik, Berlin, 1996, Available online at `ftp://ftp.zib.de/pub/zib-publications/reports/SC-96-47.ps`.

[87] M. C. M. O'Brien, *The dynamic Jahn-Teller effect with many frequencies: a simple approach to a complicated problem*, J. Phys. C **5**, 2045 (1972).

[88] The Portland Group, Inc. (PGI), *PGF90*, Version 3.0 (Portland, USA), `http://www.pgroup.com`.

[89] M. B. Plenio and P. L. Knight, *The quantum-jump approach to dissipative dynamics in quantum optics*, Rev. Mod. Phys. **70**, 101 (1998).

[90] W. T. Pollard, A. K. Felts, and R. A. Friesner, *The Redfield Equation in Condensed-Phase Quantum Dynamics*, Adv. Chem. Phys. **93**, 77 (1996).

[91] W. T. Pollard and R. A. Friesner, *Solution of the Redfield equation for the dissipative quantum dynamics of multilevel systems*, J. Chem. Phys. **100**, 5054 (1994).

[92] W. T. Pollard, S.-Y. Lee, and R. A. Mathies, *Wave packet theory of dynamic absorption spectra in femtosecond pump-probe experiments*, J. Chem. Phys. **92**, 4012 (1990).

[93] W. H. Press, S. A. Teukolsky, W. T. Vetterling, and B. P. Flannery, *Numerical Recipes in FORTRAN 77*, Cambridge University Press, Cambridge, 1992.

[94] A. Raab and H.-D. Meyer, *A numerical study of the performance of the multiconfiguration time-dependent Hartree method for density operators*, J. Chem. Phys. **112**, 10718 (2000).

[95] S. Ramakrishna and F. Willig, *Pump-Probe Spectroscopy of Ultrafast Electron Injection from the Excited State of an Anchored Chromophore to a Semiconductor Surface in UHV: A Theoretical Model*, J. Phys. Chem. B **104**, 68 (2000).

[96] S. Ramakrishna, F. Willig, and V. May, *Photoinduced ultrafast electron injection from a surface attached molecule: Control of electronic and vibronic distributions via vibrational wave packets*, Phys. Rev. B **62**, R16330 (2000).

[97] ———, *Theory of ultrafast photoinduced heterogeneous electron transfer: Decay of vibrational coherence into a finite electronic vibrational quasicontinuum*, J. Chem. Phys. **115**, 2743 (2001).

[98] A. G. Redfield, *The Theory of Relaxation Processes*, Adv. Magn. Reson. **1**, 1 (1965).

[99] C. Reichardt, *Solvents and solvent effects in organic chemistry*, VCH, Weinheim, 1990.

[100] P. Reineker, *Stochastic Liouville Equation Approach: Coupled Coherent and Incoherent Motion, Optical Line Shapes, Magnetic Resonance Phenomena*, in: Exciton Dynamics in Molecular Crystals and Aggregates (G. Höhler, ed.), Springer Tracts in Modern Physics, vol. 94, Springer, Berlin, 1982, pp. 111–226.

[101] R. D. Ruth, *A canonical integration technique*, IEEE Trans. Nucl. Science **30**, 2669 (1983).

[102] P. Saalfrank, *Stochastic wave packet vs. direct density matrix solution of Liouville-von Neumann equations for photodesorption problems*, Chem. Phys. **211**, 265 (1996).

[103] R. Scholz, M. Darwish, and M. Schreiber, *Ultrafast electron transfer of betaine-30*, J. Lumin. **76&77**, 404 (1998).

[104] M. Schreiber, I. Kondov, and U. Kleinekathöfer, *Different direct integrators for Redfield equations applied to electron transfer dynamics*, J. Mol. Liq. **86**, 77 (2000).

[105] D. Segal, A. Nitzan, W. B. Davis, M. R. Wasielewski, and M. A. Ratner, *Electron Transfer Rates in Bridged Molecular Systems 2. A Steady-State Analysis of Coherent Tunneling and Thermal Transitions*, J. Phys. Chem. B **104**, 3817 (2000).

[106] L. Seidner, G. Stock, and W. Domcke, *Nonperturbative approach to femtosecond spectroscopy: General theory and application to multidimensional nonadiabatic photoisomerization processes*, J. Chem. Phys. **103**, 3998 (1995).

[107] Y. R. Shen, *The Principles of Nonlinear Optics*, Wiley, New York, 1984.

[108] J. Steinbach, B. M. Garraway, and P. L. Knight, *High-order unraveling of master equations for dissipative evolution*, Phys. Rev A **51**, 3302 (1995).

[109] G. Stock and M. Thoss, *Semiclassical Description of Nonadiabatic Quantum Dynamics*, Phys. Rev. Lett. **78**, 578 (1997).

[110] J. T. Stockburger and H. Grabert, *Exact c-Number Representation of Non-Markovian Quantum Dissipation*, Phys. Rev. Lett. **88**, 170407 (2002).

[111] W. T. Strunz, *The Brownian motion stochastic Schrödinger equation*, Chem. Phys. **268**, 237 (2001).

[112] W. T. Strunz, L. Diosi, N. Gisin, and T. Yu, *Quantum Trajectories for Brownian Motion*, Phys. Rev. Lett. **83**, 4909 (1999).

[113] H. Sumi and R. A. Marcus, *Dynamical effects in electron transfer reactions*, J. Chem. Phys. **84**, 4894 (1986).

[114] M. Suzuki and K. Nasu, *Dynamics of charge transfer from molecule to semiconductor at surface: Numerical method for nonadiabaticity and irreversibility in discrete-continuum transition*, J. Chem. Phys. **92**, 4576 (1990).

[115] T. Takagahara, E. Hanamura, and R. Kubo, *Second Order Optical Processes in a Localized Electron-Phonon System - Stationary Response*, J. Phys. Soc. Japan **44**, 728 (1978).

[116] M. Thoss, H. Wang, and W. H. Miller, *Self-consistent hybrid approach for complex systems: Application to the spin-boson model with Debye spectral density*, J. Chem. Phys. **115**, 2991 (2001).

[117] G. C. Walker, E. Åkesson, A. E. Johnson, N. E. Levinger, and P. F. Barbara, *Interplay of Solvent Motion and Vibrational Excitation in Electron-Transfer Kinetics: Experiment and Theory*, J. Phys. Chem. **96**, 3728 (1992).

[118] H. Wang, M. Thoss, and W. H. Miller, *Systematic convergence in the dynamical hybrid approach for complex systems: A numerically exact methodology*, J. Chem. Phys. **115**, 2979 (2001).

[119] U. Weiss, *Quantum Dissipative Systems*, 2nd ed., World Scientific, Singapore, 1999.

[120] B. Wolfseder, *Modellrechnung zur Dynamik und Zeitaufgelösten Spektroskopie von ultraschnellen Elektron-Transfer-Prozessen*, Dissertation, Technische Universität München, München, 1997.

[121] B. Wolfseder and W. Domcke, *Multi-mode vibronic coupling with dissipation. Application of the Monte Carlo wavefunction propagation method*, Chem. Phys. Lett. **235**, 370 (1995).

[122] ———, *Intramolecular electron-transfer dynamics in the inverted regime: quantum mechanical multi-mode model including dissipation*, Chem. Phys. Lett. **259**, 113 (1996).

[123] B. Wolfseder, L. Seidner, W. Domcke, G. Stock, M. Seel, S. Engleitner, and W. Zinth, *Vibrational coherence in ultrafast electron-transfer dynamics of oxazine 1 in N,N-dimethyl-aniline: simulation of a femtosecond pump-probe experiment*, Chem. Phys. **233**, 323 (1998).

[124] B. Wolfseder, L. Seidner, G. Stock, and W. Domcke, *Femtosecond pump-probe spectroscopy of electron-transfer systems: a nonperturbative approach*, Chem. Phys. **217**, 275 (1997).

[125] X. Zhao, J. A. Burt, F. J. Knorr, and J. L. McHale, *Thermosolvatochromism of Betaine-30 in* CH_3CN, J. Phys. Chem. A **105**, 11110 (2001).

[126] Y. Zong and J. L. McHale, *Resonance Raman study of solvent dynamics in electron transfer. I. Betaine-30 in* CH_3CN *and* CD_3CN, J. Chem. Phys. **106**, 4963 (1997).

[127] H. Zoubi, M. Orenstien, and A. Ron, *Coupled microcavities with dissipation*, Phys. Rev. A **62**, 033801 (2000).

Erklärung gemäß Promotionsordnung §6 (2) 4, 5

Hiermit erkläre ich, dass ich die vorliegende Arbeit selbständig und nur unter Verwendung der angegebenen Literatur und Hilfsmittel angefertigt habe. Die Stellen in der Arbeit, die in Sinn und Wortlaut anderen Werken entnommen wurden, habe ich entsprechend gekennzeichnet. Ich erkläre, nicht bereits früher oder gleichzeitig bei anderen Hochschulen oder an der Universität Chemnitz ein Promotionsverfahren beantragt zu haben. Die derzeit gültige Promotionsordnung der Fakultät für Naturwissenschaften der Technischen Universität Chemnitz vom 10. Oktober 2001 ist mir bekannt.

Chemnitz, den 17. Oktober 2002

Ivan Kondov

Thesen zur Dissertation

- In allen Konfigurationen wird bei starker elektronischer Kopplung das Langzeitverhalten der Populationsdynamik von der diabatischen Dämpfungsnäherung (DDA) beeinflusst. Je stärker die Kopplung ist, desto größer ist die Abweichung vom thermischen Gleichgewicht mit dem Wärmebad bei $t \to \infty$.

- Die DDA kann zu falscher Populationsdynamik führen, auch wenn die Kopplung genügend klein ist. Dies passiert im Falle von Potenzialkonfigurationen mit Barriere, wobei zumindest ein vibronisches Niveau im angeregten Zustand unter dem Kreuzungspunkt der diabatischen Potenziale liegt. Bei schwacher elektronischer Kopplung in den barrierelosen Potenzialkonfigurationen, sowie im Marcus'schen invertierten Bereich, ist die DDA durchaus gerechtfertigt.

- Mit Hilfe der Störungstheorie erster Ordnung in der elektronischen Kopplung ließ sich das Matrixelement des Relaxationsoperators Λ in diabatischer Darstellung analytisch bestimmen. Somit wurde der Einfluss der elektronischen Kopplung auf die dissipativen Mechanismen berücksichtigt.

- Der einzige Mechanismus in der DDA, der zur Transferdynamik beiträgt, ist kohärenter Transfer zwischen Niveaus mit großer Franck-Condon-Überlappung. Die dissipativen Terme führen lediglich zu einer Dämpfung innerhalb jedes Potenzials. Dissipative Transfermechanismen treten erst mit Berücksichtigung der ersten Ordnung des Relaxationsoperators auf.

- Verschiedene numerische Methoden zur Propagation von Dichtematrizen wurden implementiert und auf ihre Effizienz geprüft. Abgesehen vom hochgenauen Newtonschen Polynom-Verfahren zeigt die Runge-Kutta-Methode von NAG die beste Leistung in beiden diabatischer und in adiabatischer Darstellungen der Dichtematrix. Der short-iterative-Arnoldi-Propagator zeigt ein relativ günstiges Verhältnis zwischen Aufwand und Genauigkeit.

- Zur effizienten Lösung allgemeiner zeit-lokaler Mastergleichungen, die nicht auf die Lindblad-Form beschränkt sind, wurde ein neues stochastisches Entfaltungsschema entwickelt. Die numerischen Teste an zwei Beispielsystemen (Brown'sche Bewegung und Elektrontransfer) haben gezeigt, dass die neue Methode schon bei 1000 Realisierungen eine genügende Konvergenz ergibt, obwohl diese Simulation im Vergleich mit dem üblichen Quantensprung-Verfahren aufwendiger ist.

- Die Lage des Absorptionsmaximums im simulierten frequenz- und zeit-aufgelösten Spektrum von Betain-30, sowie des Emissionsmaximums, stimmen mit den experimentell aufgenommenen Spektren quantitativ überein. Die Resultate bestätigen die Erkenntnis, dass der Elektrontransfer-Übergang vom S_1- zum S_0-Zustand in Betain-30 ein mehrstufiger Prozess ist.

- Zwei Stufen sind beim Elektrontransferprozess in Betain-30 zu unterscheiden. Die erste schließt die Solvatatisierung des angeregten Zustandes S_1 und die Umordnung der niedrigfrequenten Mode ein. Die zweite ist ein strahlungsloser Übergang zum Grundzustand S_0 und langsame Relaxation (Abkühlung) im Grundzustand.

- Die Verwendung von Modellen für Elektrontransfer mit zwei Reaktionsmoden hat Elektrontransferraten ergeben, die besser mit dem Experiment als die Raten vom Modell mit einer einzelnen Mode, sowie besser als die Vorhersagen anderer Theorien, übereinstimmen.

- Die Behandlung der nicht-Markovschen Effekte beim ultraschnellen Exzitontransfer erfordert die Berücksichtigung der Anfangskorrelationen in der reduzierten Dichtematrix.

Lebenslauf

Persönliche Angaben

Name:	Ivan Stelyianov Kondov, Dipl. Chem.
Geburtsdatum:	18.03.1973
Geburtsort:	Dobrich, Bulgarien
Staatsangehörigkeit:	bulgarisch
Familienstand:	seit 17.08.1996 verheiratet, ein Kind

Schulbildung

1980 – 1987	Polytechnische Oberschule in Dobrich
1987 – 1991	Sekundarschule mit englischer Sprache in Dobrich
Mai 1991	Abschlussprüfungen (Abitur)

Studium und Beruf

01.10.1991 – 18.07.1996	Studium in der Fachrichtung Chemie an der Universität Sofia
01.02.1996 – 01.07.1996	Diplomarbeit “Einfluss der Umgebung und der Strukturbesonderheiten auf die photo- und thermochromen Eigenschaften von nitrosubstituierten Spiropyranidolinen”
18.07.1996	Verteidigung der Diplomarbeit, Prädikat “ausgezeichnet”
seit 18.07.1996	Akademischer Grad “Magister der Chemie”
01.09.1996 – 31.03.1999	Wissenschaftlicher Mitarbeiter, Central Laboratory of Photoprocesses, Bulgarian Academy of Sciences
17.06.1998 – 15.10.1998	Aufenthalt als Gastwissenschaftler in der Professur “Theorie ungeordneter Systeme” an der Technischen Universität Chemnitz bei Prof. Dr. M. Schreiber
01.11.1998 – 31.03.1999	Entwicklung von Messverfahren und Anwendung der Chemometrie und der Kolorimetrie in spektroskopischen Analysen bei OpTec GmbH, Bulgarien
seit 01.04.1999	Wissenschaftlicher Mitarbeiter an der Technischen Universität Chemnitz in der Professur “Theorie ungeordneter Systeme”, Thema der Promotion “Elektrontransfer in molekularen Systemen”

Veröffentlichungen und Vorträge

Publikationen

[1] M. Schreiber, I. Kondov, and U. Kleinekathöfer, *Different direct integrators for Redfield equations applied to electron transfer dynamics*, J. Mol. Liq. **86**, 77 (2000).
[2] I. Kondov, U. Kleinekathöfer, and M. Schreiber, *Efficiency of different numerical methods for solving Redfield equations*, J. Chem. Phys. **114**, 1497 (2001).
[3] U. Kleinekathöfer, I. Kondov, and M. Schreiber, *Perturbative treatment of intercenter coupling in the framework of Redfield theory*, Chem. Phys. **268**, 121 (2001).
[4] M. Schreiber, I. Kondov, and U. Kleinekathöfer, *A density matrix approach to photoinduced electron injection*, J. Lumin. **94&95**, 471 (2001).
[5] U. Kleinekathöfer, I. Kondov, and M. Schreiber, *Stochastic unraveling of time-local quantum master equations beyond the Lindblad class*, Phys. Rev. E **66**, 037701 (2002).
[6] M. Schreiber, I. Kondov, and U. Kleinekathöfer, *Numerical simulation of electron transfer rates in betaine-30*, Nonlin. Opt. (accepted).
[7] I. Barvík, I. Kondov, P. Heřman, M. Schreiber, and U. Kleinekathöfer, *Femtosecond dynamics in the anisotropy of emission in LH2 units*, Nonlin. Opt. (accepted).

Vorträge

[8] I. Kondov, U. Kleinekathöfer, and M. Schreiber, *Theory of ultrafast electron transfer dynamics in large systems with dissipation*, 36th Symposium for Theoretical Chemistry (Litschau, Austria), September 2000.
[9] I. Kondov, U. Kleinekathöfer, and M. Schreiber, *Stochastic wave function methods for solving quantum master equations*, Seminar at Faculty of Mathematics and Physics (Charles University, Prague, Czech Republic), November 2001.
[10] I. Kondov, U. Kleinekathöfer, and M. Schreiber, *Numerical studies of electron transfer dynamics in systems with dissipation*, Seminar at the professor chair of Theoretical chemistry (Technische Universität München), May 2002.

Posterbeiträge auf Konferenzen

[11] I. Kondov, U. Kleinekathöfer, and M. Schreiber, *Dissipative quantum dynamics of photoinduced electron transfer*, 35th Symposium for Theoretical Chemistry (Freiberg, Germany), September 1999.

[12] I. Kondov, U. Kleinekathöfer, and M. Schreiber, *Numerische Untersuchungen zur Elektronentransferdynamik in molekularen Systemen*, Spring Meeting of the German Physical Society (Potsdam, Germany), March 2000.

[13] I. Kondov, U. Kleinekathöfer, and M. Schreiber, *Numerical studies of ultrafast electron transfer in betaine-30*, Symposium on Electron Transport on the Molecular Scale (MPIPKS, Dresden, Germany), February 2001.

[14] I. Kondov, U. Kleinekathöfer, and M. Schreiber, *Theory and numerical studies of electron transfer in betaine-30*, The Seventh European Conference On Atomic And Molecular Physics (Berlin, Germany), April 2001.

[15] I. Kondov, U. Kleinekathöfer, and M. Schreiber, *Theoretical and numerical studies of electron transfer in betaine-30*, 5th International Symposium of the Volkswagen-Stiftung on Intra- and Intermolecular Electron Transfer (Chemnitz, Germany), May 2001.

[16] I. Kondov, U. Kleinekathöfer, and M. Schreiber, *Numerical simulation of pump-probe spectra of systems with intramolecular electron transfer*, 37th Symposium for Theoretical Chemistry (Bad Herrenalb, Germany), September 2001.

[17] I. Kondov, U. Kleinekathöfer, and M. Schreiber, *Stochastic unraveling and applications of non-Lindblad quantum master equations*, International Workshop QRandom II (MPIPKS, Dresden, Germany), January 2002.

[18] I. Kondov, U. Kleinekathöfer, and M. Schreiber, *Numerical simulation of time-resolved absorption/emission spectra of betaine-30 in solution*, Spring Meeting of the German Physical Society (Osnabrück, Germany), March 2002.

[19] I. Kondov, U. Kleinekathöfer, and M. Schreiber, *Mechanisms of intramolecular charge transfer revealed by simulated pump-probe spectra*, International Workshop "Quantum dynamical concepts: from diatomics to biomolecules"(MPIPKS, Dresden, Germany), April 2002.

[20] I. Kondov, U. Kleinekathöfer, and M. Schreiber, *Simulation of transient frequency-resolved absorption and emission spectra of betaine-30 in solution*, 38th Symposium for Theoretical Chemistry (Bremen, Germany), August 2002.

Danksagung

An dieser Stelle möchte ich mich recht herzlich bei allen bedanken, ohne die meine Promotion gar nicht möglich gewesen wäre.

Zuallererst danke ich Herrn Prof. Dr. Michael Schreiber, der mich in seine Arbeitsgruppe sehr freundlich aufgenommen hat. Er hat mir das interessante Forschungsthema vorgeschlagen und hat mich während meines ersten Gastaufenthalts in Chemnitz sowie weiter während meiner Promotionszeit stets betreut und unterstützt.

Mein besonderer Dank gilt Herrn Dr. Ulrich Kleinekathöfer. Er war mein unmittelbarer und hingebungsvoller Betreuer und fand sich jederzeit zu Besprechungen und Hilfe bereit. Ihm danke ich auch für das Korrekturlesen der Dissertation.

Desweiteren bedanke ich mich bei allen Kollegen der Arbeitsgruppe, die für eine angenehme und kreative Arbeitsatmosphäre gesorgt haben.

Ebenso danke ich Philipp Cain für seine Hilfe bei Computerproblemen und Mike Becher vom Universitätsrechenzentrum für die Unterstützung bei meinen Parallelrechnungen auf dem Chemnitzer Linux Cluster.

Für hilfreiche Diskussionen bedanke ich mich auch bei den Herren Prof. Dr. Wolfgang Domcke, Dr. habil. Volkhard May, Dr. Michael Thoss und den Doktoranden Frau Dassia Egorova und Herrn Alexey Novikov.

Besonders dankbar bin ich dem Graduiertenkolleg “Dünne Schichten und nichtkristalline Materialien” und seinem Sprecher Herrn Prof. Dr. Frank Richter für die Finanzierung und die Fortbildungsmöglichkeiten in den Seminaren und den Ringvorlesungen.

Das Kapitel über Exzitontransfer in der Dissertation entstand in Kollaboration mit Herrn Prof. Ivan Barvík von der Karls Universität in Prag. Ihm danke ich herzlich für seine Gastfreundschaft während der drei angenehmen Aufenthalte in Prag.

Mein Fortschritt mit der deutschen Sprache ist größtenteils Frau Erna Adamczyk zu verdanken. Bei ihr bedanke ich mich deshalb ganz herzlich.

Nicht zuletzt geht mein Dank auch an meine Frau Krassimira und meinen Sohn Kaloyan für ihre stetige Begleitung im Alltag und besonders für ihre Geduld in der Endphase, in der ich die Dissertation zusammenschrieb.